

UNIVERSITÀ DEGLI STUDI DI PADOVA

Dipartimento di Fisica e Astronomia “Galileo Galilei”

Master Degree in Astrophysics and Cosmology

Final Dissertation

The cosmological relevance of Fuzzy Dark Matter

Thesis supervisor

Dr. Daniele Bertacca

Thesis co-supervisor

Prof. Nicola Bartolo

Candidate

Mr. Luca Panozzo

Anno Accademico 2022/2023

Abstract

In this thesis we discuss an alternative to Cold Dark Matter (CDM) currently adopted in the concordance model of cosmology, the Λ CDM model. This alternative is called Fuzzy DM (FDM) and it is composed of an ultralight scalar field called axion with a mass around 10^{-22} eV. In this thesis we look for observables that could be able to verify the presence of ultralight axions as the source of DM. In order to do that, we derive the equation of motion of this scalar field and the Euler equation which shows an additional quantum pressure term that cause a cut-off in the non-linear matter power spectrum $P_{nl}(k, z)$ in the small scales regime. This cut-off is dependent on the mass of the axion, so the non-linear matter power spectrum can be used to put constraints on the mass of the axion. Another observable used to obtain information on the mass of an axion is the power spectrum related to the alignment of galaxies. Galaxy alignment is given by three contribution which are an intrinsic galaxy alignment $\langle \epsilon^s \epsilon^s \rangle$, an extrinsic one called shear $\langle \gamma \gamma \rangle$ and a mixed term $\langle \epsilon^s \gamma \rangle + \langle \gamma \epsilon^s \rangle$. All these three terms are dependent on the non-linear matter power spectrum, and so its modification is also felt by the galaxy alignment.

Contents

Contents	i
Introduction	iii
1 The Concordance Model of Cosmology	1
1.1 Hubble expansion	2
1.2 The CMB Radiation	3
1.3 Universe overview	5
1.3.1 The FLWR metric	5
1.3.2 The Friedmann equations	6
1.4 Inflation	7
1.4.1 The Flatness problem	7
1.4.2 The Horizon problem	9
1.4.3 The Unwanted Relics Problem	9
1.4.4 The dynamics of inflation	10
2 Dark Matter	13
2.1 The genesis of Dark Matter	15
2.1.1 The evolution of the particle density	15
2.1.2 The freeze-out mechanism	18
2.1.3 Cold Dark Matter	19
2.2 Small scale issues	20
2.2.1 The Missing Satellite Problem	20
2.2.2 The Core-Cusp Problem	21
3 Fuzzy Dark Matter	23
3.1 The QCD Axion	24
3.2 Classical Field Justification	24
3.3 Unperturbed Klein-Gordon Equation	25
3.4 Klein-Gordon perturbed	26
3.5 From Klein-Gordon to fluid treatment	29
3.6 Probability Current	30
3.7 Madelung equations	32
3.8 Jeans scale	33
3.9 The Axiverse	35
3.9.1 Planck CMB data	37
3.9.2 BOSS galaxy spectrum and bispectrum data	39
3.9.3 Constraints on the axion population	42
3.10 Generation of the first stars	44
3.10.1 The simulation	44
3.10.2 Results on PopIII stars formation	45
3.11 The Fornax dSph galaxy	51

4 The Superradiance	53
4.1 Kerr Black Holes	53
4.1.1 The classical Penrose process	54
4.2 The superradiance condition	55
4.3 The Black Hole Bomb	56
4.4 The Gravitational Atom	59
4.5 Binary Inspiral System	59
4.5.1 The gravitational effect of the companion	61
4.5.2 Overview on the energetic transition	62
4.5.3 Gravitational Wave emission	64
5 Galaxy Alignment	67
5.1 Galaxy triaxial shape	67
5.2 The matter power spectrum	68
5.2.1 The linear matter power spectrum	69
5.2.2 The non-linear matter power spectrum	69
5.3 Gravitational Lensing	71
5.3.1 The shear power spectrum	74
5.3.2 The total power spectrum	78
6 Conclusions	81
Bibliography	97

Introduction

The Λ CDM model successfully describes the evolution of the Universe from its beginnings to today. This model relies on Einstein's General Relativity and the Cosmological Principle which states that, at large scales, the Universe appears to be homogeneous and isotropic. The success of the model, however, is certainly not the same thing as saying that all the questions have already been answered.

Today it is well known that baryonic matter represents only a tiny fraction of the total energy density of the Universe. In particular, its contribution is more or less the 5%. DM is way more relevant than ordinary matter, since its energy density is almost the 26% of the total one. In the end, the vast majority of the total energy density in the Universe is represented by the energy responsible for the accelerated expansion of the Universe or Dark Energy (DE) which is more or less the 69%). When studying the evolution of the Universe, it is obvious that DM plays a key role in understanding phenomena that we can observe.

Identify the nature of DM represents one of the most difficult puzzles to solve in modern cosmology. CDM is well-suited to explain large scales phenomena, however, it fails to explain the effects that occur on a small scales. CDM cannot solve the Core-Cusp Problem or the Missing Satellite Problem, for example. These two small scales issues arise from the fact that CDM predicts too much DM halos and subhalos that create dwarf galaxies. In order to have a more complete theory on DM, we should be able to preserve the large scales behaviour of CDM but change the one at small scales. For this reason it was introduced one of the alternative forms of DM, the FDM.

The particle of FDM is an ultralight scalar field, typically identified with the axion, whose mass can cover a very wide range of values. The mass of the axion considered in this thesis is around 10^{-22} eV, but, depending on the model considered, it can reach also far lower values till 10^{30} eV. When the mass is so low, the axion contribution is no longer to DM, but DE. In this work we will assume that DM is entirely composed of these axions unless expressly stated otherwise.

The small mass causes quantum behavior to be factored into the equation of motion expressed by the Klein-Gordon equation and this will lead to an Euler equation with an extra term representing a quantum pressure that is negligible at large scales, but it suppresses the matter power spectrum at small scales, where the conventional CDM predict an excess of DM.

Since DM is not directly detectable, the goal is to find observables that are dependent on the presence of the axion. One simple example of observable that suffers axions is the linear and non-linear matter power spectrum since it is directly related to both baryonic and non-baryonic matter. The non-linear matter power spectrum $P_{nl}(k, z)$ with the implementation of the axion transfer function $T^2(k)$ can give us some constraints on the mass of the ultralight scalar field. The other observable studied in this thesis is the angular power spectrum of galaxy alignment $C(l)$ which is strongly related to $P_{nl}(k, z)$, and so for the same reason, the observable is useful to gain additional information on the mass of the axion.

In chapter 1 there is a brief introduction to the most important equations and details about the concordance model of cosmology. Chapter 2 is devoted to explain why DM is necessary in the Λ CDM model, how its number density evolved with time and the reason why the model involves specifically cold DM. The chapter ends with two shortcomings of the Λ CDM model such as the Core-Cusp Problem and the Missing Satellite Problem that cannot be solved with CDM. Chapter 3 introduces FDM as an alternative to CDM, how this change in the nature of DM reflects on the equation of motion and the Euler equation and the consequences on the matter power spectrum. It is treated also the possibility to have an Axiverse instead of an axion with a single fixed mass

and the repercussion of the axion presence on the first generation of stars. Chapter 4 is meant to be an insight into the possible detection of gravitational waves around compact objects surrounded by a cloud of axion known as the gravitational atom, but this is not treated in details. The last chapter provides information on the gravitational lensing, so it is firstly described how the simple matter power spectrum is obtained and then how this is related to the angular power spectrum of lensing. In the last section it is described how the addition of the axion transfer function of the axion can change the original power spectrum and provide constraints on the axion mass.

We emphasize that where it is not specified, we are assuming normal units, therefore $c = \hbar = G = 1$.

Chapter 1

The Concordance Model of Cosmology

This first chapter is dedicated to providing a brief introduction to the current Standard Model of Cosmology, to characterize what are the processes it includes and to define the basic mathematical tools used in this thesis.

What is today known as the Concordance Model of Cosmology, was originally formulated as the Hot Big Bang Model and, as new questions and possible explanations arose, it expanded to become the current Λ CDM. Λ refers to the presence of DE that drives the current accelerated expansion of the Universe, while CDM represents the major contribution to the matter energy density [52].

Thanks to the work of cosmologists who have followed one another over the years, it was elaborated a model that was able to describe how the Universe has evolved throughout its existence, even though there are still many questions to answer. According to the NASA Explorer mission WMAP (Wilkinson Microwave Anisotropy Probe) [157] launched in June 2001, the age of the Universe seems to be more or less 13.8 billion years and, thanks to the concordance model, it has been possible to highlight the fundamental events that took place.

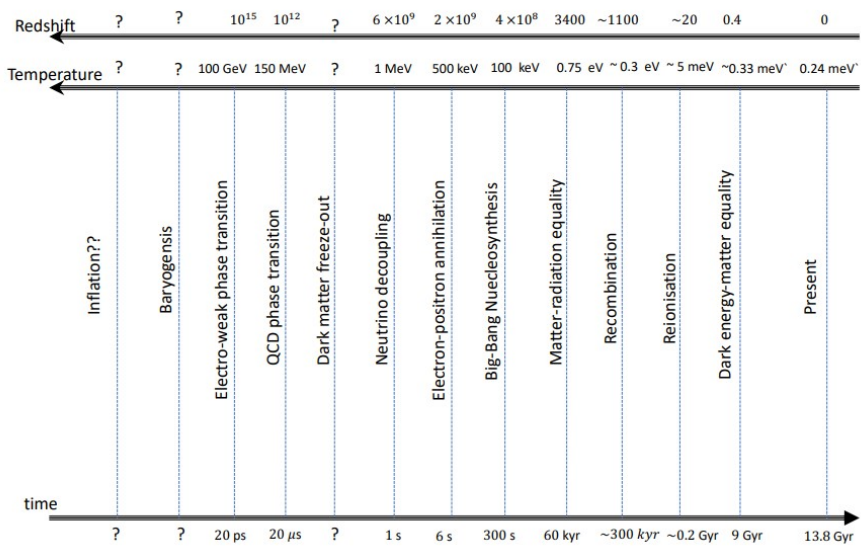


Figure 1.1: Timeline of the Universe that highlights redshift, temperature and time of the most important events (Figure from [92]).

According to the model, the Universe expansion was triggered by a phenomenon that takes the name of "*Big Bang*". The temperature before that event was infinite, while the radius of the

Universe was equal to 0 i.e. the Universe density was infinite [52]. In Fig[1.1] it is possible to see the most important event in the history of the Universe and when they took place. Even though this model is considered and accepted by most scientists as the Standard Cosmological Model, since there are several observational evidences that the Λ CDM model is capable of describing what cosmologists have been observing over the centuries, cosmologists have continued to debate and are still debating what happened immediately after the Big Bang and what led to the Universe to appear as it is today.

Before trying to give a possible interpretation to what it is possible to observe in Universe and why it is so, it is important to make a brief review of the model currently in use. This chapter is used to introduce the tools and notions that will be needed to carry out this work.

1.1 Hubble expansion

Since the Universe is expanding, it is very important to distinguish between physical and comoving coordinates.

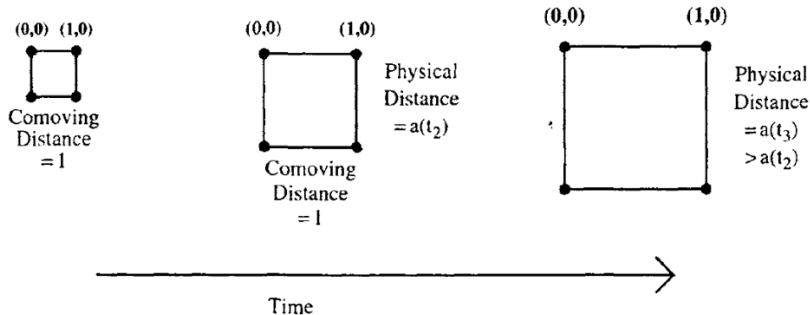


Figure 1.2: Simple representation of the expansion of the Universe that show the difference between comoving and physical distance (Figure from [52]).

In this figure, a key element is the scale factor $a(t)$, which characterize the expansion. The current value of this parameter is conventionally set $a(t = t_0) = 1$ and, going backward, it becomes smaller and smaller [52]. The scale factor $a(t)$ is the parameter that allow the conversion between physical and comoving coordinates. Referring to the Fig[1.2] while the comoving distance x between two point in the grid remain the same, the physical distance d changes. This is due to the fact that the two type of distances are related in the following way:

$$d(t) = a(t)x. \quad (1.1)$$

Now, since the Universe is expanding, this means that, for example, a source of light is stepping away from an observer at rest. As a consequence, the physical wavelength of the light emitted by the source is affected by the expansion and the observer detect a different wavelength. This phenomenon is described by the redshift z :

$$1 + z = \frac{\lambda_{\text{obs}}}{\lambda_{\text{emit}}} = \frac{a_{\text{obs}}}{a_{\text{emit}}} = \frac{1}{a_{\text{emit}}}. \quad (1.2)$$

In the last step it is considered that the observer detects the light today, so $a_{\text{emit}} = a(t_0) = 1$.

Edwin Hubble in 1929 published a paper named "*A Relation between Distance and Radial Velocity among Extra-Galactic Nebulae*" [77] in which he observed that the farther a galaxy is from Earth, the faster it is for an observer on this planet (neglecting potential comoving motion of the galaxy itself). He inserted the data in a plot distance-velocity and obtain Fig[1.3]

Since there are no peculiar comoving velocities of galaxies, it means that $\dot{x} = 0$ and physical velocities measured by Hubble is given by the Hubble-Lemaître law, obtained by deriving eq[1.1]

$$v = \frac{d}{dt}(ax) = \dot{a}x = \frac{\dot{a}}{a}(ax) = H_0 d. \quad (1.3)$$

The slope H is known as the Hubble rate $H = \dot{a}/a$ and quantifies the rate of change of the scale factor [77, 52]. Even though the value obtained by Hubble was affected by errors in the measured distances of the objects and led to $H_0 = 500 \text{ km s}^{-1} \text{ Mpc}^{-1}$, the current value of H is parameterized with $H_0 = 100 h \text{ km s}^{-1} \text{ Mpc}^{-1}$ where $h \sim 0.7$ seems to be the most correct estimate. The 2018 Planck data [135] gives $H_0 = 67.36 \text{ km s}^{-1} \text{ Mpc}^{-1}$. This value of H_0 is called Hubble constant and its inverse gives us the Hubble time which is the age the Universe would have if the expansion were linear [52]. The Hubble time is approximately 14 billion years, slightly bigger than the actual age, since the expansion of the Universe is not linear, as already known.

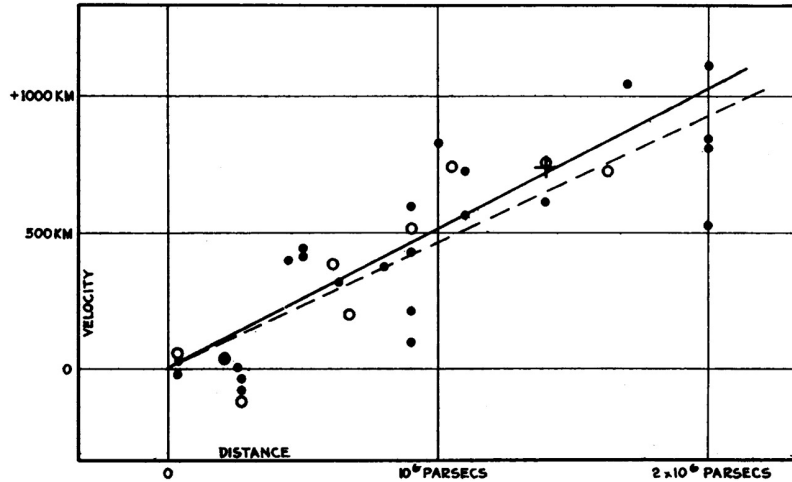


Figure 1.3: The original Hubble diagram velocity-distance. There are two lines whose slopes give the Hubble constant. Hubble plotted two different lines considering two groups of objects (Figure from [77]).

1.2 The CMB Radiation

At the very beginning, the Universe was extremely hot and dense. All the components were in thermal equilibrium, so everything was at the same temperature thanks to the interactions of the different elements with each other. One effect of the expansion is that the Universe cools down and this means that, at some point, thermal equilibrium will be no longer maintained, since the interactions of the components will become inefficient. This condition is verified when the interaction rate of a specific event Γ becomes lower than the Hubble rate evaluated at that specific time $H(t_*)$.

At first, photons were interacting with free electrons in the plasma of hot particles. The mean free path of photons was short and so the early Universe appears to be opaque for the first 380,000 years ($z \sim 1100$), until what is called "Recombination Era". The expansion was proceeding and the Universe was getting colder and colder. At $z \sim 1100$, the temperature was low enough to allow free electrons to combine with protons in order to form electrically neutral H atoms. Photons found themselves without free electron to interact with and start travel longer distances. This is called the "decoupling" of photons. These free photons are observable and give one of the most important images of how the early Universe looked like and represents the limit of its direct observations. The temperature of these photons, felt the expansion and starting from $T_{\text{Rec}} = 10^4 \text{ K}$, it reached an effective value of about $T_0 \sim 2.7 \text{ K}$. This temperature corresponds to a wavelength that put the photons in the microwave domain, and this is the reason for the name CMB, Cosmic Microwave Background [52].

This cosmic radiation was detected for the first time in the 1964 almost by accident by Arno Penzias and Robert Wilson and, since then, has been the subject of countless studies [130].

The spectrum of this relic radiation is an almost perfect black body, since it gives a picture of the Universe in the last moment of thermal equilibrium. The distribution is given by the following relation [52]:

$$I_\nu = \frac{4\pi\hbar\nu^3/c^2}{\exp[2\pi\hbar\nu/k_B T] - 1}, \quad (1.4)$$

where the Planck constant is $\hbar = h/2\pi = 1.05 \cdot 10^{-34} \text{ J} \cdot \text{s} = 6.58 \cdot 10^{-16} \text{ eV} \cdot \text{s}$, the speed of light is $c = 299792458 \text{ m s}^{-1}$ and the Boltzmann constant is $k_B = 1.38 \cdot 10^{-23} \text{ J K}^{-1}$.

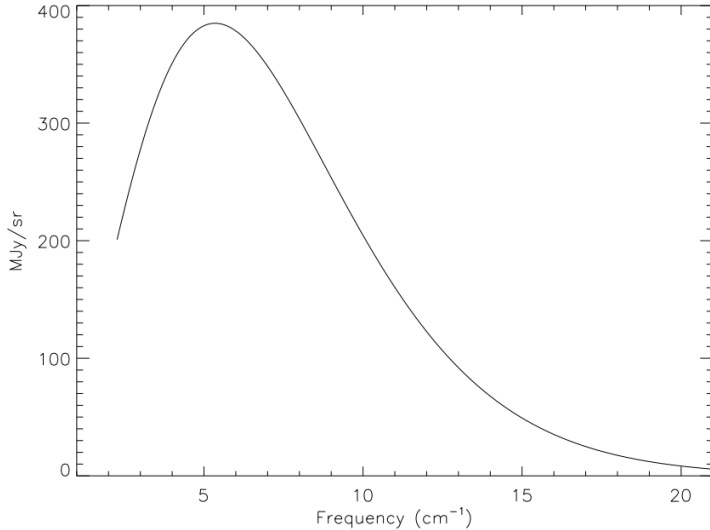


Figure 1.4: Spectrum of the CMB. It appears as a perfect black body radiation up to the point that the error bars are smaller than the actual line of the model (Figure from [62]).

During the years, several space missions have been launched in order to create an image of how the last scattering surface looks like in terms of physical properties like the temperature. The most detailed one available is given by the Plank mission [135] and it is plotted in Fig. 1.5. As can be seen, there are small anisotropies in temperature. This is due to the fact that the early Universe was not completely smooth and, as will be seen later, these inhomogeneities of order $\Delta T/T \sim 10^{-5}$ are essential for the formation of all the structures that are observable in the Universe today. These structures are well known to be non-isotropic, as can be seen in Fig. 1.6.

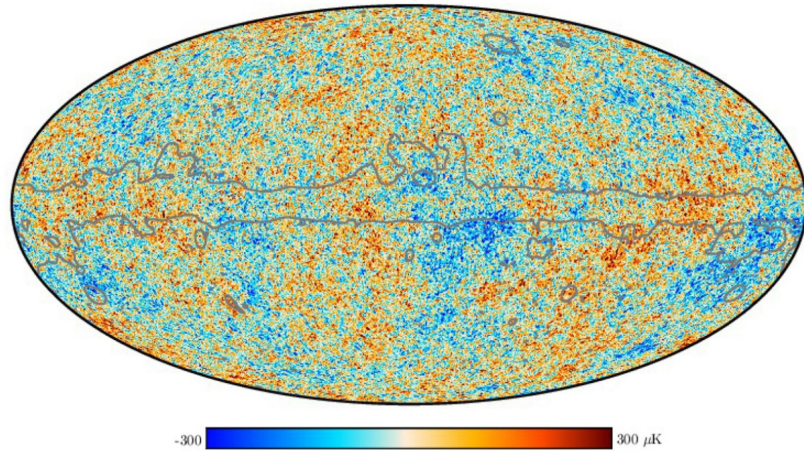


Figure 1.5: The Cosmic Microwave Background map taken by Plank. This map shows the small fluctuations in the background temperature and their order of magnitudes (Figure from [134]).

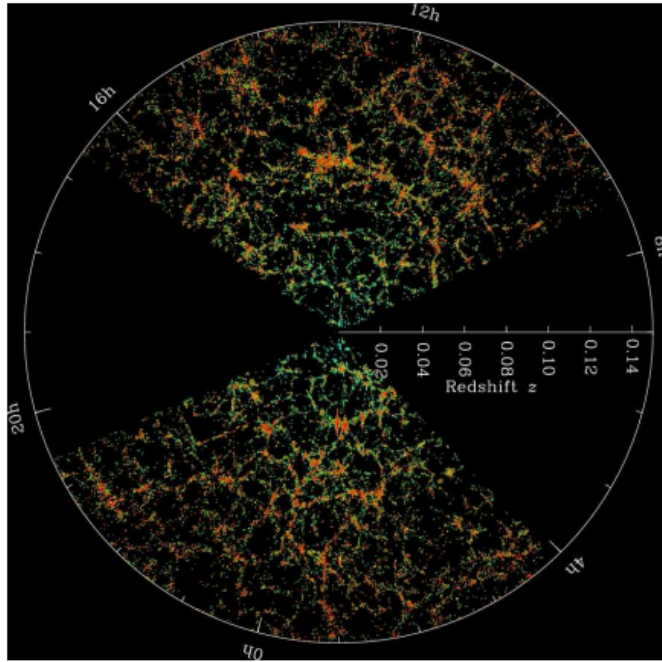


Figure 1.6: Distribution of structure in the Universe as a function of the distance (or redshift) from the Earth. It clearly shows filaments, voids and nodes inserted into a spiderweb configuration (Figure from [28]).

1.3 Universe overview

In this section we will define some of the fundamental equations that are going to be used throughout the review, which are the main component of the Universe and how they contributed to its evolution.

1.3.1 The FLWR metric

The Universe is expanding, but in order to describe mathematically this phenomenon, it is necessary to have the metric that describes the geometry of the Universe itself. There are three possibilities which manifest themselves with the different value of the parameter k [52]. If $k = 0$ the Universe is flat or Euclidean; if $k = 1$ it is closed; if $k = -1$ it is open. A simple representation can be found in Fig[1.7].

All the observation indicate that the most realistic scenario is a flat Universe and, as it will be discussed in the section [1.4], the explanation is already been discussed by cosmologists.

Before introducing the metric, it is important to mention the "Cosmological Principle" which states that the Universe is homogeneous and isotropic if large scales are considered (to give an estimate, consider scales larger than 100 Mpc). In other words, the principle states that there are no preferred places in the Universe. An expanding Universe homogeneous, isotropic and flat, can be described by the Friedmann–Lemaître–Robertson–Walker (FLRW). In general the formula is expressed in comoving coordinates and it is expressed by the following relation [52]:

$$ds^2 = -dt^2 + a(t)^2 \left[\frac{dr^2}{1 - kr^2} + r^2(d\theta^2 + \sin^2 \theta d\varphi^2) \right], \quad (1.5)$$

and since $k = 0$ because of the flatness, the metric becomes

$$\begin{aligned} ds^2 &= -dt^2 + a(t)^2 [dr^2 + r^2(d\theta^2 + \sin^2 \theta d\varphi^2)] \\ &= -dt^2 + a(t)^2 [dx^2 + dy^2 + dz^2]. \end{aligned} \quad (1.6)$$

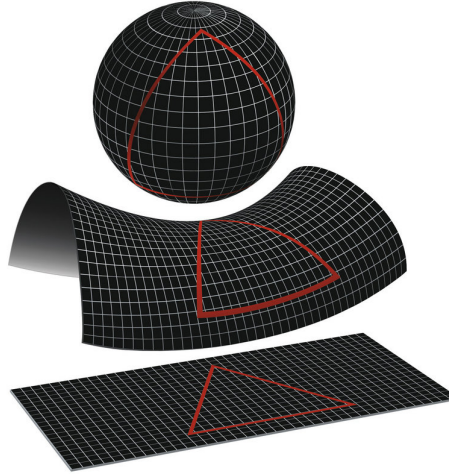


Figure 1.7: The three geometry that the Universe can show. From the top, it be closed ($k = 1$), open ($k = -1$) or flat ($k = 0$) (Figure from [156]).

Eq.1.6 is a metric with no perturbations, this means that it describes an empty Universe that is expanding. When gravitational perturbation will be taken into account in order to include matter sources, it will become slightly different as we will see in Chapter 3.

1.3.2 The Friedmann equations

In 1922, Alexander Alexandrovich Friedmann (Saint Petersburg 1888 - Leningrad 1925) used General Relativity, in particular Einstein's field equation (EFE), to obtain fundamental relation using only the hypothesis of a Universe homogeneous and isotropic.

Einstein's field equation relates the space-time geometry to its distribution of matter [52]. The equation is

$$R_{\mu\nu} - \frac{1}{2}Rg_{\mu\nu} + \Lambda g_{\mu\nu} = 8\pi G T_{\mu\nu}, \quad (1.7)$$

where $R_{\mu\nu}$ is the Ricci tensor, R the Ricci scalar, $g_{\mu\nu}$ the metric, Λ the cosmological constant and $T_{\mu\nu}$ the stress energy tensor and G is the Newtonian constant of gravitation $G = 6.67 \cdot 10^{-11} \text{ m}^3 \text{ kg}^{-1} \text{ s}^{-2}$.

It is easier and smarter to include the cosmological constant on the right-hand side of eq.1.7 because it is possible to generalize all the results to any form of DE.

In order to ensure homogeneity and isotropy, there cannot be a net momentum of the components of the Universe. The only quantities of interest are the energy density ρ and the pressure P of the different elements present in the Universe. In General Relativity, perfect fluids can be used to describe the distribution of matter since it respects the condition of homogeneity and isotropy. The 4-velocity of the fluid in its rest frame is $u^\mu = (1, 0, 0, 0)$ and, considering the density and pressure in that frame, the stress-energy tensor is $T_{\mu\nu} = (P + \rho)u_{\mu u}u_{\nu u} + Pg_{\mu\nu}$ or, in the matrix form, can be written as [52]:

$$T^\mu{}_\nu = \begin{pmatrix} -\rho & 0 & 0 & 0 \\ 0 & P & 0 & 0 \\ 0 & 0 & P & 0 \\ 0 & 0 & 0 & P \end{pmatrix}. \quad (1.8)$$

Applying the FLRW metric to the EFE, Friedmann obtained 2 independent equation that are the pillars of modern cosmology. The first one is obtained by the 00 component of EFE, while the second from the ij component [52, 65]. For completeness, here it is included also the curvature parameter k :

$$\begin{cases} H^2 = \frac{8\pi G}{3}\rho - \frac{k}{a^2} \\ \ddot{a}/a = -\frac{4\pi G}{3}(\rho + 3P) \end{cases}, \quad (1.9)$$

Actually, there is another relation that can be obtained by the combination of the system [1.9] and it is given by

$$\dot{\rho} + 3H(\rho + P) = 0. \quad (1.10)$$

In order to solve the system, that involve 3 unknown quantities namely $a(t)$, $\rho(t)$ and $P(t)$, another independent relation is required. This equation is the equation of state $P = P(\rho)$ that take the form of $P = \omega\rho$ [52].

The values of ω , the equation of state parameter, are essential to establish which component is the subject of study. It assumes values: $\omega = 0$ when it is attributed to non-relativistic matter; $\omega = 1/3$ to describe radiation; $\omega = -1$ in order to characterize a cosmological constant.

By plugging in the equation of state in eq.[1.10], the resulting relation is a simple differential equation of the first order that can be solved by separating the variable

$$\frac{\dot{\rho}}{\rho} = -3(1 + \omega)\frac{\dot{a}}{a}. \quad (1.11)$$

And the final result is an important relation between the energy density and the scale factor. Even before the computation, it is possible predict what the dependence $\rho - a$ will be in each case. Non-relativistic matter preserves the number of particle, so the energy density will be inversely proportional to a volume in expansion. Radiation will be subject to the same effect, however, another consequence must be taken into account: the redshift. For this reason, radiation will have a energy density with a slightly different dependence on the scale factor. The easiest case is the cosmological constant one, since, by definition, the energy density is conserved. to summarize [52] [65]:

$$\rho \propto a^{-3(1+\omega)} = \begin{cases} a^{-3} & \text{for non-relativistic matter} \\ a^{-4} & \text{for radiation} \\ \text{constant} & \text{for a cosmological constant} \end{cases}. \quad (1.12)$$

1.4 Inflation

The Concordance Model of Cosmology had some shortcomings that cosmologists couldn't explained. There were three problems which are now rapidly being introduced and which have been answered by the introduction of a primordial phase called inflation.

1.4.1 The Flatness problem

If the curvature parameter is equal to 0 as in the FLRW metric [1.6] than the first equation of the system [1.9] can be used to obtain the critical density ρ_{crit} , by definition the density required for the Universe to be flat [52]

$$\rho_{crit} = \frac{3}{8\pi G}H^2. \quad (1.13)$$

The current value of this density is $\rho_{crit} = 8.45 \cdot 10^{-27} \text{kg m}^{-3}$ and thanks to this, it is possible to introduce the density parameters $\Omega_i = \rho_i/\rho_{crit}$. The subscript i refers to the different constituents of the Universe, namely ordinary matter, DM, radiation and DE.

Taking again the first Friedman equation and dividing everything by H^2 , a relation between the curvature and the density parameter is then obtained

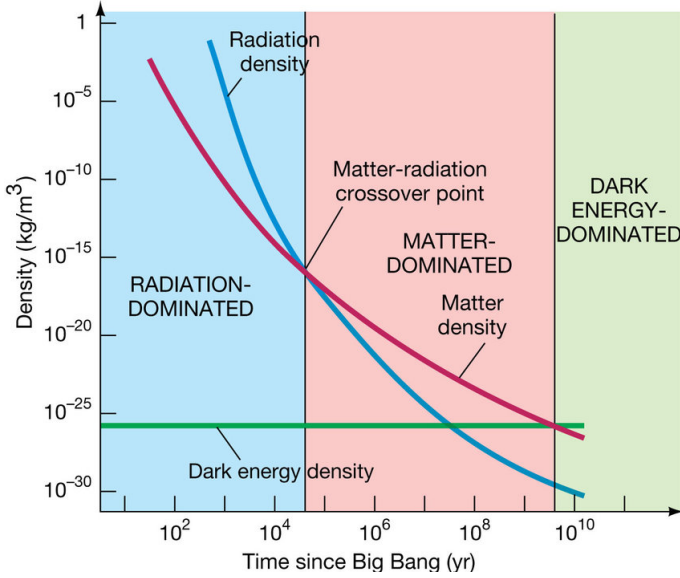


Figure 1.8: The early stages of the Universe were dominate by radiation. Then, ρ_{mat} became greater than ρ_{rad} and the Universe became matter dominated. Today the Universe is dominated by the cosmological constant energy density (Figure from [120]).

rho

$$\Omega - 1 = \frac{k}{a^2 H^2} = k r_H^2. \quad (1.14)$$

Although so far in this work the Universe has been considered flat, cosmological observation find out the current value of Ω_0 is not perfectly equal to 1, but it is $\Omega_0 = 1.0007 \pm 0.0037$ [135] and since the comoving Hubble radius r_H^2 is a time-dependent function, it is possible to give an estimate to Ω in different eras. It turns out that $|\Omega - 1|$ has always been very close to zero, without reaching it. In early times, the Universe was radiation dominated and then become dominated by non relativistic particle. Since it is known the dependency of the scale factor with respect to time, it is known also the dependency of $\Omega - 1$ with respect to time [65]

$$\Omega - 1 = k r_H^2 \implies r_H = (aH)^{-1} \propto \begin{cases} t^{1/2} & \text{radiation dominated era} \\ t^{1/3} & \text{non-rel matter dominated era} \end{cases}. \quad (1.15)$$

A tiny deviation from flatness, for example, at Plank time ($t \sim 10^{-43}$ s) would implied a current value of Ω strongly different from 1, since the Hubble radius increases with time. For this reason $|\Omega - 1|$ has to be fine-tuned very close to 0 in order to explain the current value [68].

Inflation was a phase of exponential expansion (called "De Sitter expansion") in the very beginning of the Universe in which its size became ~ 60 order of magnitude larger in a time between $t \sim 10^{-36}$ s and $t \sim 10^{-33}$ s after the Big Bang. This phase is characterized by the decrease of r_H and it is in agreement with the presence of a cosmological constant [65]. To see this consider

$$r_H' < 0 \implies r_H' = \frac{d}{dt} \left(\frac{1}{\dot{a}} \right) = -\frac{\ddot{a}}{\dot{a}^2} \implies \ddot{a} > 0. \quad (1.16)$$

This condition, when inserted in the second Friedmann eq [1.9] and using the equation of state $P = \omega \rho$, translate in the condition $\omega - 1/3$ which is the case of a cosmological constant ($\omega = -1$) which is characterized by an exponential expansion.

During this period, the comoving Hubble radius is required to decrease. In this way, even if the value of $|\Omega - 1|$ was very different from 0 at the beginning of inflation, it gets closer and closer to 0 toward the Plank time. Using the fact that $(\Omega - 1)\rho a^2$ is a constant, it is possible to write the ratio between the density parameter in terms of ratio of the product ρa^2 , or, using the relation [1.12], only in terms of ratio of scale factors. In the end, the result is given by [65]:

$$\frac{|\Omega(t_f) - 1|}{|\Omega(t_i) - 1|} = \left(\frac{a_i}{a_f} \right)^2 = e^{-2N}, \quad (1.17)$$

with N is the number of e-folds, a parameter used to quantify the inflationary exponential expansion. N turns out to be $\sim 60 - 70$ in order to give a value of $|\Omega(t_f) - 1|$ extremely close to 0.

1.4.2 The Horizon problem

This problem is related to the fact that two regions of the sky can be causally connected or not. A photon can travel a finite distance in a given time t . All the possible directions of motion of this photon form its particle horizon. All the observable Universe is contained in our particle horizon. The most remote surface that is observable is the last scattering surface at $z \sim 1100$ that correspond to the epoch when photons decoupled from the primordial plasma. The image is the CMB map in Fig 1.5. A property of that map is that these randomly distributed photons have all the same temperature of $\sim 2.7 K$ within a very small error. Having the same temperature is a requirement for thermal equilibrium, however, this should not be possible in principle [52] [65].

The comoving Hubble radius is the comoving displacement travelled by light in an Hubble time H^{-1} . The time dependence of r_H scale according to eq 1.15, so a volume defined by that radius, the comoving Hubble horizon, will start its expansion from a small size. An arbitrary comoving region will therefore be larger than the comoving Hubble horizon for a interval of time. This condition is called "super-horizon" regime. In this period it is impossible for that region to be causally connected since there cannot be interactions in the whole region.

Inflation solved the problem, since as already saw in the previous section, the comoving Hubble radius decreases with time during this period and so the region is initially causally connected and able to reach thermal equilibrium while in the sub-horizon regime [65].

In Fig 1.9 it is represented the inflationary effect for an arbitrary region of size $\lambda \propto k^{-1}$

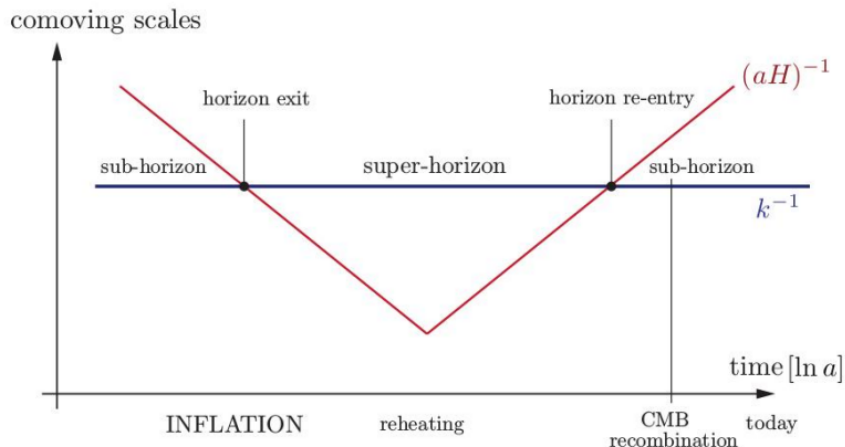


Figure 1.9: The inflationary solution add a phase of shrinking of the Hubble comoving radius (red line). In this way, a region of comoving size $\lambda \sim k^{-1}$ (blue line) will be initially in a sub-horizon regime, able then to reach equilibrium. After the end of inflation, at reheating, the comoving Hubble radius start to increase and the condition of the region remain freezed since throughout the duration of the super-horizon condition (Figure from [111]).

1.4.3 The Unwanted Relics Problem

In order to explain briefly this problem, it is necessary a mention to the Standard Model of Particle Physics. Interactions between particles are divided into four categories driven by as many forces:

- Strong nuclear;
- Weak nuclear;
- Electromagnetic;
- Gravitational.

Each one, except for the gravitational force, is well represented by a group that determine a symmetry. The simplest example are the ferromagnetic materials. In normal condition, the magnetic spins are oriented randomly and a rotation around any of the three spatial axis do not change the total orientation of those spins. The group that characterize the invariance under spatial rotations is the $SO(3)$. However, if the temperature drop below a critical value, the Curie temperature, the spins align in a specific direction. It means that only the rotation around one specific axis, parallel to the total spin, is possible. The $SO(3)$ symmetry is then spontaneous broken into the $U(1)$. The symmetry breaking is spontaneous (SSB) since the Lagrangian of the system is not explicit perturbed and remain the same.

In the Standard Model of Particle Physics, the electromagnetic force and the weak nuclear force, merged into the electroweak interaction if high energies are considered, or, in other words, when the temperature of the Universe was higher in the past. In the same way, physicists like Howard Georgi and Sheldon Glashow [64] tried to propose that in the early Universe, when the temperature was extremely high, there was only one force that, with the cool down of the Universe, split through SSB into the interaction known today. This is the basis for the Grand Unification Theories (GUT) which are still being studied today [138].

The unwanted relics problem arises from the fact that a SSB require the formation of a particle called Goldstone boson. The details of these processes are not the purpose of this work, but the danger was that the density of these particles coming from the subsequent SSB could affect Ω to be much larger than 1. Inflation is then needed, since the exponential expansion "diluted" those unwanted relics.

1.4.4 The dynamics of inflation

This section is used to introduce quantities that will be essential for the next chapters, like the potential of the inflaton and its stress energy tensor.

Inflation cannot be driven by some cosmological constant, as it would lead to infinite exponential expansion. Inflation has to end at some point to enter the age of radiation. The simplest way to generate such a transition is through the potential energy of a single scalar field, although there are many models that use multiple fields.

Let be ϕ the scalar field with a small mass m given by a SSB. The action of this field is given by [79]

$$\mathcal{S}[\phi] = \int d^4x \sqrt{-g} \mathcal{L}[\phi, g_{\mu\nu}], \quad (1.18)$$

where \mathcal{L} is the Lagrangian density, for which one of the simpler forms was chosen:

$$\mathcal{L}[\phi, g_{\mu\nu}] = -\frac{1}{2}\partial_\mu\phi\partial^\mu\phi - V(\phi). \quad (1.19)$$

The Lagrangian density involves the potential of the field $V(\phi)$. For the choice of $V(\phi)$ there is a large number of possible potential candidate and to choose one of those, it is required the concept of slow-roll. The most famous scenario of inflation is indeed the "slow-roll" model [98] which require that the scalar field moves slowly toward its true ground state. To quantify this, it is introduced the first slow roll parameter ϵ_{sr} [65]

$$\epsilon_{sr} = \frac{m_{pl}^2}{16\pi} \left(\frac{\partial_\phi V}{V} \right)^2 \ll 1. \quad (1.20)$$

Having now this parameter, it is possible to chose the potential according to the model to be used [15].

There can be the so-called "Large field models" in which ϕ is bigger than the Planck mass (which is around 10^{19} GeV). This condition arises from eq. 1.20 since this kind of model shows a potential of the form $V(\phi) \sim \phi^\alpha$. The condition becomes $m_{pl}/\phi \ll 1$.

There can be also "Small field models" that require ϕ to be smaller than M_{Pl} for the same condition $\epsilon \ll 1$. The potential this time assumes the form

$$V(\phi) = V_0 \left(1 - \left(\frac{\phi}{\mu} \right)^p \right), \quad (1.21)$$

where μ is a parameter related to ϕ , while p is a natural number greater than 2. Computing $\partial_\phi V$ and inserting it into eq. 1.20, the condition for small field models is indeed that $m_{pl}\phi^{p-1} \ll 1$.

A comparison between these two models can be found in Fig. 1.10

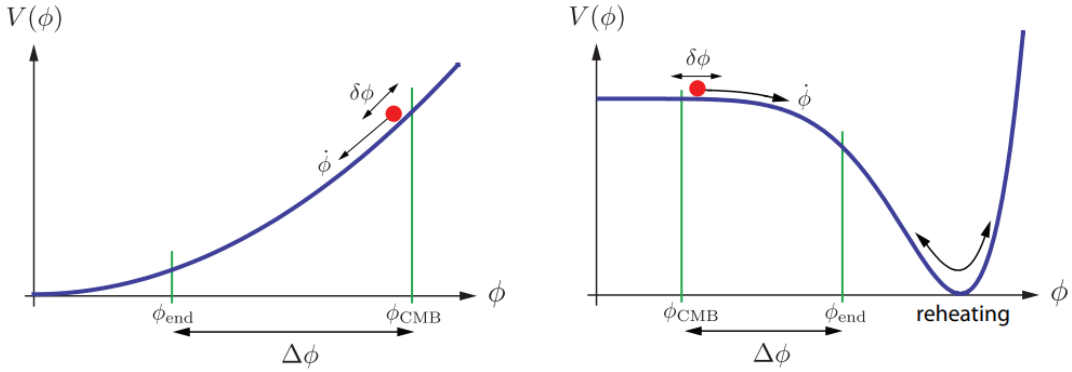


Figure 1.10: Example of Large Filed Model (left) and Small Field Model (right). ϕ_{CMB} refers to the value of the inflaton when the fluctuation on the CMB were formed at the beginning of the super-horizon regime, while ϕ_{end} refers to the second cross of the comoving Hubble horizon. $\Delta\phi$ in the excursion that the field had suffered during the 60 – 70 e-folds. Small Field Models end with the oscillations of the inflaton around the ground state that produced light in the decay process. This phase is called "reheating" and determines the start of the radiation dominated era (Figure from [15]).

It is worth to mention the existence of hybrid models, however they include a second scalar field, and so they are neglected in this work.

To conclude, it is also useful computing the stress-energy tensor of the inflaton ϕ [104]

$$T_{\mu\nu} = -\frac{2}{\sqrt{-g}} \frac{\delta S}{\delta g^{\mu\nu}}. \quad (1.22)$$

In the last equation, the derivative is the functional one. The action is given by eq. 1.18 and the Lagrangian density by eq. 1.19, can be taken.

Since the Lagrangian density is dependent only on $g_{\mu\nu}$ the functional derivative in eq. 1.22 gives

$$\begin{aligned} T_{\mu\nu} &= -\frac{2}{\sqrt{-g}} \left[\frac{\partial}{\partial g^{\mu\nu}} (\sqrt{-g} \mathcal{L}) \right] \\ &= -\frac{2}{\sqrt{-g}} \left[\frac{\partial \sqrt{-g}}{\partial g^{\mu\nu}} \mathcal{L} + \sqrt{-g} \frac{\partial \mathcal{L}}{\partial g^{\mu\nu}} \right] \\ &= -\frac{2}{\sqrt{-g}} \left[-\frac{1}{2} \sqrt{-g} g_{\mu\nu} \mathcal{L} + \sqrt{-g} \frac{\partial \mathcal{L}}{\partial g^{\mu\nu}} \right] \\ &= -2 \frac{\partial \mathcal{L}}{\partial g^{\mu\nu}} + g_{\mu\nu} \mathcal{L} \\ &= \partial_\mu \phi \partial_\nu \phi + g_{\mu\nu} \left[-\frac{1}{2} g^{\alpha\beta} \partial_\alpha \phi \partial_\beta \phi - V(\phi) \right]. \end{aligned} \quad (1.23)$$

In the third line, the fact that $\partial\sqrt{-g}/\partial g^{\mu\nu} = -\frac{1}{2}\sqrt{-g} g_{\mu\nu}$ was exploited.

It is known from eq. 1.8 that the component T^0_0 is related to the energy density, and the component T^i_j is related to the pressure. In the end, recalling homogeneity and isotropy, the diagonal components of the stress-energy tensor are

$$T^0_0 = g^{00}T_{00} = -\left(\frac{1}{2}\dot{\phi}^2 + V(\phi)\right) = -\rho(t), \quad (1.24)$$

$$T^i_j = g^{ik}T_{kj} = \frac{1}{2}\dot{\phi}^2 - V(\phi) = P(t). \quad (1.25)$$

So the energy density and pressure can be written in the following way

$$\rho = \frac{1}{2}\dot{\phi}^2 + V(\phi), \quad (1.26)$$

$$P = \frac{1}{2}\dot{\phi}^2 - V(\phi). \quad (1.27)$$

For inflation to happen, the equation of state must be negative ($\omega < -1/3$) and so the pressure must be negative too. From eq. 1.27 it is easy to see that the pressure have a negative sign if the potential term is greater than the kinetic one. This gives another condition for the slow roll [15]:

$$\frac{1}{2}\dot{\phi}^2 \ll V(\phi). \quad (1.28)$$

Chapter 2

Dark Matter

With only the Standard Model of Particle Physics and the knowledge acquired from cosmology, the Hot Big Bang model was not sufficient to explain all the observations. It was necessary to go beyond the knowledge of the time and add to the concordance model of cosmology other main ingredient. In particular, three main concept have been added [52]:

- Inflation, as already seen in the 1.4 section, solved the horizon, flatness and unwanted relics problems through an inflaton-driven exponential expansion ending with the reheating phase;
- Non-baryonic DM is the main source of matter in the Universe and the evidences of its existence are currently accepted and studied. However, its nature is still unknown;
- DE represents the largest contribution to the total energy density of the Universe and the current expansion of the Universe is driven by this source of energy.

Thanks to Planck Collaboration [135], the current density parameter are available and, although small discrepancies are present in the same values for different measurements depending on the technique used to compute them, it is possible to give a rough estimates of the extent of these parameters. Total matter, DM and DE are denoted by the indices m , DM and Λ respectively

$$\begin{aligned}\Omega_m &= \frac{\rho_m}{\rho_{crit}} \sim 0.315, \\ \Omega_{DM} &= \frac{\rho_c}{\rho_{crit}} \sim 0.265, \\ \Omega_\Lambda &= \frac{\rho_\Lambda}{\rho_{crit}} \sim 0.685.\end{aligned}$$

The Ω_{DM}/Ω_m ratio reveals that more than the 80% of the matter in the Universe is non-baryonic and this type of matter represents the $\sim 26\%$ of the total energy density, while the ordinary one contributes only for the $\sim 5\%$.

There are a lot of observational evidences of the existence of DM. Just to mention the most robust evidence, if DM did not exist, then galaxy rotational curves would be a puzzle that could not be solved [100]. This evidence is simple to understand, because it is sufficient to observe that there is not enough luminous matter in a galaxy in order to justify the measured rotational curve that can be observe in Fig 2.1. It is known that a star orbiting around the center of a spherically symmetrical galaxy should have a keplerian velocity $v(r) = \sqrt{GM(r)/r}$. However, as Fritz Zwicky first observed in 1933 [175], the velocity seemed to suggest that the total mass contained within a given radii r was way bigger than what was normally expected considering only the luminous matter. Indeed, galaxies are surrounded by halos of DM.

It is currently unknown what DM actually is or how it was formed. However, it is known that it interacts only through gravitational forces and does not emit electromagnetic radiation. The only property observable is the effect of DM, as a source of generic matter perturbs space-time and influences the objects that sense that change in the gravitational field. An example of this is the phenomenon of gravitational lensing visible in Fig 2.2. The trajectories of photons are deflected

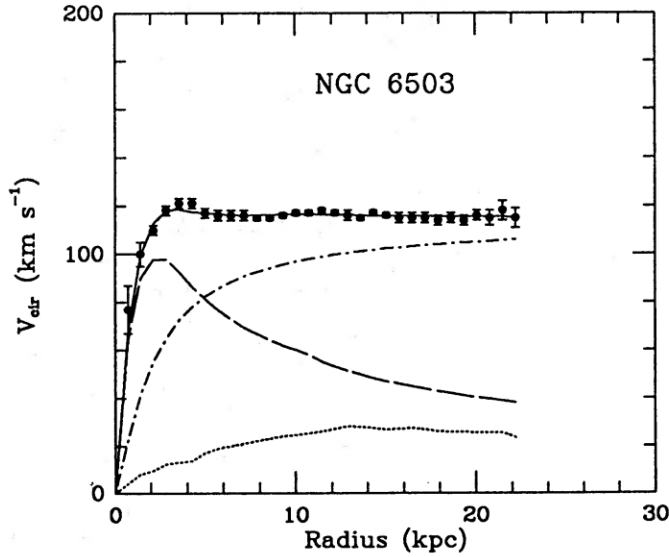


Figure 2.1: Rotational curve of the dwarf spiral galaxy NGC 6503. The plot shows four different curves: the dotted line represents the contribution of the gas, the dashed line of the visible disk, while the dash-dot curve portray the dark halo presence. The sum of these components gives the actual rotational curves coherent with the observations. This is a clear evidence that the keplerian velocity of luminous elements by themselves gives a profile that heavily underestimate the rotational velocity of the galaxy and so there must be something massive that does not emit electromagnetic radiation i.e. DM [21].

by the perturbations in space-time due to the presence of massive objects and therefore we can observe objects that would normally be impossible to see [100, 52].

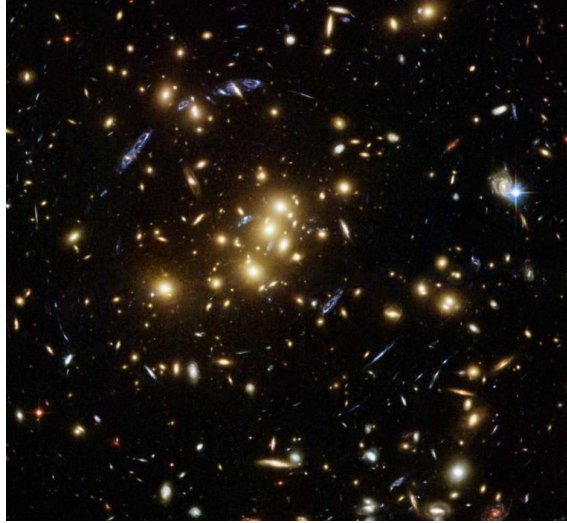


Figure 2.2: Gravitational lensing effect around the galaxy cluster CL0024+17. The yellow elliptical luminous galaxies are part of the cluster and around them it is present a "ring" in which other objects appear to be squeezed. This is due to the presence of a DM halo that perturbs space-time around the cluster and makes observable what is behind that cluster. The more DM is present, the more enhanced is the perturbation (Figure from [105]).

The fact that DM exerts only gravitational interaction with ordinary matter, means that it is

decoupled from every other species in the Universe. This can lead to think that after the formation of those particles in the early Universe, they stayed in equilibrium with the plasma for a certain amount of time until the expansion rate H became too large to allow interactions of DM and so it decoupled.

2.1 The genesis of Dark Matter

The process that describe the production of DM particles is analogous to Baryogenesis [45], the process who gave birth to baryon right after the end of inflation in the early Universe.

2.1.1 The evolution of the particle density

The interest in particle analysis is directed towards the whole rather than the individual elements. For this reason, statistics play an extremely important role. The equation that expresses the departure of Universe from thermal equilibrium is the Boltzmann equation.

It is important to emphasize again the relevance of the relation between the interaction rate and the Hubble constant:

- $\Gamma \geq H \Rightarrow$ Thermal equilibrium established or maintained;
- $\Gamma \leq H \Rightarrow$ The interaction described by Γ is inefficient.

Since the Boltzmann equation involve statistics, it is required a phase-space distribution of a given particle specie. Given a infinitesimal volume element dx^μ , the distribution function $f(x^\mu, p^\mu, t)$ identifies the number of particles of a given species within the infinitesimal momentum-space dp^μ element. The relation used to obtain the usual Boltzmann equation is given by the rate of change of this distribution [52] [100]

$$L[f] = C[f]. \quad (2.1)$$

$L[f]$ is the Liouville operator and it is equal to $df/d\lambda$. If the affine parameter λ is chosen to be time, then $L[f]$ represents the variation over time of the number of particles in the phase-space volume considered, while $C[f]$ is the collision operator, responsible for the change of the number of particle in the volume. A collisionless system has $C[f] = 0$.

Imposing the normalization $g_{\mu\nu}p^\mu p^\nu = -1$, the covariant relativistic expression of eq.2.1 is given by the relation [95]

$$L[f] = \left[p^\mu \frac{\partial}{\partial x^\mu} - \Gamma^\alpha{}_{\beta\gamma} p^\beta p^\gamma \frac{\partial}{\partial p^\alpha} \right] f. \quad (2.2)$$

Since the metric considered is the FLRW (eq.1.6), then the distribution $f(x^\mu, p^\mu, t)$ can be written as $f(\mathbf{x}, t, |\mathbf{p}|, \hat{p}, E, t)$. Due to homogeneity and isotropy, \mathbf{x} and \hat{p} respectively can be neglected. Moreover, the relativistic relation $E^2 = p^2 + m^2$ links E and $|\mathbf{p}|$. The distribution in the end will be $f = f(x^0, p^0) = f(t, E)$. The Christoffel symbols are given by the relation

$$\Gamma^\mu{}_{\alpha\beta} = \frac{1}{2} g^{\mu\nu} (g_{\alpha\nu,\beta} + g_{\beta\nu,\alpha} - g_{\alpha\beta,\nu}). \quad (2.3)$$

Using the FLRW metric in eq.2.3, it gives $\Gamma^0{}_{ij} = \delta_{ij} a \dot{a}$ and $\Gamma^i{}_{0j} = \Gamma^i{}_{j0} = \delta_j^i \dot{a}/a$. Now it is possible to explicit eq.2.2 with the correct dependencies of the distribution function.

$$\begin{aligned} L[f] &= \left[p^0 \frac{\partial}{\partial x^0} + p^i \frac{\partial}{\partial x^i} - \Gamma^0{}_{ij} p^i p^j \frac{\partial}{\partial p^0} - 2\Gamma^i{}_{0j} p^0 p^j \frac{\partial}{\partial p^i} \right] f \\ &= \left[p^0 \frac{\partial}{\partial x^0} - \Gamma^0{}_{ij} p^i p^j \frac{\partial}{\partial p^0} \right] f \\ &= \left[E \frac{\partial}{\partial t} - \delta_{ij} a p^i p^j \frac{\partial}{\partial E} \right] f \\ &= \left[E \frac{\partial}{\partial t} - H p^2 \frac{\partial}{\partial E} \right] f, \end{aligned} \quad (2.4)$$

where it has been defined p^2 as $g_{ij}p^i p^j = a^2 \delta_{ij}p^i p^j$ and used the definition of Hubble constant.

To proceed, it is introduced one of the momenta of the distribution function i.e. the number density of the given species of particles [47, 100]:

$$n = \frac{g}{(2\pi)^3} \int d^3p f. \quad (2.5)$$

In this equation g is the internal degrees of freedom (d.o.f.), a parameter that describes the system. For example, photons have 2 polarization (right or left circular polarization), so $g = 2$. Combining eq[2.1] with eq[2.4] multiplying by the constant $g/(2\pi)^3 E$ and integrating in d^3p :

$$\frac{\partial}{\partial t} \left(\frac{g}{(2\pi)^3} \int d^3p f \right) - H \frac{g}{(2\pi)^3} \int d^3p \frac{p^2}{E} \frac{\partial f}{\partial E} = \frac{g}{(2\pi)^3} \int d^3p \frac{1}{E} C[f]. \quad (2.6)$$

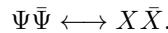
It is possible to recognize the time derivative of the number density in the first term. To obtain a more easy form of the Boltzmann equation, the second term should be written in another way. For this reason, using the homogeneity and isotropy proprieties, one could note that $d^3p = 4\pi p^2 dp$ and since $E^2 = p^2 + m^2$ it is true that $EdE = pdp$ [100]. The second term in eq[2.6] can be written as

$$\begin{aligned} H \frac{g}{(2\pi)^3} \int d^3p \frac{p^2}{E} \frac{\partial f}{\partial E} &= H \frac{4g\pi}{(2\pi)^3} \int dp \frac{p^4}{E} \frac{\partial f}{\partial E} \\ &= H \frac{4g\pi}{(2\pi)^3} \int dp p^3 \frac{\partial f}{\partial p} \\ &= H \frac{4g\pi}{(2\pi)^3} \left[p^3 f \Big|_0^\infty - 3 \int dp p^2 f \right] \\ &= -3H \frac{4g\pi}{(2\pi)^3} \int dp p^2 f \\ &= -3H \frac{g}{(2\pi)^3} \int d^3p f = -3Hn(t). \end{aligned} \quad (2.7)$$

In the third step it is been used integration by parts and considered $f(\infty) = f(0) = 0$ since there are no particles with infinite or zero momentum. The Boltzmann equation is then [52, 47]

$$\dot{n}(t) + 3Hn(t) = \frac{g}{(2\pi)^3} \int d^3p \frac{1}{E} C[f]. \quad (2.8)$$

For DM, it is supposed the existence of a massive particle Ψ with its mass m_Ψ . This particle is chosen to be long-lived (i.e. with a life longer than the age of the Universe). The decay is not possible, so the only interaction allowed that change the number density of Ψ is the annihilation with its anti-particle $\bar{\Psi}$ that produce the pair $X\bar{X}$ included in the SM of Particle Physics [47]. It is considered then the process



This is a reaction of the type $1 + 2 \longleftrightarrow 3 + 4$. Since the goal is to observe the rate of change in the Ψ particle, the following computation is focused on the number density $n_1(t)$

The collision term of eq[2.8] is given by [100]

$$\int d\Pi_1 d\Pi_2 d\Pi_3 d\Pi_4 (2\pi)^4 \delta^4 [|M|_{34 \rightarrow 12}^2 f_3 f_4 (1 \pm f_1)(1 \pm f_2) - |M|_{12 \rightarrow 34}^2 f_1 f_2 (1 \pm f_3)(1 \pm f_4)]. \quad (2.9)$$

Eq[2.9] used the following notation

- $\delta^4 = \delta^4(p_1 + p_2 - p_3 - p_4) \longrightarrow$ it is present for the conservation of the 4-momentum;
- $d\Pi_i = \frac{g_i d^3 p_i}{(2\pi)^3 2E_i};$

- $|M_{AB \rightarrow CD}| \rightarrow$ it is the matrix element for the reaction $A + B \rightarrow C + D$. It is called the "amplitude" and it is linked to the probability;
- $(1 \pm f_i) \rightarrow$ Pauli blocking and Bose enhancement. Another term linked to the probability to form the i -particle. The sign "+" is for bosons, while "-" for fermions. This difference is due to the fact that it is easier to form bosons since they do not obey to the Pauli exclusion principle.

The problem of eq. 2.9 is that it is very difficult to solve, since if it is inserted into the r.h.s. of eq. 2.8, this leads to an integro-differential equation. Some assumptions are then needed [100]:

1. Time-reversal symmetry of the process $1 + 2 \rightarrow C + D$ makes sure that the amplitudes are equal $|M|_{34 \rightarrow 12}^2 = |M|_{12 \rightarrow 34}^2 = |M|^2$.
2. The kinetic equilibrium allows the use of the following formula as the distribution function

$$f = \frac{1}{\exp(\frac{E-\mu}{T}) \pm 1}, \quad (2.10)$$

which is the Bose-Einstein distribution for bosons (-) and the Fermi-Dirac distribution for fermions (+). The parameter μ is the chemical potential, the energy exchange in a process that perturbs the particle number of the given species.

3. The condition $T \ll E - \mu$ ensures the fact that terms like $(1 \pm f_i)$ in eq. 2.9 become of order 1. Taking eq. 2.10, if the exponential is too large, due to the fact that $T \ll E - \mu$, then the unity term can be dropped, and so

$$f \sim e^{\frac{\mu}{T}} e^{-\frac{E}{T}}. \quad (2.11)$$

That is the Maxwell-Boltzmann distribution [52, 100]. It is known that $E \gg T$ from hypothesis and so this means that $(1 \pm f_i) \sim 1$.

Eq. 2.8 can be rewritten as

$$\dot{n}_1 + 3Hn_1 = \int d\Pi_1 d\Pi_2 d\Pi_3 d\Pi_4 (2\pi)^4 \delta^4 \left[|M|^2 (f_3 f_4 - f_1 f_2) \right]. \quad (2.12)$$

For the conservation of energy it must be valid $E_1 + E_2 = E_3 + E_4$, and so

$$f_3 f_4 - f_1 f_2 = e^{-\frac{E_1+E_2}{T}} \left(e^{\frac{\mu_1}{T}} e^{\frac{\mu_2}{T}} - e^{\frac{\mu_3}{T}} e^{\frac{\mu_4}{T}} \right). \quad (2.13)$$

This last relation can be written in other way considering that eq. 2.11 can be inserted into the definition of number density in eq. 2.5:

$$n_i(t) = \frac{g_i}{(2\pi)^3} e^{\frac{\mu_i}{T}} \int d^3 p_i e^{-\frac{E_i}{T}}. \quad (2.14)$$

Eq. 2.14 involves the chemical potential, but if it is supposed local thermodynamics equilibrium, then $\exp(\mu/T)$ can be dropped. LTE is obtained when both kinetic and chemical equilibrium are established. The kinetic one is already been imposed, and the chemical one is equivalent to the condition $\mu_1 + \mu_2 = \mu_3 + \mu_4$ [52]

$$n_i^{eq}(t) = \frac{g_i}{(2\pi)^3} \int d^3 p_i e^{-\frac{E_i}{T}}. \quad (2.15)$$

Considering the relativistic and non-relativistic regime [52]

$$\begin{cases} n_i(t) = g_i \left(\frac{m_i T}{2\pi} \right)^{3/2} e^{-\frac{m_i}{T}} & \text{non-rel case } T \ll m_i, \\ n_i(t) = \frac{g_i}{\pi^2} T^3 & \text{rel case } T \gg m_i. \end{cases} \quad (2.16)$$

In the non-relativistic case, the most important element is the exponential, responsible for the Boltzmann suppression.

Using eq. 2.14 and eq. 2.15, it is true that $n_i/n_i^{eq} = \exp(\mu_i/T)$ and eq. 2.13 become

$$f_3 f_4 - f_1 f_2 = \left(\frac{n_3}{n_3^{eq}} \frac{n_4}{n_4^{eq}} - \frac{n_1}{n_1^{eq}} \frac{n_2}{n_2^{eq}} \right) \exp\left(-\frac{E_1 + E_2}{T}\right). \quad (2.17)$$

The last thing to do is introducing the thermally averaged cross section. In this case it refers to the process of annihilation [100]

$$\langle \sigma |v| \rangle = \frac{1}{n_1^{eq} n_2^{eq}} \int d\Pi_1 d\Pi_2 d\Pi_3 d\Pi_4 (2\pi)^4 \delta^4 |M|^2 \exp\left(-\frac{E_1 + E_2}{T}\right). \quad (2.18)$$

The Boltzmann equation that describes the typical production of DM with the reaction $\Psi\bar{\Psi} \longleftrightarrow X\bar{X}$ have some hypothesis [47]

- Initial symmetry: $n_\Psi = n_{\bar{\Psi}}$, $n_X = n_{\bar{X}}$,
- X and \bar{X} in LTE: $n_X = n_X^{eq}$; $n_{\bar{X}} = n_{\bar{X}}^{eq}$.

With these conditions, the Boltzmann equation is

$$\dot{n}_\Psi + 3Hn_\Psi = -\langle \sigma |v| \rangle [n_\Psi^2 - (n_\Psi^{eq})^2]. \quad (2.19)$$

2.1.2 The freeze-out mechanism

DM does not interact except with gravitational force. To make this possible, DM cannot be in equilibrium with other particles present in the Universe. In other words, DM is decoupled from those particles. In the early Universe, the primordial plasma contained all species in equilibrium, even DM particles. However, at some point in history, DM particles went out of equilibrium such that the current density parameter represent the $\sim 26\%$ of the total energy density in the Universe [55].

Remembering the stress-energy tensor in eq. 1.23, the continuity equation $\partial\rho/\partial t = 0$ and Euler equation $\partial P/\partial x^i = 0$ can be summarize by a single conservation law $\nabla_\mu T^\mu{}_\nu = 0$ [52]. Taking the covariant derivative of the $T^\mu{}_0$ component, the following relation arises

$$a^{-3} T \frac{\partial}{\partial t} \left[\frac{(\rho + P)a^3}{T} \right] = 0. \quad (2.20)$$

This means that the term in the square bracket must be a constant and can be rewrite as sa^3 . The parameter s is called entropy density and scales as a^{-3} . This entropy density is used to introduce the quantity $Y = n_\Psi/s$ that represents the number of Ψ particles in a comoving volume [52]. Considering that the Nucleosynthesis happened during the radiation era and the density of relativistic particles is

$$\rho = g_* \frac{\pi^2}{30} T^4, \quad (2.21)$$

so the entropy density is given by

$$s = \frac{\rho + P}{T} = g_{*s} \frac{2\pi^2}{45} T^3. \quad (2.22)$$

Here g_{*s} is the number of degrees of freedom of all the particles involved and it is been used the fact that for radiation $P = \rho/3$.

The l.h.s of eq. 2.19 can be rewritten as $s\dot{Y}$ [100, 47]. Moreover, the introduction of the variable $z = m_\Psi/T$ allow the change of the time derivative $\partial_t = zH\partial_z$. The z-derivative will be noted with the symbol $''$. The result is

$$Y' = -\frac{sz}{H(z=1)} \langle \sigma |v| \rangle [Y^2 - Y_{eq}^2]. \quad (2.23)$$

Since $H \propto \sqrt{\rho}$ for the Friedmann relation, it is also true that $H \propto T^2$ [52], and so $H z^2 = H(z=1)$. Recalling eq[2.21]:

$$H(z=1) = \left(\frac{8\pi G}{3} \rho \right)^{1/2} = \left(\frac{8\pi G}{3} \right)^{1/2} \left(\frac{\pi^2}{30} \right)^{1/2} g_*(z=1) T^2. \quad (2.24)$$

In eq[2.23] the term with Y represents the annihilation of the Ψ particle since it is a negative contribution to Y' , while the term involving Y_{eq}^2 acts for the inverse annihilation for the opposite reason.

Considering that a classic definition of the interaction rate is $\Gamma = n\sigma|v|$ [100] and the fact that $Y_{eq} \cdot s = n_\Psi^{eq}$, eq[2.23] can be arranged into the form

$$\frac{dY}{dz} \frac{z}{Y_{eq}} = -\frac{\Gamma}{H} \left[\left(\frac{Y}{Y_{eq}} \right)^2 - 1 \right]. \quad (2.25)$$

The l.h.s. of eq[2.25] can be seen as $\Delta Y/Y$, the relative change in the number of Ψ particles in a comoving volume. This fraction depend on the ratio between the interaction and expansion rate, or, in other words, to the efficiency of the annihilation process. At some point, the ratio will become very small due to the expansion of the Universe and so ΔY . The effect is that the number of DM particles per comoving volume is then frozen [55].

If the freeze-out happened when the particles were still relativistic ($z_f < 1$), then the DM is said to be "hot" (HDM model). The main particle of HDM would be massive neutrinos. HDM, however, cannot be the main DM source for several reasons as the too low density parameter or the failure to describe the formation of structure in the Universe ([137]).

2.1.3 Cold Dark Matter

When DM particles decoupled in the non-relativistic regime ($\Gamma \ll H$), then it is said to be cold. This type of DM is accepted in the Concordance Model of Cosmology since it could give an answer to many cosmological problems [52]. The decoupling is shown in Fig[2.3]

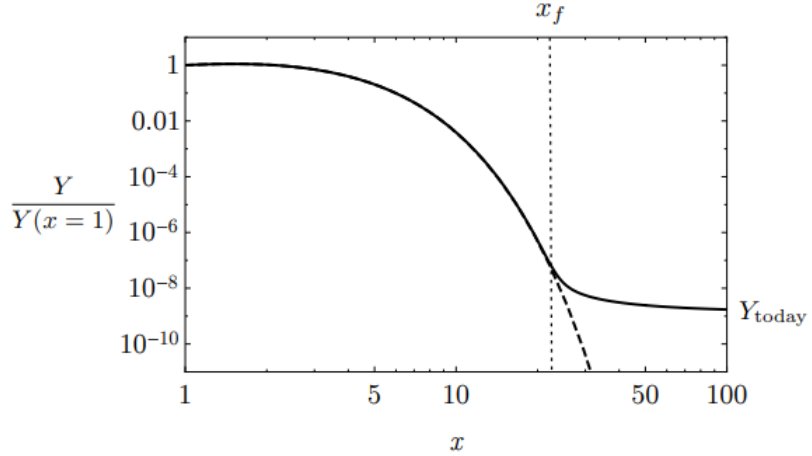


Figure 2.3: The plot represents the out-of-equilibrium scenario. The solid curve is the relative DM number density as a function of the auxiliary variable x . Before the freeze out, the number density matches the equilibrium distribution (dashed line). However, at $x = x_f$ the number density start to separate from the dashed line to reach the asymptotic value Y_{today} (Figure from [100]).

The thermally average cross section is temperature dependent ([100]), so it is possible to write $\langle \sigma|v| \rangle = \sigma_0 z^{-n}$ remembering that $z \propto T^{-1}$. Introducing a new parameter λ

$$\lambda = \frac{z^3 s \sigma_0}{H(z=1)} = const \cdot \frac{g_* s}{g_*(z=1)}, \quad (2.26)$$

and the difference $\Delta = Y - Y_{eq}$, it is possible to rewrite eq.2.23

$$\Delta' = -Y'_{eq} - \frac{\lambda}{z^{2+n}}(\Delta + 2Y_{eq})\Delta. \quad (2.27)$$

While before the freeze-out ($1 < z < z_f$) the distribution follows the equilibrium, Δ is very close to zero. The situation changes dramatically when DM decoupled at $z > z_f$ [100]. In this regime Y_{eq} and Y'_{eq} are exponentially suppressed and so $\Delta \sim Y$. Then

$$Y' \sim -\frac{\lambda}{z^{2+n}}Y^2. \quad (2.28)$$

By separating the variable, this equation can be integrated between the epoch of freeze-out until the very late times $Z = \infty$

$$\frac{1}{Y_\infty} - \frac{1}{Y_f} \sim \frac{\lambda}{n+1} z_f^{-n-1}. \quad (2.29)$$

Since $Y_f^{-1} < Y_\infty^{-1}$, it is finally obtained $Y_\infty \sim z^{n+1}(n+1)/\lambda$. The last thing to do is to compute the current density parameter. Having $n_{\Psi_0} = s_0 Y_\infty$, the density parameter obtained is [52]

$$\Omega_{\Psi_0} h^2 = 0.1 \left(\frac{z_f}{20} \right) \left(\frac{g_*}{100} \right)^{1/2} \frac{2 \cdot 10^{-26} \text{ cm}^3 \text{ s}^{-1}}{\langle \sigma | v | \rangle}. \quad (2.30)$$

The normalization of z_f is just an order of magnitude gives by numerical simulations (For example, $n = 0$ gives $z_f = 17$). For what concern the cross section, the normalization value is typical for weak interactions and this would give the exact amount of DM present in the Universe. This is known as the "WIMP miracle", Weakly Interactive Massive Particles.

2.2 Small scale issues

Even though CDM can successfully describe the evolution of the structure of the Universe and WIMPs could lead to the right density parameter, their existence of is still debated, as direct and indirect experiments for its detection have failed and so other candidate have arisen over the years. However, WIMPs have other problems other than not being detected. In particular, there are some controversies at small scales [167].

Two of the major conflicts between observations and theoretical predictions are known as the Missing Satellite Problem and the Core-Cusp Problem.

2.2.1 The Missing Satellite Problem

Galaxies are surrounded by halos of DM. These halos are filled by several subhalos that collapsed at early times and have preserved their identities after falling into larger DM regions since CDM preserve primordial fluctuations [171].

Λ CDM cosmology predicts that galaxies like the Milky Way should present a large number of satellite galaxies. However, observations suggest that those galaxies are much fewer than expected from N-body simulations.

Several possible explanations have been proposed over the years, including baryonic physics or modification of the nature of DM [167]:

- If the circular velocity of subhalos is greater than the critical value $v_c \sim 30 \text{ km s}^{-1}$, it will host a luminous galaxy. Only a fraction of halos with circular velocity less than v_c is luminous and therefore detectable [37];
- Stellar wind from first generation stars and supernovae may be the responsible for the gas leak from the potential well of low-mass halos. This would mean the impossibility of the formation of very bright objects, keeping the halo dark [37];

- Modification of DM, involving warm DM (WDM) [74] and self-interacting cold DM (SICDM) [152];
- Modification of the inflationary fluctuation spectrum [90].

Unfortunately, none of these possibilities could solve the missing satellite problem and if any of them were able to do so, other related problems would arise.

The main problem is that numerical simulations in the Λ CDM model predict too much DM in the central region of halos and subhalos. This fact is most evident when described in the context presented in the next section.

2.2.2 The Core-Cusp Problem

As already said, the circular velocity in a spherical matter distribution is given by $v(r) = \sqrt{GM(r)/r}$, however, there are relevant discrepancies between the observed and predicted velocity curves at small radii in typical galaxies.

The rotational velocity in the outer part of late-type disk galaxies appears to be roughly constant and this means that $\rho_{DM} \sim r^{-2}$ as in a isothermal sphere [32]. In the inner part, velocity and radius seems to increase linearly. This solid-body behavior suggest that DM presents a core in the central region of the halo. One of the density profile that respect this propriety is the pseudo-isothermal (PI) profile [162]

$$\rho_{PI}(r) = \frac{\rho_0}{1 + (r/R_c)^2}, \quad (2.31)$$

where ρ_0 is the central density, while R_c is the core radius. This means that the relation density-distance is the pseudo-isothermal profile is $\rho \sim r^\alpha$ with $\alpha = 0$

In 1997, thanks to N-body simulations, another profile started to be used as the standard equilibrium density profiles of collisionless CDM halos of all masses, the Navarro–Frenk–White (NFW) profile [113]

$$\rho_{NFW}(r) = \frac{\rho_i}{(r/R_s)(1 + r/R_s)^2} \quad (2.32)$$

The density of the Universe at the collapse of the halo is denoted ρ_i and the halo radius is R_s . This model predicts $\rho \sim r^\alpha$ with $\alpha = -1$ in the inner regions and $\alpha = -3$ in the outer regions.

The key difference between eq. 2.31 and eq. 2.32 is that the pseudo-isothermal profile gives an inner core of DM of constant density, whereas the NFW profile has a cusp where the density continue to increase as the radius decrease. This can be seen in Fig. 2.4

The PI profile is a better model than the NFW one, so it is more likely that halos and subhalos have a central core rather than a cusp. Even though it is still unknown the physical reason, also for this problem it is possible to make some hypothesis

- During the processes that took place in the galaxy formation phase, an adiabatic contraction of the inner DM region could be happened [30];
- The presence of the DM core can be justified if a large amount of baryon are expelled into the halo [114];
- Merging of gas clouds of masses between 10^5 and $10^8 M_\odot$ could have destroyed the cusps only if the interaction took place in the early Universe when the halos where smaller than today [170].

As in the Missing Satellite Problem, the issue is the excess of DM that the Λ CDM model predicts in the innermost region of the halos and subhalos. Higher resolution observation and detailed description of systematic effects are required then to make the situation clearer and find a possible solution that involve baryonic physics or a different DM behavior.

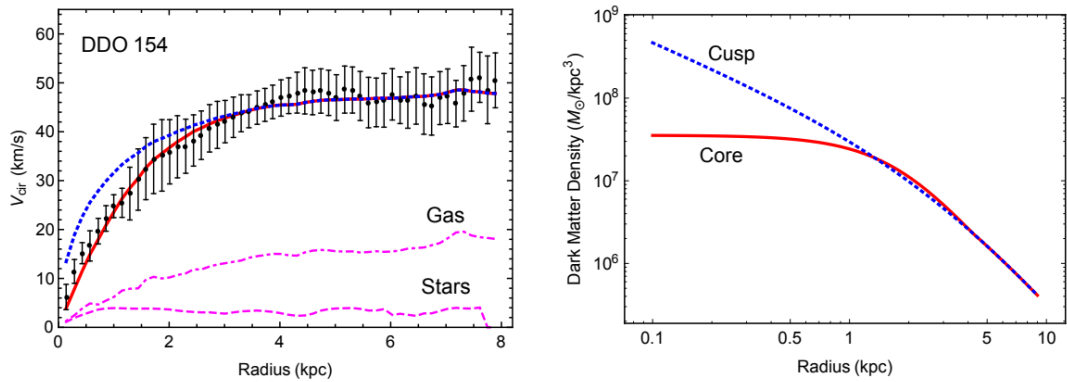


Figure 2.4: (Left) Rotational curve of the dwarf galaxy DDO 154. The blue line is the model involving a NFW profile that generate a inner cusp. The red curve is obtained thanks to a core profile. (Right) The DM density profile with a core and cusp model. For this NFW curve it has been used $R_S \sim 3.4 \text{ kpc}$ and $\rho_i \sim 1.5 \cdot 10^7 M_\odot/kpc^3$ (Figure from [162]).

Chapter 3

Fuzzy Dark Matter

The previous chapter ended with the suggestion that one possibility to find the solution of issues like the Missing Satellite Problem or the Core-Cusp Problem is to change the nature of DM. Λ CDM model involve collisionless cold DM and modification of the its nature were already been proposed in the early 2000 [74], [152]. A comparison between the formation scenario considering different types of DM can be found in Fig 3.1.

In the same time period, it was proposed another type of DM, the FDM [76]. This type of DM is made up by ultralight scalar particles without self-interactions. To reach today's value of Ω_{DM} , the mass of the standard FDM particle covers a range typically between 10^{-22} and 10^{-20} eV and, for this reason, the interest does not fall into its particle behavior, but on its wave properties. In general, when the mass of the main particle is below ~ 30 eV, we are referring to "Wave" DM ψ DM [78]

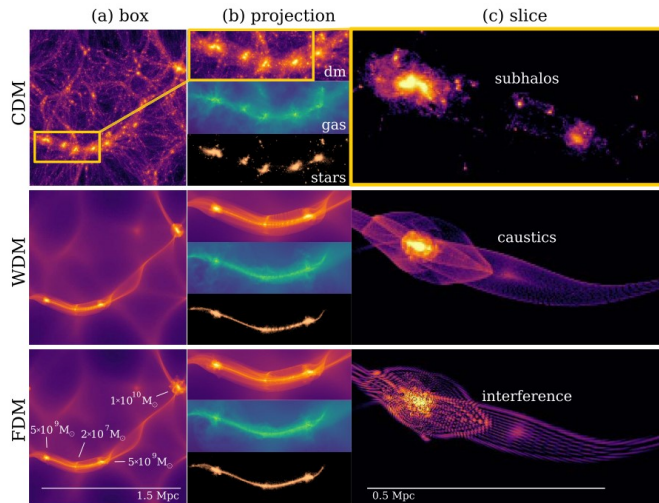


Figure 3.1: Structures of galaxy formation considering cos CDM, WDM and ψ DM. In column (a) it is plotted the projected DM distribution at redshift $z = 5.5$ in a box of size 1.5 Mpc; in column (b) a zoom of the filament-shape like structure separating DM, gas and star contribution; in column (c) the more detailed DM structure. As the mass of the DM field decrease from CDM to FDM models, the structure of DM tends to leave the spherical halo fragmentation into subhalos in order to form interference patterns as the DM wave nature becomes increasingly relevant (Figure from [109]).

3.1 The QCD Axion

One of the most common examples of ultra-light scalar candidates as FDM particle is the axion introduced by Peccei and Quinn [124]. The axion was first introduce as the solution of the strong CP problem.

CP is the combination of the charge conjugation symmetry C and the parity symmetry P. In principle, there is no reasons for strong interaction to respect this symmetry, so its violation is mathematically possible. However, the CP violation of strong interactions has never been observe in experiments.

The Lagrangian term that describes the CP violation of strong interaction is [104]

$$\mathcal{L}_{\theta,QCD} = \frac{\theta_{QCD}}{32\pi^2} \text{Tr } G_{\mu\nu} \bar{G}^{\mu\nu}, \quad (3.1)$$

where $G_{\mu\nu}$ is the gluon field strength, while $\bar{G}^{\mu\nu} = \epsilon^{\mu\nu\alpha\beta} G_{\alpha\beta}/2$ represent the problematic term for the CP symmetry, since $\epsilon^{\mu\nu\alpha\beta}$ is an anti-symmetric tensor. θ_{QCD} is a real number that parameterize the true vacuum of the system, also called θ -vacuum.

The violating term generates an electric dipole moment for the neutron. The entity of this moment was studied by inserting ultracold neutrons in a trap and permeating them with uniform electric and magnetic fields. The analysis gives an upper limit to the electric dipole moment of $|d_n| < 2.9 \cdot 10^{-26} e \text{ cm}$ at 90% C.L. [9].

Since the relation between the electric dipole moment and θ is $d_n \sim 3.6 \cdot 10^{-16} \theta_{QCD} e \text{ cm}$ [104], the upper limit on the moments reflects to an upper limit on θ . By the comparison of the two results, it is possible to ascertain $\theta_{QCD} < 10^{-10}$.

This extremely low value highlights a fine-tuning problem. A possible solution is given by Peccei and Quinn [124]. They introduced a symmetry called $U(1)_{PQ}$ which spontaneously broken at some energy scale f between 10^9 and 10^{17} GeV [104]. Whenever a symmetry is spontaneously broken, a Goldstone boson is released and the particle originated from the $U(1)_{PQ}$ SSB is the QCD axion.

3.2 Classical Field Justification

Noted with \bar{r} the interparticle separation, it is known that this parameter is dependent on $n^{-1/3}$, with n the number density.

It is given that the DM density in the neighborhood of the Solar System is $\rho_{DM,\odot} = 0.4 \text{ GeV/cm}^3 = 4 \cdot 10^{23} \text{ eV/km}^3$ [78]. This means that, if it is known the mass of DM, the number density $n = \rho_{DM,\odot}/m_{DM}$ can be found.

The starting point is to compute the de Broglie wavelength that tell the scale at which wave properties are relevant fot the particle

$$\begin{aligned} \lambda_{dB} &= \frac{2\pi}{mv} \hbar c^2 = 1.49 \left(\frac{10^{-6} \text{ eV}}{m} \right) \left(\frac{250 \text{ km/s}}{v} \right) \text{ km} \\ &= 0.48 \left(\frac{10^{-22} \text{ eV}}{m} \right) \left(\frac{250 \text{ km/s}}{v} \right) \text{ kpc}. \end{aligned} \quad (3.2)$$

In this formula, v is the statistical dispersion of velocities about the mean velocity for a group of astronomical objects.

Now, the relation that has to be considered is the case in which $\lambda_{dB} < \bar{r}$. The ratio in eq.3.2 involving the velocity dispersion is approximated to be of order 1. In this case, since $\bar{r} = (m/\rho)^{1/3}$ the inequality gives the upper bound

$$m < (1.49 \cdot 10^{-6} \rho^{1/3})^{3/4} \text{ eV} \sim 34 \text{ eV}.$$

This low value of DM mass allows to consider DM field as a classical field. This can be seen thanks to the following consideration. The number of particles in a de Broglie volume is given by $N = nV = n\lambda_{dB}^3 = \rho\lambda_{dB}^3/m$. Using (3.2), N is given by

$$N = 0.99 \left(\frac{34\text{eV}}{m} \right)^4 \left(\frac{250 \text{ km/s}}{v} \right)^3.$$

However, since $m \ll 34\text{eV}$ due to the fact that fuzzy DM is considered, the occupancy N is so high that DM must be bosonic, since fermions obey to the Pauli exclusion principle [91].

With the introduction of a quantum state $\hat{\psi}$, it is possible to split it into $\hat{\psi} = \psi + \delta\hat{\psi}$, the expectation value in a given state and the relative quantum corrections. For a coherent state, which is a state with similar behavior of a classic harmonic oscillator that describes the oscillating motion of a particle in a quadratic potential well, the occupancy for modes of the typical wavelength obey to [76]

$$\frac{1}{\sqrt{N}} = \frac{\delta\hat{\psi}}{\psi}.$$

So if N is too high (boson), then $\delta\hat{\psi} \ll \psi$ and the approximation to consider the field as a classical one is justified.

3.3 Unperturbed Klein-Gordon Equation

Since the mass of the FDM is extremely low, it is natural to choose a potential for a small field like in eq[1.21], and, in particular, the potential for the axion is

$$V(\phi) = \Lambda^4 \left(1 - \cos\left(\frac{\phi}{f}\right) \right). \quad (3.3)$$

The ratio in the cosine is an effective angle, and f is an high energy level as already said. The square of the mass of the field is given by the second derivative of V with respect to ϕ , calculated in $\phi = 0$, so $m^2 = \Lambda^4/f^2$ [78].

Since f is very high and ϕ is lower than this energy scale, the cosine can be expanded

$$\cos\left(\frac{\phi}{f}\right) \sim 1 - \frac{1}{2!} \left(\frac{\phi}{f}\right)^2 + \frac{1}{4!} \left(\frac{\phi}{f}\right)^4 - \frac{1}{6!} \left(\frac{\phi}{f}\right)^6 + \dots \quad (3.4)$$

Only the free mass term (ϕ^2) is considered, while self interactions (ϕ^4) are ignored. Higher order terms are useless to considered, since $(\phi/f)^\alpha$ becomes extremely small starting from $\alpha = 6$. The expansion then stops at first order in ϕ

In this case

$$V(\phi) = \Lambda^4 \left(1 - \left(1 - \frac{1}{2} \frac{\phi^2}{f^2} \right) \right) = \frac{1}{2} \frac{\Lambda^4}{f^2} \phi^2 = \frac{1}{2} m^2 \phi^2. \quad (3.5)$$

With this potential, it is now possible to derive the Klein-Gordon equation for the scalar field ϕ

$$\square\phi = \frac{\partial V}{\partial\phi}. \quad (3.6)$$

From the metric given in eq[1.6], the matrix needed is

$$g_{\mu\nu} = \begin{pmatrix} -1 & 0 & 0 & 0 \\ 0 & a^2(t) & 0 & 0 \\ 0 & 0 & a^2(t) & 0 \\ 0 & 0 & 0 & a^2(t) \end{pmatrix}. \quad (3.7)$$

The determinant of this matrix is noted with the letter g . The next step is to compute the unperturbed d'Alembertian [104].

$$\square = \frac{1}{\sqrt{-g}} \partial_\mu (\sqrt{-g} g^{\mu\nu} \partial_\nu). \quad (3.8)$$

In this case, the easy form of $g_{\mu\nu}$ allows a direct computation

$$\begin{aligned}\square &= \frac{1}{\sqrt{-g}} \partial_\mu (\sqrt{-g} g^{\mu\nu} \partial_\nu) \\ &= \frac{1}{\sqrt{-g}} \partial_0 (\sqrt{-g} g^{00} \partial_0) + \frac{1}{\sqrt{-g}} \partial_i (\sqrt{-g} g^{ii} \partial_i) \\ &= \frac{1}{a^3} \partial_0 (-a^3 \partial_0) + \frac{1}{a^3} a^3 \frac{1}{a^2} \partial_i \partial_i \\ &= -3 \frac{a^2}{a^3} \dot{a} \partial_0 - \partial_0^2 + \frac{1}{a^2} \nabla^2 \\ &= -\partial_0^2 - 3H\partial_0 + \frac{\nabla^2}{a^2}.\end{aligned}\tag{3.9}$$

Using (3.9) into (3.6) leads to

$$-\ddot{\phi} - 3H\dot{\phi} + \frac{\nabla^2}{a^2} \phi = \partial_\phi V.\tag{3.10}$$

For the moment is valid the assumption that ϕ is homogeneous, so the ∇ term in the above equation vanishes. The conclusion is the Klein-Gordon equation that rules the motion of a free particle in a FLRW metric under the influence of a potential V .

$$\ddot{\phi} + 3H\dot{\phi} + \partial_\phi V = 0.\tag{3.11}$$

From this equation it is possible to conclude that DM scales as non-relativistic matter. To see this, and considering $H/m \ll 1$ the JWKB approximation is useful to solve equation of the form [104], [67]

$$\ddot{x} + 2\eta\dot{x} + k^2x = 0.\tag{3.12}$$

In this approximation $\dot{x}/x = -\eta$. The comparison between eq.3.12 and eq.3.11 gives $\dot{\phi}/\phi = -3H/2$. Since $H = \dot{a}/a$, this equation can be solved by separating the variables. It turns out

$$\ln \phi \propto -\frac{3}{2} \ln a \implies \phi \propto a^{-3/2}.\tag{3.13}$$

Inserting this scale into eq.1.26 and using the slowroll approximation eq.1.28, the conclusion is that $\rho \propto a^{-3}$ and this is exactly the behavior of non-relativistic matter.

3.4 Klein-Gordon perturbed

Of course, the Universe is full of matter that perturbs space-time. A metric like the one in eq.1.6 is not perfect to describe the reality of the Universe. The FLRW metric changes when perturbations are included and the Newtonian gauge can be used to describe it. The Newtonian potentials are referred with Φ and Ψ [104]

$$ds^2 = -(1 + 2\Phi)dt^2 + a^2(t)(1 - 2\Psi)\delta_{ij}dx^i dx^j,\tag{3.14}$$

where Φ and Ψ are the scalar gravitational potentials. In a Universe without anisotropic stresses it is possible to consider $\Phi = \Psi$ since there is a parameter called "gravitational slip" [133] $\eta = \Phi/\Psi$ which is the ratio between the effective gravitational coupling of light to that of the matter, and is almost equal to 1. A Universe without anisotropic stresses shows a stress energy tensor $T_{\mu\nu}$ where the three pressures are identical, so it is invariant under spatial rotations [52].

Having then $\Phi = \Psi$, the matrix is

$$g_{\mu\nu} = \begin{pmatrix} -(1 + 2\Phi) & 0 & 0 & 0 \\ 0 & a^2(t)(1 - 2\Phi) & 0 & 0 \\ 0 & 0 & a^2(t)(1 - 2\Phi) & 0 \\ 0 & 0 & 0 & a^2(t)(1 - 2\Phi) \end{pmatrix}.\tag{3.15}$$

The goal is again to compute (3.6), remembering that the d'Alembertian is given by (3.8)

This time the treatment is more complicated than in the unperturbed case, so some approximations are required. In particular, the main assumption is to consider Φ only at first order

$$\begin{aligned} g &= -a^6(1+2\Phi)(1-2\Phi)^3 \\ &= -a^6(1-4\Phi^2)(1-2\Phi)^2 \\ &= -a^6(1-4\Phi^2)(1-4\Phi+4\Phi^2) \\ &= -a^6(1-4\Phi+4\Phi^2-4\Phi^2+16\Phi^3-16\Phi^4). \end{aligned} \quad (3.16)$$

Considering only terms at first order in Φ , the determinant in (3.16) becomes

$$g = -a^6(1-4\Phi). \quad (3.17)$$

For the next step remember the expansion $(1+x)^\alpha \sim 1 + \alpha x$ for small x . This expansion is justified because the order of magnitude of Φ is 10^{-4} [52]

$$\sqrt{-g} = a^3(1-4\Phi)^{1/2} \sim a^3(1-2\Phi). \quad (3.18)$$

Before the computation of the d'Alembertian, the terms of $g^{\mu\nu}$ can also be expanded

$$g^{00} = -\frac{1}{1+2\Phi} \sim -1 + 2\Phi, \quad g^{ii} = \frac{1}{a^2(1-2\Phi)} \sim \frac{1+2\Phi}{a^2}. \quad (3.19)$$

The computation of the d'Alembertian will be divided into three parts

$$\begin{aligned} \square &= \frac{1}{\sqrt{-g}} \partial_\mu (\sqrt{-g} g^{\mu\nu} \partial_\nu) \\ &= \underbrace{\frac{1}{\sqrt{-g}} \partial_\mu (\sqrt{-g})}_{\mathcal{A}} g^{\mu\nu} \partial_\nu + \underbrace{\partial_\mu (g^{\mu\nu})}_{\mathcal{B}} \partial_\nu + \underbrace{g^{\mu\nu} \partial_\mu \partial_\nu}_{\mathcal{C}}. \end{aligned} \quad (3.20)$$

The first computation will be \mathcal{A}

$$\frac{1}{\sqrt{-g}} \partial_\mu (\sqrt{-g}) g^{\mu\nu} \partial_\nu = \frac{1}{\sqrt{-g}} \partial_0 (\sqrt{-g}) g^{00} \partial_0 + \frac{1}{\sqrt{-g}} \partial_i (\sqrt{-g}) g^{ii} \partial_i, \quad (3.21)$$

and since

$$\begin{aligned} \partial_0 \sqrt{-g} &= 3a^2 \dot{a}(1-2\Phi) - 2a^3 \dot{\Phi} \\ \partial_i \sqrt{-g} &= -2a^3 \partial_i \Phi, \end{aligned}$$

the first partial result is

$$\begin{aligned} \frac{1}{\sqrt{-g}} \partial_\mu (\sqrt{-g}) g^{\mu\nu} \partial_\nu &= \frac{-3a^2 \dot{a}(1-2\Phi)^2}{a^3(1-2\Phi)} \partial_0 + \frac{2a^3 \dot{\Phi}(1-2\Phi)}{a^3(1-2\Phi)} \partial_0 - \frac{2a^3 \partial_i \Phi}{a^3(1-2\Phi)} \frac{1}{a^2} (1+2\Phi) \partial_i \\ &= -(1-2\Phi) 3H \partial_0 + 2\dot{\Phi} \partial_0 - \frac{2}{a^2} \partial_i A \partial_i. \end{aligned} \quad (3.22)$$

For the last term it is been used the fact that $(1+2\Phi)/(1-2\Phi) \sim (1+2\Phi)^2$ and since only first order terms in Φ are considered [52], that ratio can be put similar to 1 since it will be multiply by $\partial_i \Phi$ that is already a first order term.

The \mathcal{B} term is

$$\begin{aligned} \partial_\mu g^{\mu\nu} \partial_\nu &= \partial_0 g^{00} \partial_0 = +\partial_i g^{ii} \partial_i \\ &= 2\dot{\Phi} \partial_0 + \frac{2}{a^2} \partial_i A \partial_i. \end{aligned} \quad (3.23)$$

The last one, \mathcal{C} , is the most immediate

$$\begin{aligned} g^{\mu\nu}\partial_\mu\partial_\nu &= g^{00}\partial_0^2 + g^{ii}\partial_i\partial_i \\ &= -(1 - 2\Phi)\partial_0^2 + \frac{1 + 2\Phi}{a^2}\nabla^2. \end{aligned} \quad (3.24)$$

Now the only thing to do is to sum (3.22), (3.23) and (3.24)

$$\square = -(1 - 2\Phi)3H\partial_0 + 2\dot{\Phi}\partial_0 - \frac{2}{a^2}\partial_i A\partial_i + 2\dot{\Phi}\partial_0 + \frac{2}{a^2}\partial_i A\partial_i - (1 - 2\Phi)\partial_0^2 + \frac{1 + 2\Phi}{a^2}\nabla^2.$$

And then

$$\square = -(1 - 2\Phi)(\partial_0^2 + 3H\partial_0) + a^{-2}(1 + 2\Phi)\nabla^2 + 4\dot{\Phi}\partial_0. \quad (3.25)$$

Rather than the whole ϕ it is more useful to work with a complex ψ and so the field can be defined in another way [104]

$$\phi(r, t) = \frac{1}{\sqrt{2}m} \left[\psi(r, t)e^{-imt} + \psi^*(r, t)e^{imt} \right], \quad (3.26)$$

where only the slow variating oscillations are considered and ψ varies slower than the exponential term [104]. The JWKB approximation works to solve linear differential equations with spatially variating coefficients. Since we are considering a field in slow roll, the condition is $|\ddot{\psi}| \ll m|\dot{\psi}|$. In other words the condition is $\partial_t \ll m$, and since for Schrodinger $\partial_t \sim \nabla^2/m \sim k^2/m$, it leads to $k^2/m \ll m$ [78]. The first term is the momentum term, while the latter is the rest mass. This means that the field is slowly variating.

Equation (3.6) with the potential expressed in (3.5) and the d'Alembertian in equation (3.25) becomes

$$-(1 - 2\Phi)(\partial_0^2 + 3H\partial_0)\phi + a^{-2}(1 + 2\Phi)\nabla^2\phi + 4\dot{\Phi}\partial_0\phi = m^2\phi. \quad (3.27)$$

In order to solve this equation, the first and second derivatives of ϕ are needed. Considering ϕ given in eq. 3.26 the first and second time derivative of the field are [104]

$$\begin{aligned} \partial_0\phi &= \frac{1}{\sqrt{2}m}\dot{\psi}e^{-imt} - \frac{i}{\sqrt{2}}\psi e^{-imt} \\ &= \left(\frac{1}{\sqrt{2}m}\dot{\psi} - \frac{i}{\sqrt{2}}\psi \right) e^{-imt}, \end{aligned} \quad (3.28)$$

$$\begin{aligned} \partial_0^2\phi &= \frac{1}{\sqrt{2}m}\ddot{\psi}e^{-imt} - \frac{i}{\sqrt{2}}\dot{\psi}e^{-imt} - \frac{i}{\sqrt{2}}\dot{\psi}e^{-imt} - \frac{m}{\sqrt{2}}\psi e^{-imt} \\ &= \left(i\sqrt{2}\dot{\phi} - \frac{m}{\sqrt{2}}\psi \right) e^{-imt}. \end{aligned} \quad (3.29)$$

These two results are obtained considering the assumption that ψ is slowly variating, adding the condition for slow roll ($\epsilon = -\dot{H}/H^2$), and applying the JWKB approximation. The assumptions implies that $\Phi \sim \epsilon^2, H/m \sim \epsilon$ and $\psi \sim \epsilon$ [78], and so some term that appear in (3.27) can be neglected since only quadratic term in ϵ are considered. For simplicity, the exponential term e^{-imt} is omitted and simplified later. Computing all the terms that appear in eq. 3.27 the single elements are

$$\begin{aligned}
-\partial_0^2 \phi &= i\sqrt{2}\dot{\psi} + \frac{m}{\sqrt{2}}\psi, \\
-3H\partial_0\phi &= -\frac{3H}{\sqrt{2}m}\dot{\psi} + \frac{3Hi}{\sqrt{2}}\psi, \\
2\Phi\partial_0^2\phi &= -2\Phi i\sqrt{2}\dot{\psi} - \sqrt{2}\Phi m\psi, \\
6\Phi H\partial_0\phi &= \frac{6\Phi H}{\sqrt{2}m}\dot{\psi} - \frac{6\Phi Hi}{\sqrt{2}}\psi, \\
\frac{1}{a^2}\nabla^2\phi &= \frac{1}{\sqrt{2}ma^2}\nabla^2\psi, \\
\frac{2\Phi}{a^2}\nabla^2\phi &= \frac{2\Phi}{\sqrt{2}ma^2}\nabla^2\psi, \\
4\dot{\Phi}\partial_0\phi &= \frac{4\dot{\Phi}}{\sqrt{2}m}\dot{\psi} - \frac{4\dot{\Phi}i}{\sqrt{2}}\psi, \\
m^2\phi &= \frac{m}{\sqrt{2}}\psi.
\end{aligned}$$

Now, inserting all these terms into eq. 3.27 and remembering that only the term quadratic in ϵ are involved, the result is

$$i\sqrt{2}\dot{\psi} + \frac{m}{\sqrt{2}}\psi + \frac{3Hi}{\sqrt{2}}\psi - \sqrt{2}\Phi m\psi + \frac{1}{\sqrt{2}ma^2}\nabla^2\psi = \frac{m}{\sqrt{2}}\psi. \quad (3.30)$$

Dividing by $\sqrt{2}$, the non-linear Shrödinger equation is then obtained. It is also called Gross-Pitaevskii equation [118, 76]

$$i\left[\dot{\psi} + \frac{3}{2}H\psi\right] + \frac{1}{2ma^2}\nabla^2\psi = \Phi m\psi. \quad (3.31)$$

It is confirmed the non-relativistic behavior for unperturbed background, since $\nabla^2\psi$ and Φ would be zero and equation 3.31 would be

$$\dot{\psi} + \frac{3}{2}H\psi = 0, \quad (3.32)$$

that is already been solved in equation 3.13.

3.5 From Klein-Gordon to fluid treatment

DM can be seen as a superfluid, which is a fluid without viscosity. In this way the motion of the fluid does not dissipate kinetic energy. Recalling equation eq. 3.31, it is possible to define the field ψ in the following way [173]

$$\psi(r, t) = \sqrt{\frac{\rho(r, t)}{m}} e^{i\theta(r, t)}. \quad (3.33)$$

So that $\rho(r, t) = m|\psi(r, t)|^2$. If short timescale are considered, than H tends to 0 since for small t it is true that $H = \dot{a}/a \rightarrow 0$ and the equation 3.31 become

$$i\dot{\psi} = -\frac{1}{2m}\nabla^2\psi + \Phi m\psi. \quad (3.34)$$

In this equation is formulated in physical coordinates, since $x_p = a \cdot x_c$ and so $\nabla_c = a \cdot \nabla_p$

The next step is to insert equation (3.33) into equation (3.34). The terms are computed separately

$$\begin{aligned} i\dot{\psi} &= \frac{i}{\sqrt{m}} \partial_0 \sqrt{\rho} e^{i\theta} - \sqrt{\frac{\rho}{m}} \partial_0 \theta e^{i\theta}, \\ \nabla \psi &= \frac{1}{\sqrt{m}} \nabla \sqrt{\rho} e^{i\theta} + i \sqrt{\frac{\rho}{m}} \nabla \theta e^{i\theta}, \\ \nabla^2 \psi &= \frac{1}{\sqrt{m}} \nabla^2 \sqrt{\rho} e^{i\theta} + \frac{i}{\sqrt{m}} \nabla \sqrt{\rho} \nabla \theta e^{i\theta} + \frac{i}{\sqrt{m}} \nabla \sqrt{\rho} \nabla \theta e^{i\theta} + \\ &\quad + i \sqrt{\frac{\rho}{m}} \nabla^2 \theta e^{i\theta} - \sqrt{\frac{\rho}{m}} (\nabla \theta)^2 e^{i\theta}. \end{aligned}$$

Inserting everything into eq. 3.34, terms $e^{i\theta}$ and $-\sqrt{\rho/m}$ can be simplified. Now the Schrödinger equation is split into its real and imaginary part [59].

The real part leads to

$$\frac{\partial \theta}{\partial t} = \frac{1}{2m} \frac{1}{\sqrt{\rho}} \nabla^2 \sqrt{\rho} - \frac{1}{2m} (\nabla \theta)^2 - \Phi m. \quad (3.35)$$

And the imaginary part equation is

$$\frac{\partial \sqrt{\rho}}{\partial t} = -\frac{1}{2m} (2 \nabla \sqrt{\rho} \nabla \theta + \sqrt{\rho} \nabla^2 \theta). \quad (3.36)$$

Instead of treating $\partial \sqrt{\rho}$ it is more useful to work with $\partial \rho$

$$\begin{aligned} \frac{1}{2} \rho^{-1/2} \frac{\partial \rho}{\partial t} &= -\frac{1}{2m} \left(2 \frac{1}{2} \rho^{-1/2} \nabla \rho \nabla \theta + \rho^{1/2} \nabla^2 \theta \right) \\ &= -\frac{\rho^{-1/2}}{2m} (\nabla \rho \nabla \theta + \rho \nabla^2 \theta). \end{aligned} \quad (3.37)$$

Now deleting $\rho^{-1/2}/2$, the result is then

$$\frac{\partial \rho}{\partial t} = -\frac{1}{m} (\nabla \rho \nabla \theta + \rho \nabla^2 \theta). \quad (3.38)$$

This final equation can be changed a little. If $A = \rho$ and $B = \nabla \theta$, in (3.38) it is possible to recognize the form $\nabla(AB) = \nabla A B + A \nabla B$

In the end

$$\frac{\partial \rho}{\partial t} = -\frac{1}{m} \nabla(\rho \nabla \theta). \quad (3.39)$$

3.6 Probability Current

Equation (3.39) can be written in a even more simpler form by considering the following computation. It is known that the probability density related to a field is given by [59]

$$P(r, t) = \psi^*(r, t) \psi(r, t), \quad (3.40)$$

and if in a position the probability to find a particle decreases, it means that it increases in another place for the conservation of the total probability. There is therefore a flow, or, in other words, a current. The goal is to relate the probability density to this current that is noted with J

Let be J_x the probability per unit time and unit area that passes through dA parallel to yz plane. Now it is possible to compute the rate of change in the probability density in a more general way without specifying the direction of J . Remember that the goal is to link P to J , so it can be written [59]

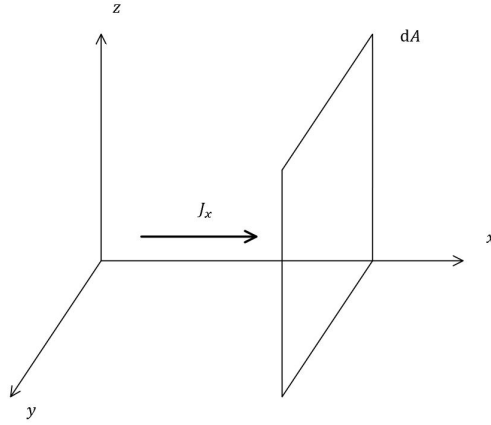


Figure 3.2: Geometrical representation of the x-component of the probability current through an infinitesimal area dA

$$\begin{aligned} \frac{\partial P}{\partial t} &= -\nabla \cdot \mathbf{J} \\ &= \frac{\partial \psi^*}{\partial t} \psi + \psi^* \frac{\partial \psi}{\partial t}. \end{aligned} \quad (3.41)$$

For the derivative of ψ and ψ^* , eq 3.34 is used in a slight different form

$$\dot{\psi} = -i \left[\frac{1}{2m} \left(\frac{\nabla}{i} \right) \left(\frac{\nabla}{i} \right) \psi + \Phi m \psi \right]. \quad (3.42)$$

So, in this way

$$\begin{aligned} \frac{\partial P}{\partial t} &= \psi^* \frac{\partial \psi}{\partial t} + \frac{\partial \psi^*}{\partial t} \psi \\ &= -i \left[\psi^* \frac{1}{2m} \left(\frac{\nabla}{i} \right) \left(\frac{\nabla}{i} \right) \psi + \Phi m \psi^* \psi - \psi \frac{1}{2m} \left(-\frac{\nabla}{i} \right) \left(-\frac{\nabla}{i} \right) \psi^* - \Phi m \psi \psi^* \right] \\ &= -i \left[\psi^* \frac{1}{2m} \left(\frac{\nabla}{i} \right) \left(\frac{\nabla}{i} \right) \psi - \psi \frac{1}{2m} \left(-\frac{\nabla}{i} \right) \left(-\frac{\nabla}{i} \right) \psi^* \right] \\ &= -\frac{1}{2mi} (\psi^* \nabla(\nabla \psi) - \psi \nabla(\nabla \psi^*)). \end{aligned} \quad (3.43)$$

The terms inside the parenthesis are in the form $A \nabla(\nabla B) = \nabla(A \nabla B) - \nabla A \nabla B$

$$\begin{aligned} (\psi^* \nabla(\nabla \psi) - \psi \nabla(\nabla \psi^*)) &= \nabla(\psi^* \nabla \psi) - \nabla \psi^* \nabla \psi - (\nabla(\psi \nabla \psi^*) - \nabla \psi \nabla \psi^*) \\ &= \nabla(\psi^* \nabla \psi - \psi \nabla \psi^*). \end{aligned}$$

Inserting it into equation 3.43

$$\frac{\partial P}{\partial t} = -\nabla \underbrace{\left(\frac{1}{2m} \psi^* \left(\frac{\nabla}{i} \right) \psi + \frac{1}{2m} \psi \left(-\frac{\nabla}{i} \right) \psi^* \right)}_{\mathbf{J}}. \quad (3.44)$$

In this way the form $\partial_t P = -\nabla \cdot \mathbf{J}$ was found. For completeness, inserting \hbar in order to have the correct units allows to highlight the momentum operator $-i\hbar \nabla$

$$\mathbf{J} = \frac{1}{2m} \psi^* \left(\frac{\hbar}{i} \nabla \right) \psi + \frac{1}{2m} \psi \left(-\frac{\hbar}{i} \nabla \right) \psi^* \quad (3.45)$$

$$= \frac{1}{2m} [\psi^* \hat{P} \psi + \psi \hat{P}^* \psi^*]. \quad (3.46)$$

The next step is to put equation (3.33) into (3.44)

$$\begin{aligned} \mathbf{J} &= \frac{1}{2m} \psi^* \frac{\nabla}{i} \psi - \frac{1}{2m} \psi \frac{\nabla}{i} \psi^* \\ &= \frac{1}{2m} \frac{(\sqrt{\rho})^2}{i} e^{-i\theta} i \nabla \theta e^{i\theta} - \frac{1}{2m} \frac{(\sqrt{\rho})^2}{i} e^{i\theta} (-i) \nabla \theta e^{-i\theta} \\ &= \frac{\rho}{m} \nabla \theta. \end{aligned} \quad (3.47)$$

It is known that the current density vector \mathbf{J} is the amount of charge per unit time that flows through a unit area perpendicular to the direction of motion $\mathbf{J} = d\mathbf{I}/dA$ [59]

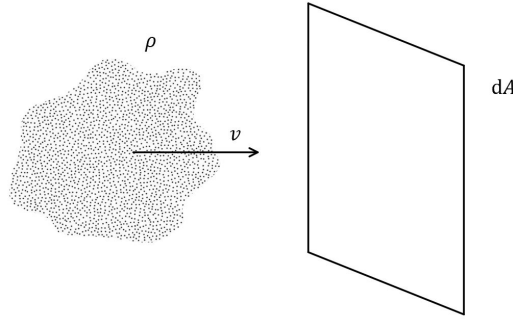


Figure 3.3: Simple representation of the motion of a group of charges with density ρ and velocity v through an area dA . The flow of the charges generate a current

Consider \mathbf{v} the velocity of the charge at time t perpendicular to dA . During dt , the charges that will go through dA will be the ones contained in the volume formed by dA and I

$$I = \frac{dq}{dt} = \frac{\rho dV}{dt} = \frac{\rho v dt dA}{dt} = \rho v dA,$$

and so

$$\mathbf{J} = \frac{d\mathbf{I}}{dA} = \frac{\rho \mathbf{v} dA}{dA} = \rho \mathbf{v}. \quad (3.48)$$

By equating eq. 3.47 and 3.48 an advantageous relation is then obtained

$$\begin{aligned} \rho \mathbf{v} &= \frac{\rho}{m} \nabla \theta \\ \mathbf{v} &= \frac{1}{m} \nabla \theta. \end{aligned} \quad (3.49)$$

3.7 Madelung equations

Eq. 3.49 is a fundamental relation, since it simplifies eq. 3.39

$$\frac{\partial \rho}{\partial t} = -\frac{1}{m} \nabla (\rho \nabla \theta) = -\nabla (\rho \mathbf{v}). \quad (3.50)$$

And also eq. 3.35

$$\begin{aligned}\frac{\partial\theta}{\partial t} &= \frac{1}{2m} \frac{1}{\sqrt{\rho}} \nabla^2 \sqrt{\rho} - \frac{1}{2m} (\nabla\theta)^2 - \Phi m \\ &= \frac{1}{2m} \frac{1}{\sqrt{\rho}} \nabla^2 \sqrt{\rho} - \frac{m}{2} v^2 - \Phi m.\end{aligned}\quad (3.51)$$

The eq. 3.50 and 3.51 are known as Madelung equations [102]. It is possible to identify θ as the velocity potential (possible thanks to eq. 3.49) and this can be seen as an equation of motion for an electrically charged fluid, but with is a strange term that involve $\nabla^2 \sqrt{\rho}$

$$\frac{\partial\theta}{\partial t} = \underbrace{-\frac{1}{2}mv^2}_{K} - \underbrace{\Phi m}_{P} + \underbrace{\frac{1}{2m} \frac{1}{\sqrt{\rho}} \nabla^2 \sqrt{\rho}}_{Q}.$$

K is the kinetic term, P is the potential term and Q is known as the quantum mechanical energy [115]. Rewriting the last equation by taking the gradient of eq. 3.51 and dividing by m , the result is the more familiar Euler equation [104]

$$\frac{1}{m} \nabla \frac{\partial\theta}{\partial t} = -\frac{1}{2} \nabla v^2 - \nabla \Phi + \frac{1}{2m^2} \nabla \left(\frac{1}{\sqrt{\rho}} \nabla^2 \sqrt{\rho} \right). \quad (3.52)$$

In the left-hand side it is possible to switch the derivatives and apply eq. 3.49 to obtain $\partial_t \mathbf{v}$. Noting that $\nabla(A \cdot B) = (A \cdot \nabla)B + (B \cdot \nabla)A + A \times (\nabla \times B) + B \times (\nabla \times A)$, the kinetic term ∇v^2 can be also changed. It can be seen that, $\nabla \times \mathbf{v} \propto \nabla \times \nabla\theta = 0$ since the rotor of the gradient is zero

$$\nabla(v^2) = \nabla(\mathbf{v} \cdot \mathbf{v}) = 2(\mathbf{v} \cdot \nabla)\mathbf{v}.$$

So eq. 3.52 became the quantum Euler equation, which is the usual Euler equation with the extra term given by the quantum potential [78]

$$\frac{\partial \mathbf{v}}{\partial t} + (\mathbf{v} \cdot \nabla) \mathbf{v} = -\nabla \Phi + \frac{1}{2m^2} \nabla \left(\frac{1}{\sqrt{\rho}} \nabla^2 \sqrt{\rho} \right). \quad (3.53)$$

3.8 Jeans scale

Suppose the density fluctuation is [78]

$$\rho(\mathbf{x}, a) = \bar{\rho}(a)[1 + \delta(\mathbf{x}, a)], \quad |\delta| \ll 1. \quad (3.54)$$

Consider eq. 3.53 and pick the two terms on the right-hand side. The computation to do is to compare them to verify when gravity dominates and when quantum pressure does. Taking the divergence

$$\nabla^2 \Phi = \frac{1}{2m^2} \nabla^2 \left(\underbrace{\frac{1}{\sqrt{\rho}} \nabla^2 \sqrt{\rho}}_{\nabla^2 \ln \sqrt{\rho}} \right).$$

So

$$\nabla^2 \Phi = \frac{1}{4m^2} \nabla^4 \ln \rho.$$

It is known that the Newtonian potential obey to $\nabla^2 \Phi = 4\pi G\rho$ and inserting eq. 3.54 instead of ρ

$$\begin{aligned}
4\pi G\bar{\rho} + 4\pi G\delta\bar{\rho} &= \frac{1}{4m^2}\nabla^4 \ln(\bar{\rho}(1+\delta)) \\
&= \frac{1}{4m^2}\nabla^4(\ln\bar{\rho} + \ln(1+\delta)) \\
&= \frac{1}{4m^2}\nabla^4\ln\bar{\rho} + \frac{1}{4m^2}\nabla^4\ln(1+\delta).
\end{aligned}$$

Consider only first order perturbation terms in which $\ln(1+\delta) \sim \delta$. The result is [76]

$$4\pi G\delta\bar{\rho} = \frac{1}{4m^2}\nabla^4\delta. \quad (3.55)$$

It is important to work in the Fourier space, where $\nabla \rightarrow i\mathbf{k}$

$$4\pi G\delta\bar{\rho} = \frac{1}{4m^2}k^4\delta. \quad (3.56)$$

Finally, the Jeans scale is found [79]

$$k_J = (16\pi G\bar{\rho})^{1/4}m^{1/2}. \quad (3.57)$$

From eq. [3.57], it is immediate to see that if k is larger than the Jeans scale quantum pressure dominates. In the opposite regime, on course, gravity dominates.

Having the Jeans scale, it is immediate compute the Jeans length

$$\lambda_J = \frac{2\pi}{k_J} = \pi^{3/4}G^{-1/4}\bar{\rho}^{-1/4}m^{-1/2}. \quad (3.58)$$

Introducing $m_{22} = m/10^{-22}$ eV and the background density $\rho_b \sim 2.8 \cdot 10^{11} \Omega_m h^2 M_\odot \text{Mpc}^{-3}$, the Jeans length can be parameterize in the following way [76]

$$\lambda_J = 55 m_{22}^{-1/2} \left(\frac{\bar{\rho}}{\rho_b} \right)^{-1/4} (\Omega_m h^2)^{-1/4} \text{kpc}. \quad (3.59)$$

Eq [3.57] is the physical Jeans scale, so the comoving one is simply $a \cdot k_J$. Since the Jeans scale depend on the mean density and the behavior of $\bar{\rho}$ is known from eq [1.12], it is possible to find the value of the Jeans scale at the equivalence radiation-matter

$$k_{eq} = 9m_{22}^{1/2} \text{Mpc}^{-1}. \quad (3.60)$$

Given the relation $k - \lambda$, large k means that small scales are considered. When $k > k_J$ quantum pressure dominates, so this could explain why small-scales structure are less numerous than what the model predicts. Gravity is not sufficient to win the force exercised by the quantum pressure and this prevents the accretion of ordinary matter in the potential well of the halo and, consequently, the formation of the galaxy itself.

To see this small-scale effect of FDM, the power spectrum is the most powerful tool. The power spectrum analysis perform a fast Fourier Transform to the variation of a specific input signal and the result is a frequency spectrum. The power spectrum then shows the magnitude of the frequency components. Given the power spectrum of ordinary Λ CDM cold DM $P_{CDM}(k)$, the power spectrum of FDM is [76]

$$P_{FDM}(k) = T_F^2(k)P_{CDM}(k), \quad (3.61)$$

where

$$T_F(k) = \frac{\cos x(k)^3}{1+x(k)^8}, \quad (3.62)$$

is the transfer function and $x(k) = 1.61 m_{22}^{1/18} k/k_{eq}$.

The scale at which the power spectrum of FDM is reduced by a factor 2 is noted as $k_{1/2}$ and after that, the power spectrum shows a dramatic drop [78]

$$k_{1/2} = \frac{1}{2} k_{eq} m_{22}^{-1/18} \sim 4.5 m_{22}^{4/9} \text{ Mpc}^{-1}. \quad (3.63)$$

For k below this critical value, the structures in the FDM scenario behave like the ones foreseen in the standard Λ CDM model. This can be seen in the simulation plotted in Fig.3.4 while the differences in the small scale structure can be understood by looking at the plot of the power spectrum in Fig.3.5.

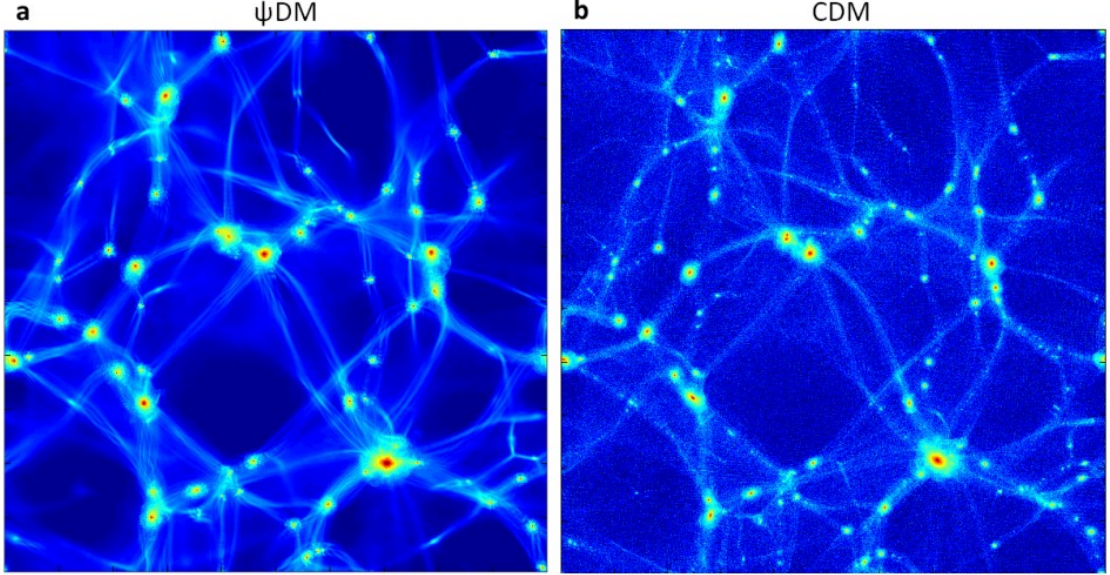


Figure 3.4: (Left) large scale structures formed considering Wave DM (ψ DM) where it is clearly observable the pattern of filaments and void that is also detectable in the conventional collisionless CDM model (Right). For the two simulations have been considered the same cosmological parameters. It is clear that the CDM simulation has way more small scale structure that are suppressed in the ψ DM case (Figure from [146]).

The cut-off in the power spectrum at small scales could solve the Core-Cusp Problem and the Missing Satellite Problem. However, this explanation could lead to other issues. Just to mention two of them [76]

- If the cut-off at small scales is indeed a fact, it is also true that the first stars formed in object of mass $\sim 10^5 M_\odot$ according to the Λ CDM scenario, are now forced to be born in structure of masses $> 10^8 M_\odot$ due to the destruction of small scales halos. As a consequence, reionization would be delayed and the number of luminous galaxies before that event would be heavily reduced;
- The cut-off is in the linear power spectrum, but quantum effects in the non-linear power spectrum of DM could reduce its relevance.

3.9 The Axiverse

The QCD axion is just one realization of a wide range of these ultralight scalar fields. In particular, string theory involves pseudoscalars fields with axion properties with a mass range that span over 23 orders of magnitude, starting from 10^{-33} eV up to 10^{-10} eV [8].

In this "Axiverse", the mass of the axion determine if its contribution goes into the DM or DE sector. More specifically, it is found that if the mass of the axion $m_a \leq 10^{-32}$ eV, the field become indistinguishable from DE since its energy density does not behave anymore as a non-relativistic particle $\phi \propto a^{-3/2}$.

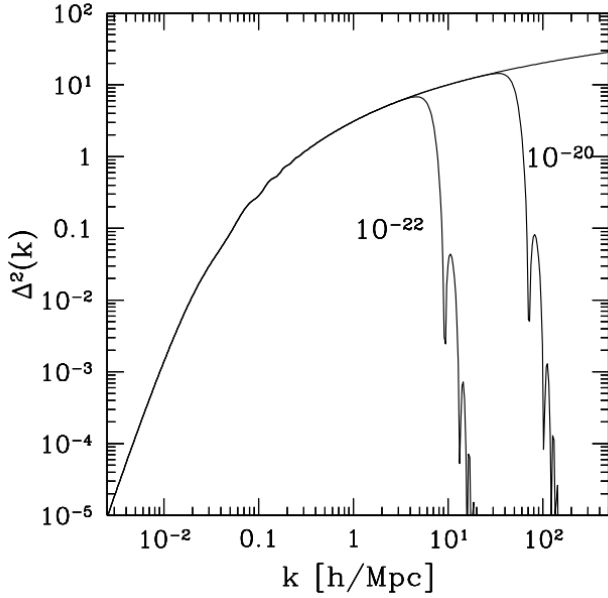


Figure 3.5: The plot shows the dimensionless power spectrum $\Delta(k)^2 = 4\pi k^3 P(k)/(2\pi)^3$ versus the wavenumber. The upper line is the spectrum of conventional CDM and, at high value of k , the different behavior of FDM considering two masses for the ultralight scalar field: 10^{-22}eV and 10^{-20}eV . At low k , so at large scale, the spectra follow the same trend. However, at small scales, FDM shows a cut-off due to the presence of the quantum pressure that in principle could explain the problems of CDM (Figure from [78]).

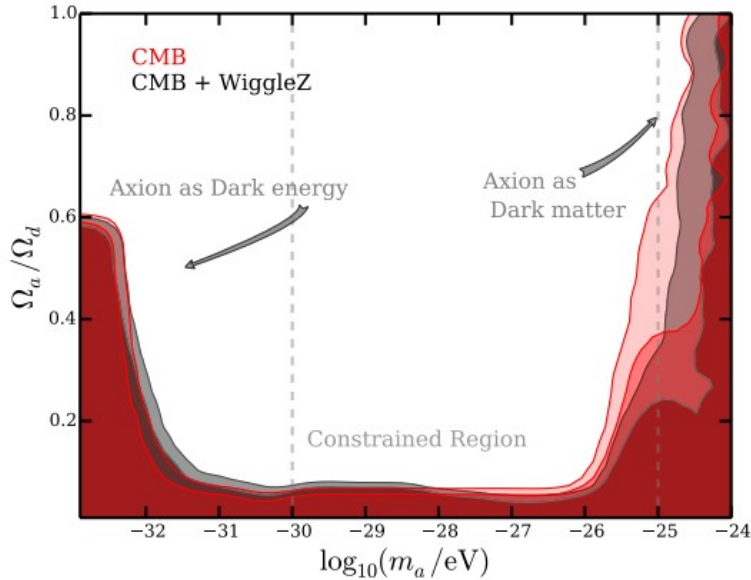


Figure 3.6: The plot shows the marginalized 2σ and 3σ contour of the contribution of axion with different masses to DM and DE. The y-axis represent the density parameter of axion relative to the total DM density. The data used come from the constraints obtained from CMB and WiggleZ DE survey [121] data on LSS. For masses $m_a > 10^{-27}\text{eV}$ the axion dilute as a non relativistic particle and therefore contribute to DM. For lower masses, the axion contribute to DE. In between those bounds, there is a region where the contribution is extremely low (Figure from [73]).

Currently, thanks to recent studies on the axion mass spectrum and on small-scale structure formation [141], [110] it is believed that FDM model with a unique ultralight axion with a mass of $\sim 10^{-22} - 10^{-21}$ eV could solve the small scale crisis. However, it is also possible that axion represent only one of the contributions to DM, DE or both.

Cosmological parameters predicted by the standard Λ CDM would show some discrepancy if one consider CMB anisotropies measurement in Planck experiments and other cosmological probes at small redshift. This tension is characterized by the parameter S_8 and it could be alleviate by a coupling between DE and DM [116] [142]

$$S_8 = \sqrt{\frac{\Omega_m}{0.3}} \sigma_8, \quad \sigma_8 = \frac{1}{2\pi^2} \int dk W_s^2 k^2 P(k), \quad (3.64)$$

where σ_8 is the linear matter fluctuation i.e. the root mean square of the density perturbation on scales $8h^{-1}\text{Mpc}$ at $z = 0$. Ω_m is the matter density parameter and W_s the tophat filter function in Fourier space given by

$$W_s = \frac{3j_1(kR_8)}{kR_8}, \quad (3.65)$$

in which j_1 is the first order spherical Bessel function $j_1(x) = \frac{\sin x}{x^2} - \frac{\cos x}{x}$ and R_8 the radius $8h^{-1}\text{Mpc}$.

For large values of k (small scales) the tophat filter function goes to zero and this cause a cut-off in σ_8 . As it is shown in Fig 3.7 the cut-off in the linear matter power spectrum is dependent on the mass of the axion.

Considering that axion mass cover a vast range, it is possible to give an estimate about the percentage of the DM density that the axion represents according to its mass value. To study this new type of DE-DM, it is used a data set obtained by a joint analysis of Planck CMB and full-shape galaxy power spectrum and bispectrum data from BOSS, a survey part of the third phase of the Sloan Digital Sky Survey [48]. For BOSS data a non-linear order theory will be necessary

3.9.1 Planck CMB data

For the model, the only perturbation considered are adiabatic (also called curvature perturbations). For this reason, a perturbation in ϕ is expressible with a shift in time in the background scalar field $\delta\phi = \dot{\phi}(t)\delta t(t, \mathbf{x})$ where \mathbf{x} is the position-vector [66].

The considered CMB data are the temperature TT, cross TE, polarisation EE and lensing potential $\phi\phi$ power spectra C_l as a function of the multipole l [135].

We recall that a deviation from the average property, as the temperature for example, can be defined by $\Theta(\hat{\mathbf{n}}) = (T(\hat{\mathbf{n}}) - \langle T \rangle)/\langle T \rangle$ with $\hat{\mathbf{n}} \equiv (\theta, \phi)$ a specific direction. This deviation can also be expressed by

$$\Theta(\hat{\mathbf{n}}) = \sum_{l>2} \sum_{|m|<l} a_{lm} Y_{lm}(\hat{\mathbf{n}}), \quad (3.66)$$

in which Y_{lm} are the standard spherical harmonics and a_{lm} constant coefficients given by

$$a_{lm} = \int_{\theta=-\pi}^{\theta=\pi} \int_{\phi=0}^{\phi=2\pi} \Theta(\hat{\mathbf{n}}) Y_{lm}^*(\hat{\mathbf{n}}) d\Omega. \quad (3.67)$$

The angular frequency l gives the angular scale of oscillations ($\theta \sim \pi/l$). The power spectrum of the fluctuation is then defined by

$$\langle a_{lm} a_{l'm'}^* \rangle = \delta_{ll'} \delta_{mm'} C_l. \quad (3.68)$$

The average is taken over many ensembles in our Universe, so the delta functions are justified by isotropy. Since the possible values of m are $(2l + 1)$ for each l , the power spectrum can be expressed by

$$C_l = \frac{1}{2l+1} \sum_{|m|<l} \langle |a_{lm}|^2 \rangle. \quad (3.69)$$

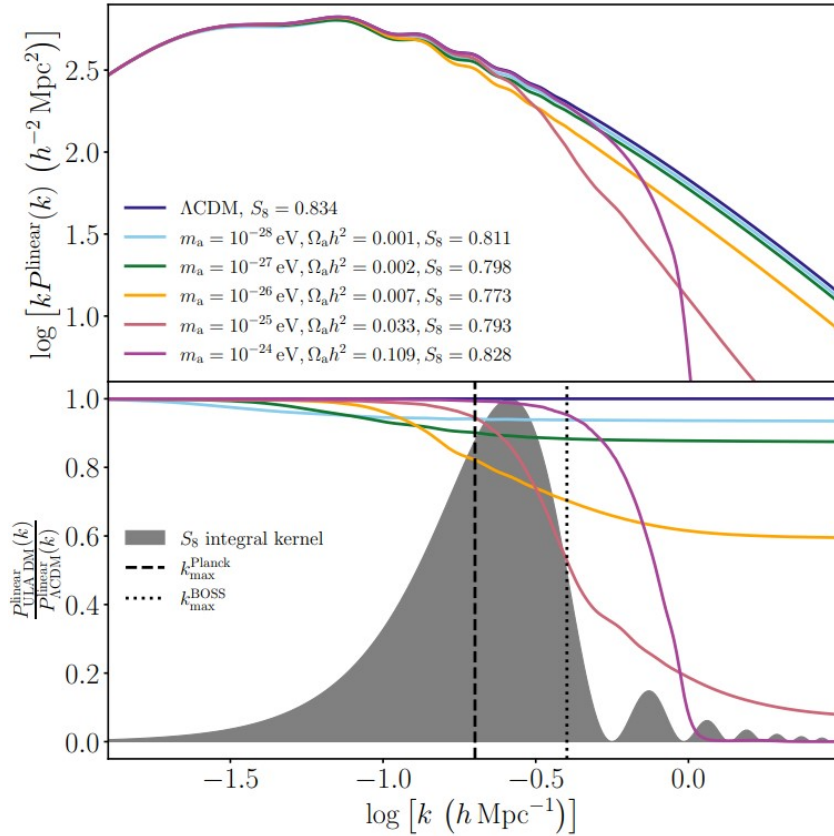


Figure 3.7: In the top panel shows the dependency of the linear matter power spectrum on the axion mass and so on the relative density parameter and S_8 tension. The power spectra are taken considering both Planck and BOSS data (Baryon Oscillatory Spectroscopy Survey [48]). The grey shaded area in the bottom panel tells the sensitivity of the S_8 tension to wavenumber and the vertical lines are the maximum value of k considering the results given by CMB measurements [135] and the BOSS galaxy power spectrum. If the ultralight field has a mass $> 10^{-24} \text{ eV}$ the cut-off will be no more effective for attenuate the S_8 tension. On the other hand, if $m_a < 10^{-25} \text{ eV}$, the axion suppression power become lower and lower. A lower bound of $m_a \sim 10^{-28}$ can be established since for lower masses, the constraints of data would be too strong in order to have an appreciable effect on the tension (Figure from [142]).

The C_l spectra and their changes according to the axion mass, can be found in Fig.3.8. In order to obtain those posteriors, the following likelihood have been considered [161] [160]:

- For low multipoles ($2 \leq l \leq 29$) it has been used the TT likelihood `commander_dx12_v3_2_29` and the EE likelihood `simall_100x143_offlike5_EE_Aplanck_B`;
- For high TT multipoles ($30 \leq l \leq 2508$) and TE,EE multipoles ($30 \leq l \leq 1996$) the likelihood is given by `plik_lite_v22_TTTEEE`;
- For what concern the lensing spectrum there is a unique likelihood for the multipoles ($8 \leq l \leq 400$) given by `smicadx12_Dec5_ft1_mv2_ndlcpp_p_teb_context8`.

For the analysis of Planck data, it is sufficient the linear theory of perturbations, since higher order effects are relevant for multipoles not considered in the analysis [14].

3.9.2 BOSS galaxy spectrum and bispectrum data

The BOSS survey contain the full-shape galaxy spectrum and bispectrum data [132]. If the spatial distribution of galaxies is plotted as a function of redshift and distances, it is possible to see that the redshift plot is distorted due to peculiar velocities of galaxies that adds to the standard expansion effect [87].

The model of the redshift-space galaxy power spectrum used needs one-loop perturbation theory. According to the effective field theory of large-scale structure (EFT of LSS), the power spectrum is the sum of several contribution [142] [81]

$$P_l(k, z) = \underbrace{P_l^{tree}(k, z)}_1 + \underbrace{P_l^{1-loop}(k, z)}_2 + \underbrace{P_l^{noise}(k, z)}_3 + \underbrace{P_l^{ctr}(k, z)}_4. \quad (3.70)$$

1. This term take into account tree-level perturbations, so linear bias and redshift-space distortion. This is the lowest order in perturbation theory
2. The second term is related to non-linear redshift-space mapping, non-linearities due to DM clustering and bias up to 1-loop in order
3. Stochastic contribution modelled with the Poisson shot noise. It has constant power spectrum in Fourier space and free amplitude
4. This last term represents the ultraviolet counterterms whose purpose is to treat small-scale physics that cannot be modeled with perturbation theory. Indeed, part of the loop integral involves high values of k Fourier modes where perturbation theory is not effective

The multipoles are computed from the full anisotropic galaxy power spectrum $P_g(k, \mu, z)$ with μ the cosine of the angle between k and the line-of-sight [142]

$$P_l(k, z) = \frac{2l+1}{2} \int_{-1}^1 d\mu \mathcal{L}_l(\mu) P_g(k, \mu, z), \quad (3.71)$$

with $\mathcal{L}_l(\mu)$ a Legendre polynomial.

When dealing with non-linear treatment, another very useful statistical implement is the bispectrum, the Fourier counterpart of the three-point correlation function and the lowest order perturbation tool to probe non-Gaussianity [155].

Likewise with the spectrum, the bispectrum can be divided into its contributions

$$B(\mathbf{k}_1, \mathbf{k}_2, z) = B^{tree}(\mathbf{k}_1, \mathbf{k}_2, z) + B^{ctr}(\mathbf{k}_1, \mathbf{k}_2, z) + B^{noise}(\mathbf{k}_1, \mathbf{k}_2, z), \quad (3.72)$$

where each term is linked to quantities in analogy with eq.3.70

To understand the phenomenology of axions, it is necessary to modify the background evolution, the linear power spectrum and using those changes in the EFT of LSS. After having marginalized over a full set of nuisance parameters [142] [80] and used a public BOSS likelihood [117], the galaxy power spectrum and bispectrum are obtained and plotted in Fig.3.9 and Fig.3.10

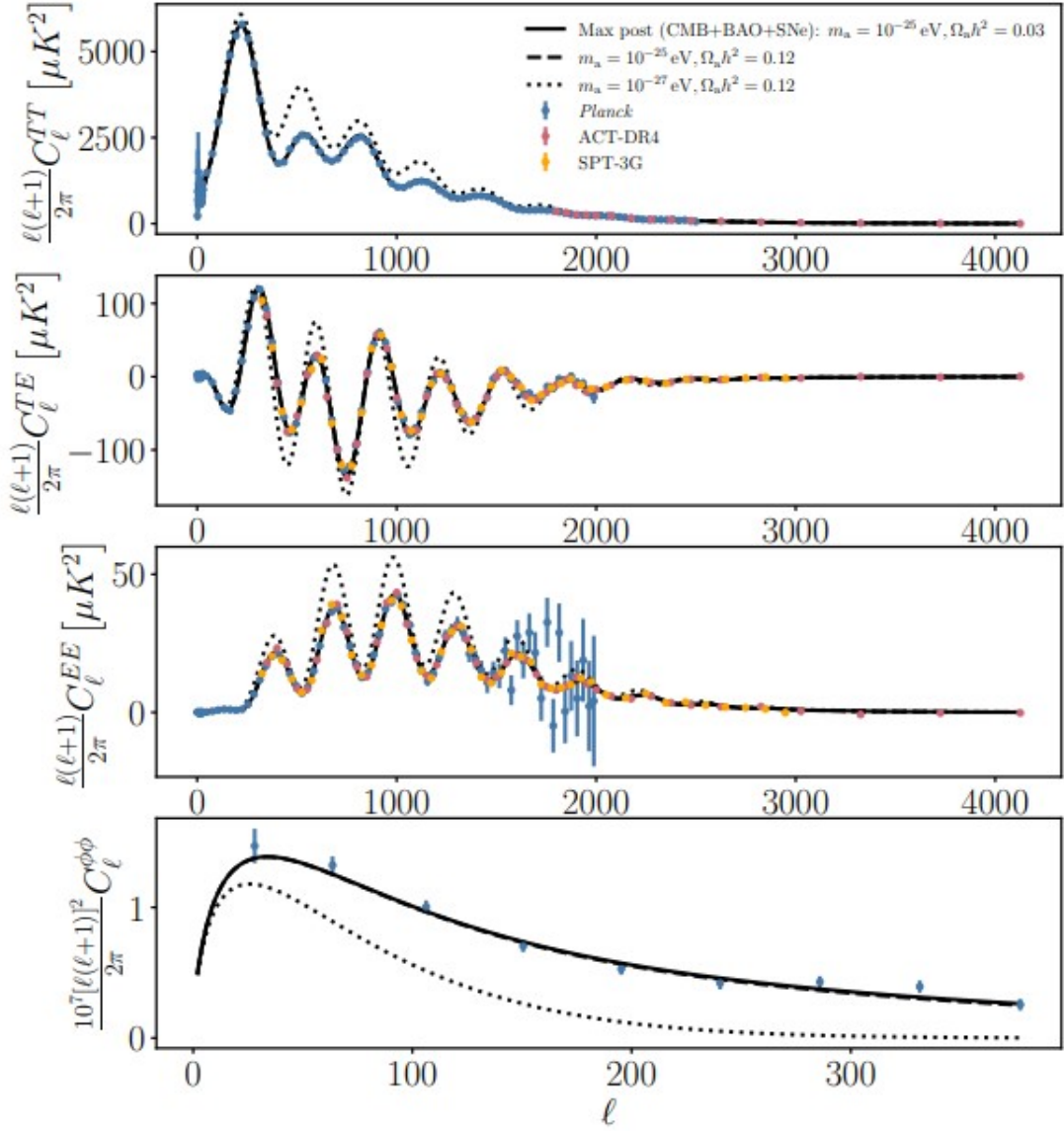


Figure 3.8: From top to bottom: the TT,TE,EE and $\phi\phi$ power spectrum as a function of the ℓ . The dots comes from the observation of Planck (blue dots, [135]), Atacama Cosmology Telescope Data Release 4 (ACT-DR4, red dots, [2]) and South Pole Telescope third survey (SPT-3G, orange dots, [151]). The maximum posterior computed takes into account also data from galaxy baryon acoustic oscillation [24], [143], [4] and supernovae data [22] for an axion mass of 10^{-25} eV and a parameter density of $\Omega_a h^2 = 0.03$. It can be also see how the power spectra changes when other type of cosmological model are considered (Figure from [142]).

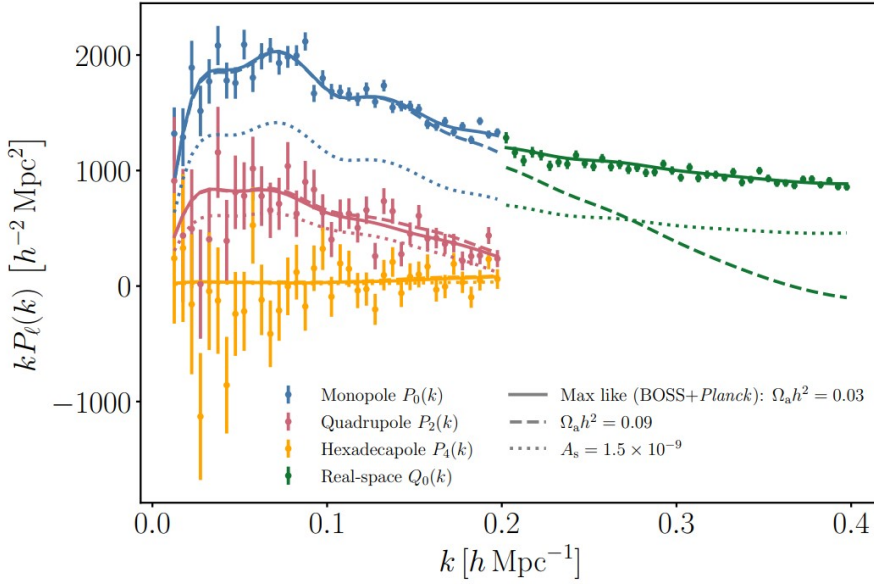


Figure 3.9: The solid lines of different colors show the maximum likelihood obtained by with BOSS spectrum together with CMB data. The dashed lines represents the same, but highlighting the effect of the presence of axion with mass $m_a = 10^{-25}$ that shows a suppression factor at small-scales, especially in the real-space power spectrum, and a little enhancement in the quadrupole power spectrum. The dotted lines are the results given by BOSS by itself considering a specific value of the amplitude of the primordial power spectrum perturbation, lower than the value given by the joint analysis ($A_s = 2.15 \cdot 10^{-9}$). In different colors, the monopole (blue), quadrupole (pink), hexadecapole (yellow) and the reshift distortion-free real space $Q_0(k, z) = P_0(k, z) - P_2(k, z)/2 + 3P_4(k, z)/8$ (Figure from [142]).

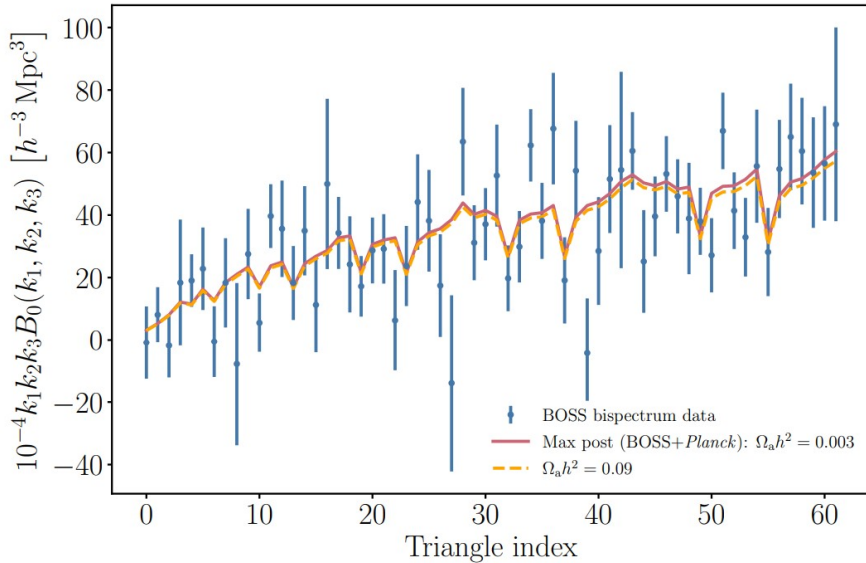


Figure 3.10: BOSS galaxy bispectrum monopole $B_=(k_1, k_2, k_3)$ maximum posterior. The solid and dashed lines differ only for the effect of the presence of axions of mass $m_a = 10^{-25}$ eV that leads to $\Omega_a h^2 = 0.09$. In the x -axis there is the triangle index which is a parameter that increase firstly with k_1 , then with k_2 and finally with k_3 . The only slight differences are for high values of the k_i parameters (Figure from [142]).

3.9.3 Constraints on the axion population

All cosmological parameters are obtained by plugging all the likelihoods presented into the estimation code `Cosmosis` [174] and the posterior distributions are obtained with `MultiNest` [58]. In Fig.3.11 there are the results of BOSS and Planck alone and then of the joint analysis [142].

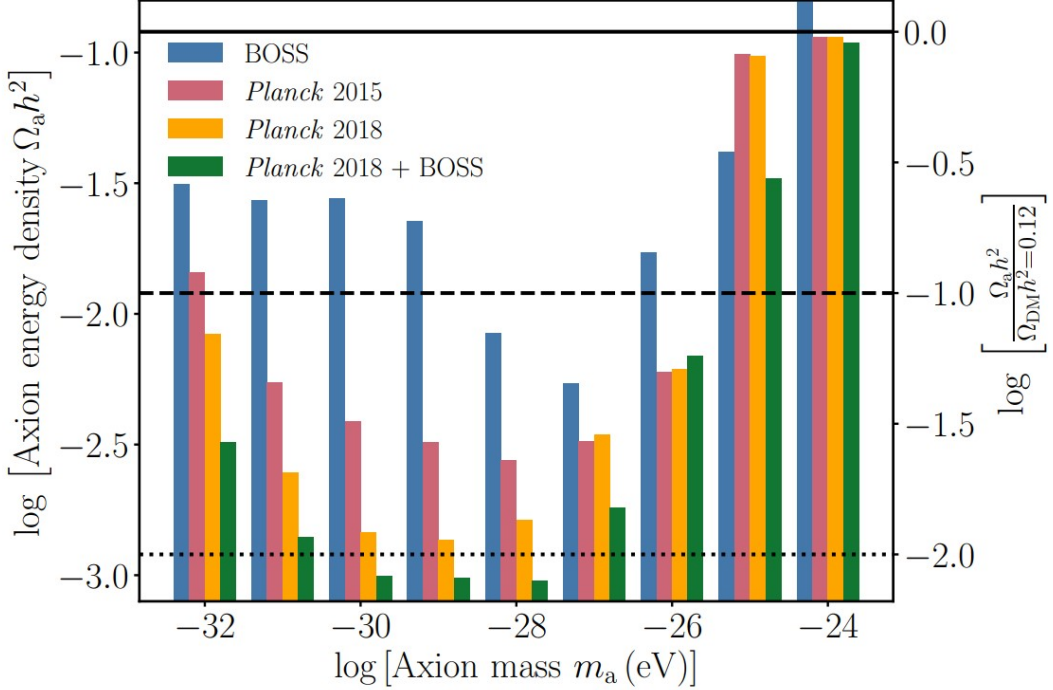


Figure 3.11: (Left scale) 95% C.L. upper limit to the axion energy density at different axion masses considering different datasets in different colors. (Right scale) 95% C.L. upper limit to the ratio between the axion energy density and the current DM energy density. The horizontal lines represent the threshold at which the axion energy density reach the 1% (dotted line), 10% (dashed line) and 100% (solid line) of the current amount of DM. The joint analysis put the most severe constraints of both DM and DE like axions (Figure from [142]).

Planck (both 2018 [135] and 2015 [119] data release) shows a "U" shape in the constraints. The major contributions of axion energy density come from DE-like axions ($m_a < 10^{-30}$ eV) and DM-like axion ($m_a > 10^{-27}$ eV). While the two Planck datasets are consistent for $m_a > 10^{-27}$ eV, at lower masses they show particular different values due to the fact that 2018 data involves also low- l multipoles. As one can see in Table 2 of Rogers et al (2023) [142] and here reported here in Table 3.1, when DM-like axions represent a significant percentage of the total amount of DM, the suppression power below the Jeans scale could attenuate the S_8 tension and this happens for 10^{-27} eV $< m_a < 10^{-25}$ eV. In particular, for $m = 10^{-26}$ eV, the tension is $S_8 = 0.819 \pm 0.020$ with respect to the $S_8 = 0.843^{+0.014}_{-0.013}$ computed in the Λ CDM model [142].

BOSS results maintain the "U" shape but there is a clear enhancement on the estimates axion energy density at all masses with respect to Planck data, with the exception of $m_a = 10^{-25}$ eV. The average tension value is lower than the Planck case and the lowest value is $S_8 = 0.653 \pm 0.040$ when $m_a = 10^{-26}$ eV. Also for the BOSS data, it is reported here the results summarized in Table 6 of Rogers et al (2023) [142], here in Table 3.2

Using both Planck and BOSS datasets, we can obtain the strongest limits on our parameters. Basically, BOSS data addition lower the axion energy density obtained by Plank at every axion mass, maintained again the "U" shape. The lowest value of the tension is again at $m_a = 10^{-26}$ eV and it is $S_8 = 0.804^{+0.020}_{-0.024}$ [142].

The most important results of the joint analysis are that axions cannot be more than the 10% of the current total DM for $m_a < 10^{-26}$ eV and it cannot either be more than 1% for

m_a	$\Omega_a h^2$ (<i>Planck</i>)	S_8 (<i>Planck</i>)	$\Omega_a h^2$ (<i>Planck+BOSS</i>)	S_8 (<i>Planck+BOSS</i>)
Λ CDM	–	$0.834^{+0.014}_{-0.013}$	–	0.827 ± 0.011
10^{-24} eV	< 0.11399	0.831 ± 0.014	< 0.10858	$0.826^{+0.011}_{-0.012}$
10^{-25} eV	< 0.09667	$0.811^{+0.025}_{-0.039}$	< 0.03306	$0.818^{+0.015}_{-0.017}$
10^{-26} eV	< 0.00615	0.819 ± 0.020	< 0.00689	$0.804^{+0.020}_{-0.024}$
10^{-27} eV	< 0.00344	$0.822^{+0.016}_{-0.020}$	< 0.00181	$0.819^{+0.013}_{-0.014}$
10^{-28} eV	< 0.00163	$0.831^{+0.014}_{-0.012}$	< 0.00095	0.824 ± 0.011
10^{-29} eV	< 0.00136	0.836 ± 0.014	< 0.00097	0.826 ± 0.011
10^{-30} eV	< 0.00145	$0.837^{+0.014}_{-0.013}$	< 0.00099	0.827 ± 0.011
10^{-31} eV	< 0.00247	$0.838^{+0.015}_{-0.014}$	< 0.00140	0.827 ± 0.011
10^{-32} eV	< 0.00833	$0.843^{+0.019}_{-0.016}$	< 0.00321	$0.829^{+0.012}_{-0.011}$

Table 3.1: Results of the joint analysis of Rogers et. al (2023) on the constraints on axion energy density and the matter clumping factor as a function of m_a considering only CMB data and then a joint dataset (Table from [142]).

m_a	$\Omega_a h^2$ (BOSS)	S_8 (BOSS)
Λ CDM	–	$0.723^{+0.041}_{-0.037}$
10^{-24} eV	< 0.15539	$0.718^{+0.038}_{-0.039}$
10^{-25} eV	< 0.04174	$0.709^{+0.043}_{-0.037}$
10^{-26} eV	< 0.01717	0.653 ± 0.040
10^{-27} eV	< 0.00542	$0.719^{+0.040}_{-0.038}$
10^{-28} eV	< 0.00842	$0.742^{+0.050}_{-0.040}$
10^{-29} eV	< 0.02259	$0.759^{+0.044}_{-0.043}$
10^{-30} eV	< 0.02771	$0.745^{+0.041}_{-0.040}$
10^{-31} eV	< 0.02706	$0.744^{+0.040}_{-0.042}$
10^{-32} eV	< 0.03126	$0.737^{+0.040}_{-0.038}$

Table 3.2: Results of the joint analysis of Rogers et. al (2023) on the constraints on axion energy density and the matter clumping factor as a function of m_a considering only BOSS data (Table from [142]).

$10^{-30}\text{eV} < m_a < 10^{-28}\text{eV}$. In addition, the scale-dependent suppression of axion (see top plot of Fig.3.7) can alleviate the S_8 tension by bringing closer the results of CMB to the ones coming from more direct probes at smaller-scale structure in galaxy clustering [142].

3.10 Generation of the first stars

Stars can be classified into three different population group

- **PopI:** this category is made up by young, metal-rich stars. Being metal-rich, their material has been processed several time by stars that have lived in former times;
- **PopII:** stars of this population have a lower, but not null metallicity and an older age than the PopI objects;
- **PopIII:** this is a hypothetical population of stars and involves the first stellar objects formed in the Universe. For this reason, they are the oldest and metal-free stars ever existed.

FDM, being a proposed modification of CDM, shows different behavior due to its wave nature and this reflects into a different history in the formation of the first stellar objects. By studying the formation of the PopIII stars, constrains on the mass of the ultralight scalar field can be imposed.

3.10.1 The simulation

Using the software **MUSIC** (Multi-Scale Initial Condition, [69]) FDM density and velocity field are generated considering a redshift $z = 100$ [94]. With those elements, it is possible to compute both the real and imaginary part of the wavefunction ψ using eq.3.49 and eq.3.33. The cosmological parameter used in MUSIC are the one given by the Plank Collaboration [135]

- Hubble constant $H_0 = 67.36 \text{ km/s/Mpc}$;
- Matter density parameter $\Omega_m = 0.315$;
- Baryon density parameter $\Omega_b = 0.0493$;
- Scalar spectral index $n_s = 0.9649$.

The wavefunction is then elaborated with another code, **ENZO** [35], which uses adaptive mesh refinement (AMR), a method to increase both high temporal and spatial accuracy for modeling astrophysical fluid flows. In particular, the interest goes into increase the resolution in turbulent regions. ENZO uses the wavefunction obtained thanks to MUSIC to solve the Gross-Pitaevskii equation [3.31]. The following results are obtained considering the mass of the ultralight boson equal to $m_B = 2.5 \cdot 10^{-22}\text{eV}$ and a volume given by the size $1.7 h^{-1}\text{Mpc}$. To ensure that such a small box contain enough collapsed structures, the simulation were set up to intentionally create an overdense region [94].

The simulation used time steps obtained by considering three sub-steps [97] and uses the code **SPoS**, a second order Schrödinger-Poisson solver built in as a module of ENZO [94, 97]. Eq.3.31 can be rewritten as

$$\partial_t \tilde{\psi} = (K + V)\tilde{\psi}, \quad (3.73)$$

where $\tilde{\psi} = a^{3/2}\psi$ is the normalized wave function, $K = i\nabla^2/ma^2$ is the kinetic operator in comoving coordinates and $V = -im\Phi$ the potential operator

The generic solution of the above equation is found by separating variables and leads to

$$\begin{aligned} \tilde{\psi}(t + \Delta t) &= e^{(K+V)\Delta t} \tilde{\psi}(t) \\ &= \underbrace{e^{V\Delta t/2}}_1 \underbrace{e^{K\Delta t}}_2 \underbrace{e^{V\Delta t/2}}_3 \tilde{\psi}(t) + \mathcal{O}(\Delta t^3). \end{aligned} \quad (3.74)$$

1. $\tilde{\psi}$ is evolved with the gravitational potential

$$\tilde{\psi} \longrightarrow e^{V\Delta t/2}\tilde{\psi} = e^{-im\Phi\Delta t/2}\tilde{\psi}. \quad (3.75)$$

2. The kinetic operator is applied through a 4th-order Runge-Kutta method, a numerical iterative method to solve non-linear equations

$$\tilde{\psi} \longrightarrow \tilde{\psi} + \frac{i}{ma^2} \nabla^2 \tilde{\psi} \Delta t. \quad (3.76)$$

3. Another gravitational evolution as in sub-step 1

This separation means that the total evolution of $\tilde{\psi}$ given by both gravitational and kinetic is separated into the single progresses. Considering the kinetic part only $\partial_t \tilde{\psi} = K \tilde{\psi}$ it assumes the form of a parabolic partial differential equation. This "kinetic" timestep is given by the Courant–Friedrichs–Lowy condition (CFL) [107], [46]. Having $\tilde{\psi}_t = \gamma \tilde{\psi}_{xx}$ and $\gamma = i\kappa$ with $\kappa \in \mathbb{R}$, the condition is

$$\frac{\kappa \Delta t}{\Delta x^2} < \frac{1}{6}, \quad (3.77)$$

at second order in time and fourth order in space. This means that the condition is truncated at $\mathcal{O}(\Delta t^2 + \Delta x^4)$ as $\Delta t, \Delta x \rightarrow 0$. So the condition of time is

$$\Delta t < \frac{1}{6\kappa} \Delta x^2 = \frac{ma^2}{6} \Delta x^2. \quad (3.78)$$

For the gravitational term $\partial_t \tilde{\psi} = V \tilde{\psi}$, it is sufficient to request that the phase is smaller than unity in order to $\tilde{\psi}$ to be slow variating

$$m\Phi \frac{\Delta t}{2} < 1 \longrightarrow \Delta t < \frac{2}{m\Phi}. \quad (3.79)$$

Considering now the whole equation $\partial_t \tilde{\psi} = (K + V)\tilde{\psi}$, the timestep condition is given by the combination of the two conditions above

$$\Delta t < \min \left[\frac{ma^2}{6} \Delta x^2, \frac{2}{m\Phi} \right]. \quad (3.80)$$

Back to the simulation, it has been add an AMR for the gas evolution in a region of size $0.119 h^{-1} \text{Mpc}$ comoving at $z = 13$ centered in the densest region of the box. Before $z = 13$ the evolution is almost linear, so the AMR is applied to look with more accuracy the evolution in the region of interest when the evolution starts to be peculiar [94].

3.10.2 Results on PopIII stars formation

Conventional CDM is supposed to form a spheroidal halo around stars in formation. However, in FDM scenario the first protostars are immersed in large structures collapsed only in one dimension called Zel'dovich pancake or sheets [94].

As the FDM collapse into the two dimensional sheet, it develop interference fringes. This are observable in the simulation plotted in the left panel of Fig. 3.12 and in different scales also in Fig. 3.13.

A first difference between FDM and CDM can already been highlighted. CDM would form several collapsed objects rather then a pancake structure. Indeed, the more massive is the DM particle, the more the structure will departed from a pancake to become an halo. A simulation made by Gao et al. [63] used WDM with a mass of $m = 3 \text{ keV}$ instead of standard CDM to reproduce the formation of large scale structures. The results are plotted in Fig. 3.14.

In the same simulation, it is also possible to find the distribution of DM particles around the axis of the filament and this is plotted here in Fig. 3.15

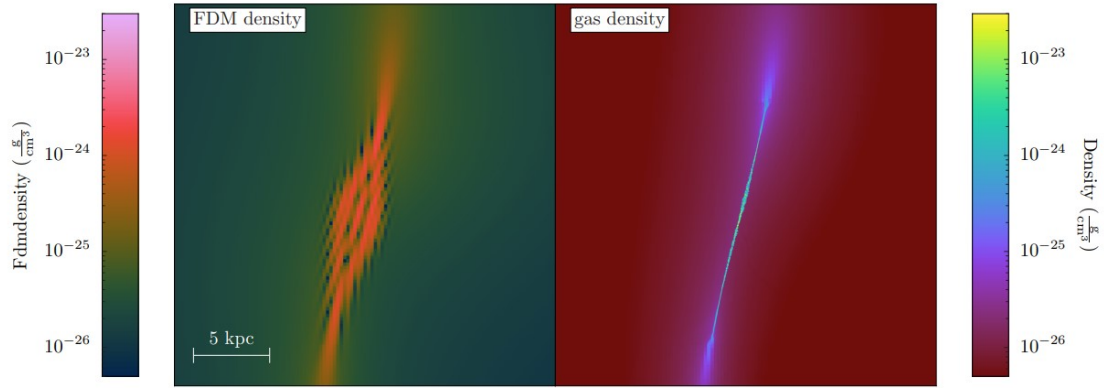


Figure 3.12: Density of DM (left) and of the gas (right) at $z = 10.03$ seen from a section that pass through the pancake. The DM sheet extends for $\sim 20 \text{ kpc}$ with a thickness of $\sim 2 \text{ kpc}$. The gas collapses in a smaller structure than the DM, with a thickness of $\sim 200 \text{ pc}$ (Figure from [94]).

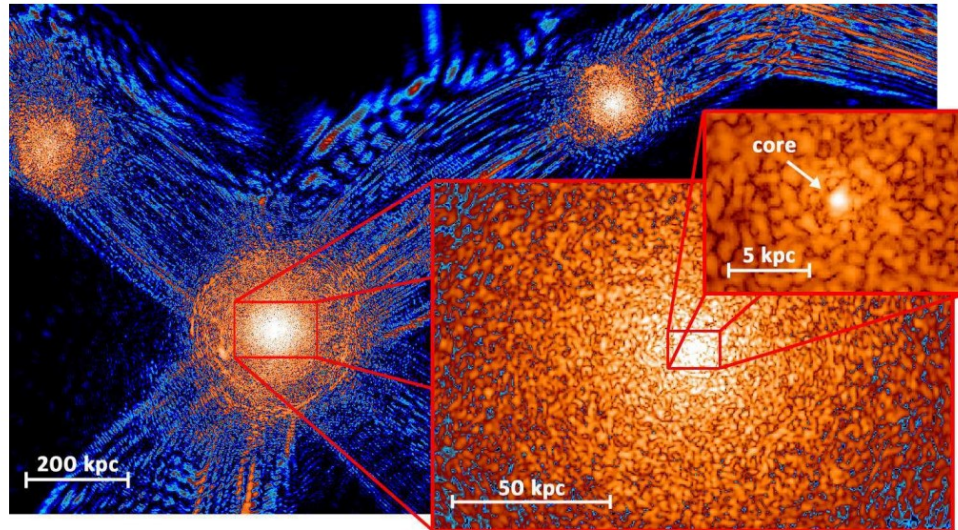


Figure 3.13: Simulated density field of FDM at different scale at redshift $z = 0.1$. As the scale become smaller, it can be see more clearly the wave nature of FDM thanks to the interference patterns (Figure from [146]).

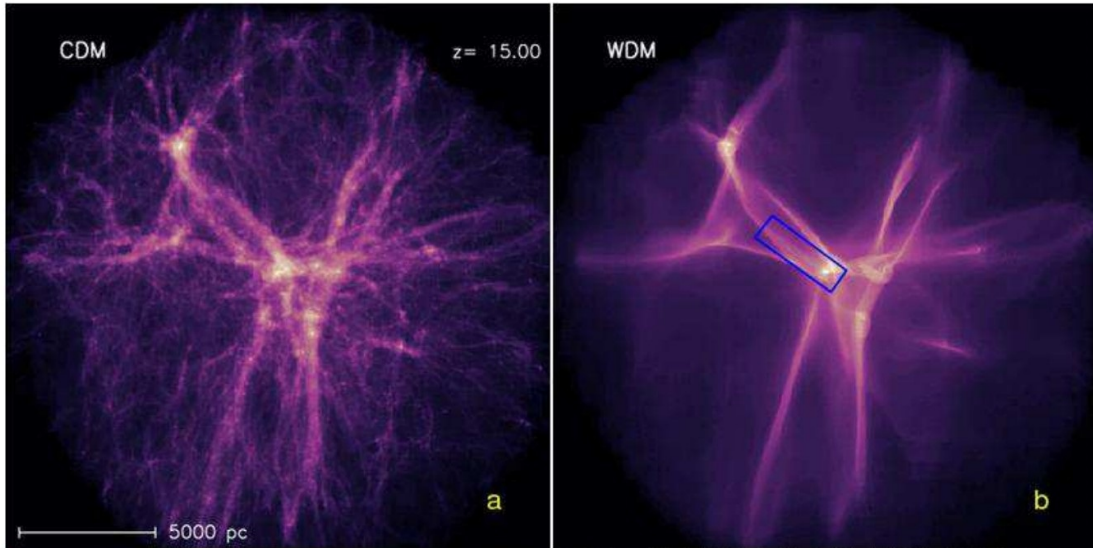


Figure 3.14: Comparison between the large scale structures formed at redshift $z = 15.00$. The structures follow the same pattern in both cases. However, the WDM scenario is more defined, in the sense that outside the filaments, there is the absence of the multitude of nearly spherical halos (Figure from [63]).

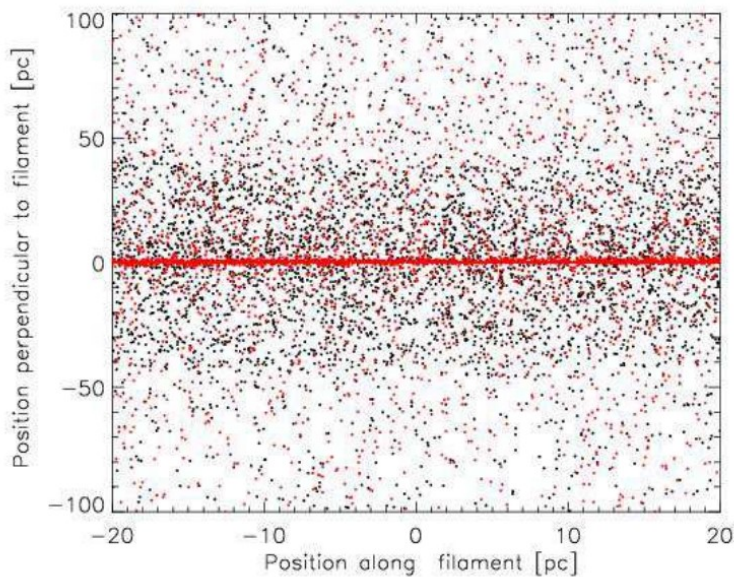


Figure 3.15: The back dots are DM particles of mass $m = 3 \text{ keV}$, while the red ones are representative for the gas. The filament pattern is suggested by the absence of a wide perpendicular spread with respect to the axis, and this show a difference with FDM, which forms two dimensional sheets (Figure from [63]).

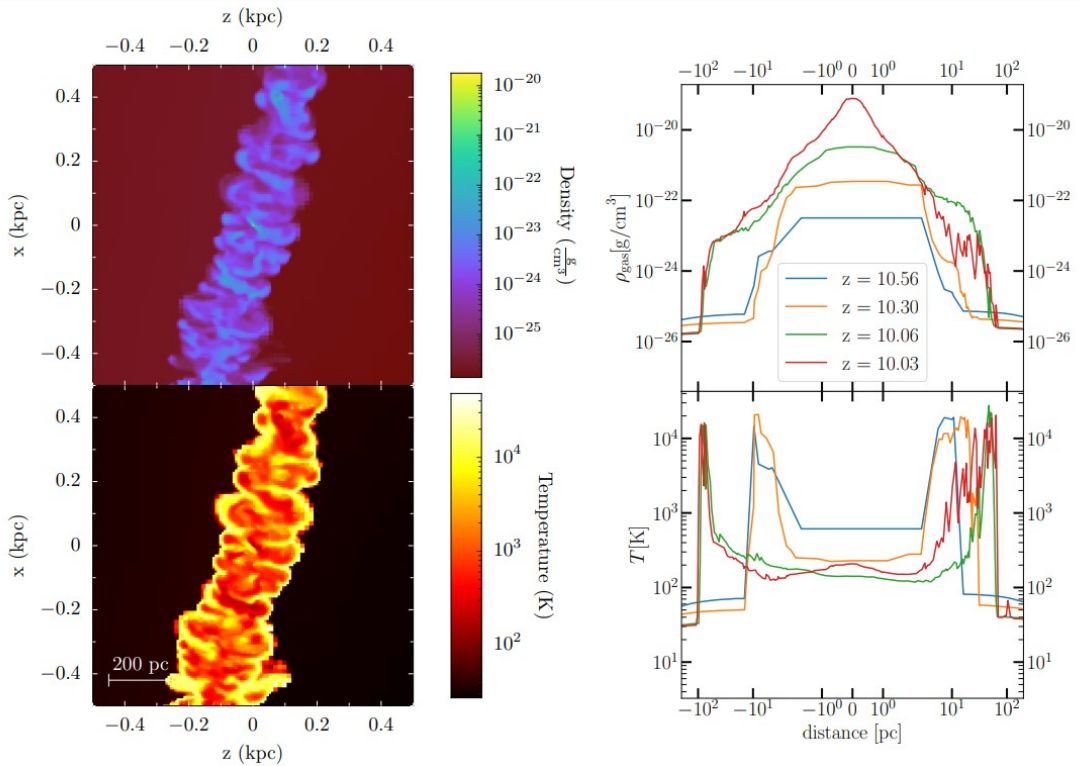


Figure 3.16: Density (above) and temperature (below) profile trough a section of the midplane of the pancake at redshift $z = 10.03$. The density increases towards the center as expected, however, the temperature is much higher at the edge of the sheet ($\sim 10^4 - 10^5 \text{ K}$) due to the shocks induced by the continuous infalling gas giving rise to a "M" temperature profile (Figure from [94]).

It seems like the masses of the order of 10^{-22} eV like in the case of FDM forms pancake structure with gas that condensate according to Fig.3.12. The density and temperature of the gas sheet are plotted in Fig.3.16.

The star formation is focused on the equatorial plane, where the gas is cooler and denser. The number density evolution plotted in Fig.3.16 is consistent with the behavior of the PopIII star forming gas clump in standard CDM cosmology [1], [106].

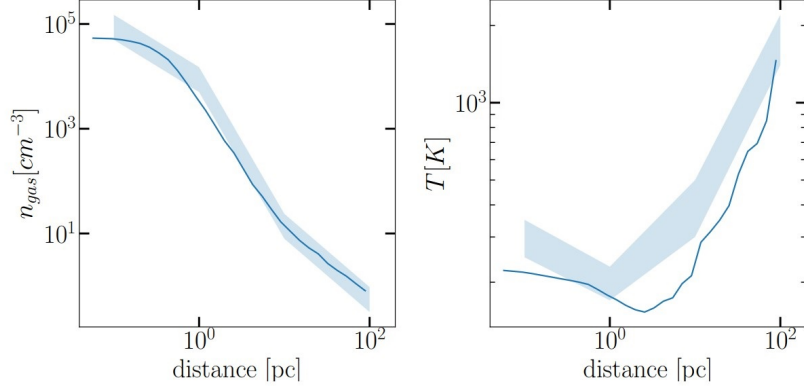


Figure 3.17: The solid line represent the temperature and density profiles in the sheet obtained by Kulkarni et al. (2022) considering FDM [94], while the shaded area in the profiles is the result of the studies of McGreer et al. (2008) on 4 different clumps with H_2 cooling in Λ CDM halos. From this fact, it seems that first stars have similar behavior in both cases, despite the huge differences in the DM models (Figure from [94]).

In the gas sheet there are, of course, more than one clump that will form a PopIII star. A natural question is how many clumps will undergo the same formation history in a sheet of the considered dimensions. Consider the geometrical configuration for the sheet in Fig.3.18.

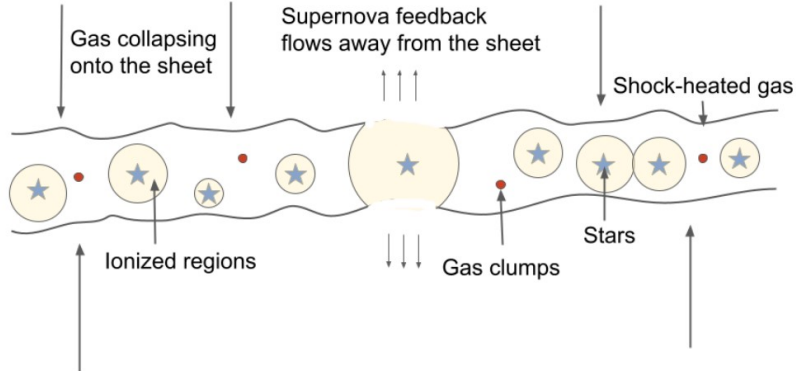


Figure 3.18: The sheet of gas is an extremely complicated environment. The central protostellar region is not the only location of star formation, but all along the sheet there are dense clumps that can collapse if some condition are fulfilled. Every clump that collapse into a star will form a bubble around itself defining a region where other clumps cannot create other stars due to perturbations (Figure from [94]).

The simulation performed by Kulkarni et al. (2022) [94] stopped at redshift $z = 10.03$ in correspondence of the central and densest clump collapse. However, it is reasonable to assume that other clumps will undergo the same fate of the central one. The question is which ones will

collapse and which ones won't. It is possible to use a simplified model to obtain an estimate of the number of PopIII star formed at the end of the collapse phase considering that object formed in a early times disturb the possible formation of future star in sheet regions within their zone of radiative influence.

Introducing a free length parameter l ^[94], a clump is considered such if its distance from all the clumps denser than itself is at least l . If this condition is not respected, it will be considered as a part of the denser clump at distance $< l$. As easily understandable, the more l is large, the less clumps will be considered as PopIII star formation region. Setting l to be 5, 10, 15 and 30 pc, the number of total clumps start to converge at ~ 50000 when $l = 15$ at the time of the central collapse that end the simulation.

As already mention, the stars formed emit ionizing radiation that perturb the surrounding region, denying any possibility to form other stellar objects. To see how many clumps will give birth to a PopIII star, the following assumption have been made [94].

- All the clumps number density evolve like the central densest one;
- When the star is formed, it emits radiation creating an ionizing bubble that keeps growing as long as the star lives at a constant velocity of ~ 30 km/s. Upon the death of the star, the size of this ionizing bubble remains constant;
- A clump inside an ionizing region will not collapsed to form another PopIII star;
- Clumps structure in the sheet does not change for about 50 Myrs. It is considered a dynamical timescale of ~ 120 Myrs using an average density;
- When radiation and other kind of feedback reach the edge of the pancake, they escape away due to the difference in the gas pressure.

It is possible to track the evolution of the population in the sheet considering all the above condition, and this is plot in Fig 3.19. The number of PopIII stars as a function of time is instead plotted in Fig 3.20. In this last plot three typical masses are considered and thanks to Schaefer [145] it is also known the lifetime of the star with the masses considered. In particular, the lifetime of stars of masses of 10, 80 and 300 M_\odot are respectively ~ 10 , 3 and 2 Myr.

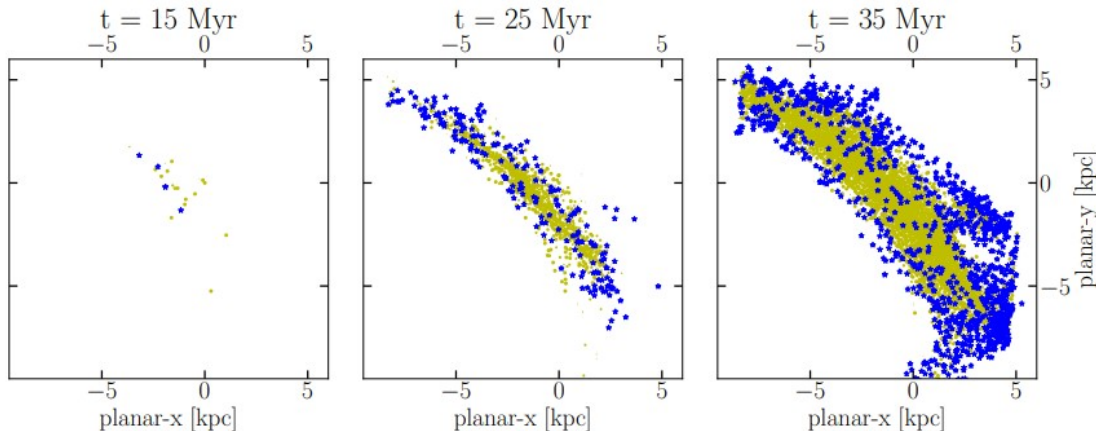


Figure 3.19: The three plots shows the population of newborn stars ($t_{life} < 1$ Myr, blue dots) and HII regions (green dots) assuming an average stellar mass of $80 M_\odot$. This type of evolution suggest that the central region is the first to be ionized, and therefore HII regions do not collapse anymore, while the stellar formation proceed in more distant regions as time passes (Figure from [94]).

The final results of the simulation is that a galaxy of PopIII is expected to have a total stellar mass of $\sim 10^5 M_\odot$ for about 20 Myr assuming a typical stellar mass of $80 M_\odot$. This means the the expected total number of star would be $\sim 10^4$. This kind of galaxy should be detectable at redshift

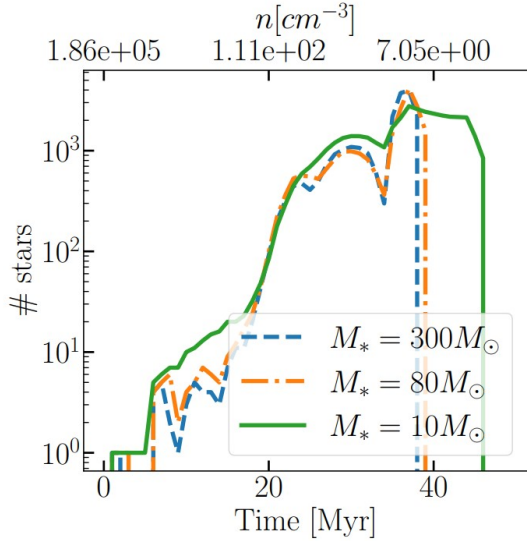


Figure 3.20: Considering three different average stellar masses, the plot shows the number of object as a function of time (Figure from [94]).

6 with the James Webb Space Telescope giving us a formidable tool supporting the FDM model over the CDM one. Moreover, a galaxy with such a relative small mass would not be present in the CDM scenario, since it would take 1-2 orders of magnitude more to form.

3.11 The Fornax dSph galaxy

It has been already stressed the fact that the NFW profile in eq.[2.32] is not the most accurate density profile to describe the soliton (or boson star) i.e. the bound object formed when the gravitational and quantum pressure terms in eq.[3.31] balance. This can be verified again by looking at Fig[3.21]. The soliton does not have an analytic density profile, but it is obtained numerically. First, the soliton mass is given by [146]

$$M_c = \frac{5.5 \cdot 10^9}{(m_b/10^{-23}\text{eV})^2(r_c/\text{kpc})} M_\odot, \quad (3.81)$$

and in the region $0 < r < 3r_c$ where the 95% of the soliton mass is contained, the density profile is

$$\rho_s(r) \sim \frac{1.9(m_b/10^{-23}\text{eV})^{-2}(r_c/\text{kpc})^{-4}}{[1 + 9.1 \cdot 10^{-2}(r/r_c)]^8} M_\odot/\text{pc}^3. \quad (3.82)$$

The best fit is obtained setting $M_c = 9.1 \cdot 10^7 M_\odot$, $r_c = 0.92\text{kpc}$ and $m_B = 8.1 \cdot 10^{-23}\text{eV}$.

In Fig[3.21] there is also a green dotted line, which represent an empirical fit obtained by Burkert [38]. The empirical formula is a slightly different form the NFW profile in eq.[2.32]

$$\rho_{DM}(r) = \frac{\rho_0 r_0^3}{(r + r_0)(r^2 + r_0^2)}, \quad (3.83)$$

where ρ_0 is the central density and r_0 a scale radius that can be identified with the soliton core radius. If it is supposed spherical symmetry, these two quantities are linked by the relation $\rho_0 = 4.5 \cdot 10^{-2}(r_0/\text{kpc})^{-2/3} M_\odot/\text{pc}^{-3}$

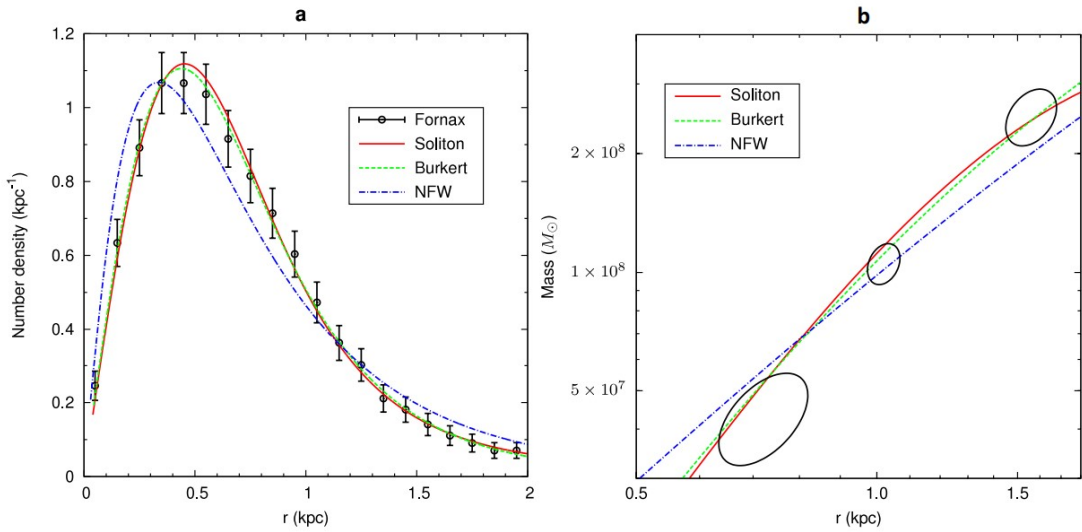


Figure 3.21: (Left) The number density as a function of the radius considering the subpopulation IM. The green dotted line is the result of the empirical fit, the blue dashed line the NFW profile, while the red line is the outcome considering wave DM. It is clear that the ψ DM scenario describe with more accuracy the real observation. (Right) Mass at different distances from the core. The circles are the 1σ contour of the total mass of the three subpopulation: from left to right the contour represent the subpopulation metal-poor (MP), intermediate-metallicity (IM) and metal-rich (MR). Again, wave DM is consistent with the observations (Figure from [146]).

Chapter 4

The Superradiance

Particles like the axion are a very good candidate as FDM, however they have never been observed in experiments therefore only estimates and hypothesis on the mass are possible. One way to put some constraints on the mass of ultralight scalar bosonic fields is to study the evolution of Kerr black holes.

The BH is needed to be spinning, since besides mass and angular momentum accretion onto the BH itself, it is possible also to extract them thanks to superradiance. In general, superradiance is an effect in dissipative systems that enhances radiation. This phenomenon related to BHs is been studied the first time by Zel'dovich and Misner in 1971 [172]. Schwarzschild BH are stable to superradiance because every perturbation that the compact object could suffer, dies exponentially [139].

With superradiance of BHs, it is possible to use gravitational waves to verify the eventual presence of scalar clouds in the surrounding of the BH. Those regions could emit monochromatic GWs with a frequency dependent on the mass of the axion $f \propto \mu$, where μ is the mass of the field. Moreover, if a massive boson is indeed present, its existence should be immediate to see in the Regge plane, which plot the mass of the BH against its dimensionless spin a_* , determining the existing regions of Kerr BHs experiencing superradiance [16], [153].

This chapter is meant to be an insight into one of the effects axions might have on detectable signals like gravitational waves, however the following discussion will not be detailed or rigorous.

4.1 Kerr Black Holes

A Kerr BH is an uncharged rotating compact object. The space-time around them is described by the Kerr metric, which is axially symmetric, stationary and asymptotically flat. In Boyer-Lindquist coordinates the line element is [34]

$$ds^2 = -\frac{\Delta}{\rho^2}(dt - a \sin^2 \theta d\phi)^2 + \frac{\rho^2}{\Delta}dr^2 + \rho^2 d\theta^2 + \frac{\sin^2 \theta}{\rho^2}(a dt - (r^2 + a^2)d\phi)^2, \quad (4.1)$$

where $\rho = r^2 + a^2 \cos^2 \theta$, $\Delta = r^2 - 2Mr + a^2$ and $a = J/M$ is the angular momentum per unit mass.

There are two surfaces of interest regarding Kerr BHs, the event horizon and the ergosphere. The first one is given by $\Delta = 0$ and the resulting solution is $r_H = M \pm \sqrt{M^2 - a^2}$. Clearly radius that will be considered is the exterior one, that is noted as r_+ . The ergosphere radius is obtained by $g_{tt} = 0$ that gives $r_e = M \pm \sqrt{M^2 - a^2 \cos^2 \theta}$. Again the sign chosen is the plus.

It will be useful to find the angular velocity of the event horizon Ω_H . This parameter is given by multiplying the Kerr metric in eq.4.1 by Δ/dt^2 , evaluating it at r_+ ($dr = 0$) and considering the equatorial plane ($\theta = \pi/2$, $d\theta = 0$). In this way every term that contains Δ is zero and in order to maintain the identity it must be

$$adt - (r_H^2 + a^2)d\phi = 0. \quad (4.2)$$

And so $\Omega_H = d\phi/dt = a/(r_+^2 + a^2) = a/2Mr_+$ since $r_+^2 + a^2 = 2Mr$ because $\Delta = 0$ at the horizon.

The ergoregion is delimited by r_+ and r_e and it is shown in Fig.4.1

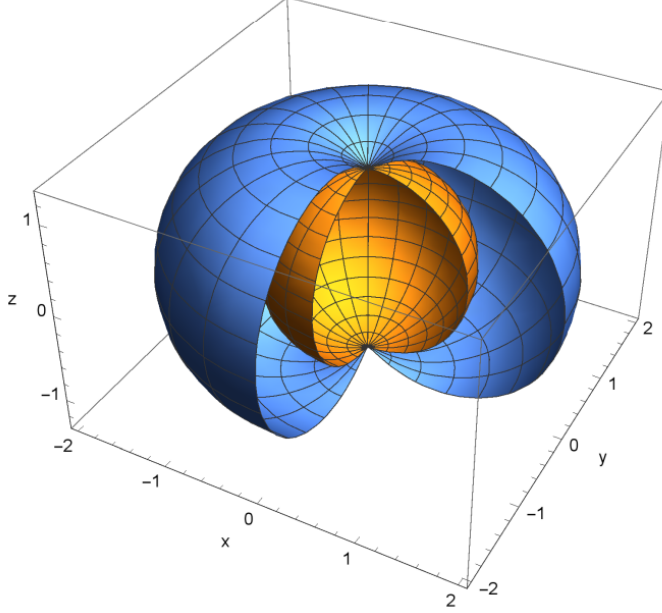


Figure 4.1: A Kerr BH is surrounded by the event horizon (orange surface) and by the ergosphere (blue surface). At $\theta = 0$ the radii of the two surfaces are equal and the maximum separation is in the equatorial plane at $\theta = \pi/2$. The ergoregion is in between these two limits (Figure from [34]).

In the ergoregion no observer can stay at rest, but it is forced to rotate with the BH.

The Kerr metric in eq.4.1 does not depend on t or ϕ , since it is stationary and axially symmetric. This means that it is possible to define the two Killing vectors [158]

$$\xi_{(t)}^\mu = (1, 0, 0, 0), \quad \xi_{(\phi)}^\mu = (0, 0, 0, 1). \quad (4.3)$$

4.1.1 The classical Penrose process

A first example of how to extract rotational energy from a Kerr BH was studied by Penrose in 1971 [129]. The most simple configuration is to consider a particle infalling into the ergoregion and undergoes a fragmentation. The representation can be found in Fig.4.2

The energy of a particle measured locally by an observer is $E = -p_\mu u^\mu$ where p_μ is the 4-momentum of the particle and u^μ the 4-velocity of the observer. If the observer is at rest, the 4-velocity coincide with the first killing vector in eq.(4.3). From the conservation of 4-momentum, it is possible to rewrite that law in a conservation of energy

$$E_0 = E_1 + (-p_2 \xi_{(t)}^\mu). \quad (4.4)$$

If $p_2 \xi_{(t)}^\mu > 0$ it means that the energy of the outgoing daughter particle is greater than the original infalling one [147], [108]. The killing vector is timelike at infinity ($\xi_\mu \xi^\mu < 0$) and spacelike in the ergosphere ($\xi_\mu \xi^\mu > 0$). This assure the presence of an orbit with negative energy in the ergoregion if measured by an observer at infinity [166].

However, even though the mathematical description is allowed, in order to extract a relevant amount of rotational energy from the Kerr BH, the particle that fall inside the event horizon and the original one should have a velocity difference of the order $\Delta v \sim 0.5$ [154].

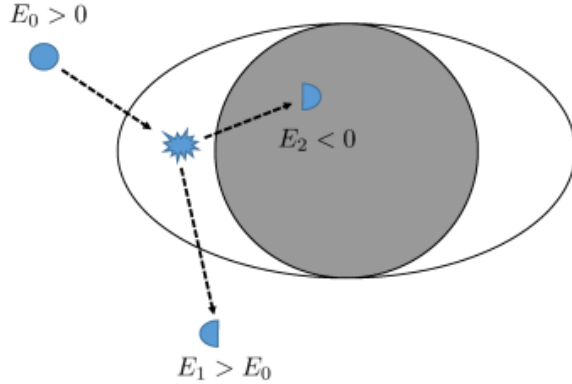


Figure 4.2: Schematic representation of the classic Penrose process. A body with energy E_0 enter the ergoregion and decay into two particles. One of them is swallowed by the BH, while the second one manages to get out of the ergoregion. There are specific trajectories for which the energy of this last particle is greater than the energy of the original infalling one (Figure from [34]).

4.2 The superradiance condition

The Penrose effect is a method thanks to which particles can steal rotational energy from a Kerr BHs. However, the effect does not work for wave field. Superradiance is a physical process that can be present in dissipative systems. Dissipation can occur through viscosity which is always present around BH and this can be explained by the membrane paradigm [96].

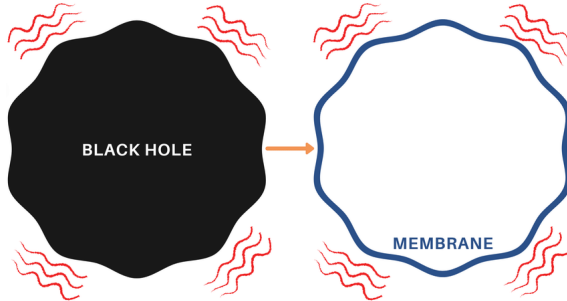


Figure 4.3: The membrane paradigm in a picture. By creating an imaginary surface around the BH, it is possible to think that inside this membrane there is vacuum and outside of it the space-time is the one we can observe. The membrane has properties that are set to fit the phenomenology of the BH (Figure from [103]).

The idea is to imagine a fictitious viscous membrane in the vicinity of the event horizon so that everything that is outside behave as usual, while the interior of the coat is considered completely vacuum. The properties of the membrane like viscosity, pressure or density are set to reproduce the phenomenology of the BH. This has been very useful to obtain several BH parameters

The superradiance condition is a direct consequence of the first and second laws of BH thermodynamics [42]. From the first law

$$\delta M = \frac{\kappa}{8\pi} \delta A_H + \Omega_H \delta J + \Phi_H \delta Q, \quad (4.5)$$

where $\kappa = 2\pi T_H$ is the surface gravity, T_H the characteristic Hawking radiation temperature, A_H the horizon area, Φ_H the electrostatic potential at the horizon and Q the charge of the BH. In

in the present case the BH is not charged. For the second law, it is known that the horizon surface always increases, so $\delta A_H > 0$.

Given the killing vectors in [4.3] and the stress-energy tensor $T_{\mu\nu}$, the conserved energy and angular momentum fluxes can be written as [34]

$$\epsilon^\mu = -T^{\mu}_{\nu}\xi_{(t)}^{\nu}, \quad l^\mu = T^{\mu}_{\nu}\xi_{(\phi)}^{\nu}. \quad (4.6)$$

The energy and angular momentum fluxes through an area $d\Sigma_\mu = n_\mu ur^2 dt d\Omega$, with n_μ its radial normal outgoing vector to the hypersurface, are $\delta E = \epsilon^\mu d\Sigma_m u$ and $\delta J = l^\mu d\Sigma_m u$. The ratio of these quantities gives

$$\frac{\delta J}{\delta E} = -\frac{T^r_\phi}{T^r_t} = -\frac{T_{r\phi}}{T_{rt}}. \quad (4.7)$$

The stress-energy tensor is given by $T_{\mu\nu} = \partial_\mu\psi\partial_\nu\psi - g_{\mu\nu}\psi^\alpha\psi_\alpha/2$ and the scalar field can be expressed by $\psi(t, r, \theta, \phi) = f(r, \theta)\exp(-i\omega t + im\phi)$. m is the azimuthal quantum number, and ω the monochromatic frequency of the field [34]. In the Kerr metric, eq[4.7] gives

$$\frac{\delta J}{\delta E} \sim \frac{\delta J}{\delta M} = \frac{m}{\omega}. \quad (4.8)$$

Using this equation into eq[4.5] is the final step to obtain the condition for mass extraction from a Kerr BH

$$\frac{\delta M}{\delta M} = \frac{\frac{\omega\kappa}{8\pi}\delta A_H}{\omega - m\Omega_H} < 0. \quad (4.9)$$

Since for the second law of BH thermodynamics, δA_H is always positive, the superradiance condition is then

$$\omega < m\Omega_H. \quad (4.10)$$

Another condition can be found on the mass of the boson if it is considered the following result. Any perturbation on the Kerr BH is stable if the mass of the boson respect $\mu \geq m\Omega_H\sqrt{1+2M/r_+}$. Since the maximum value of the square root is 2, given that the max value of r_+ is $2M$ for BH that are not spinning, the condition on the mass of the boson for superradiance to be effective is $\mu < \sqrt{2}m\Omega_H$ [25], [26]

4.3 The Black Hole Bomb

The superradiance of Kerr BHs surrounded by a boson cloud is ruled by the gravitational coupling α which is defined as the ratio between the gravitational radius of the BH $r_G \sim M$ and the Compton wavelength of the field $\lambda_C \sim \mu^{-1}$. The gravitational coupling is then $\alpha_G = M\mu$ [53].

As we will see in this section, the first mode of the classic bosonic field is unstable for $M\mu < 1$. For this condition, the field has to be ultralight, otherwise the superradiance would be relevant only for Kerr BHs with a small mass. This field is then a candidate as FDM for the necessity of extremely small masses and superradiance of rotating BH is a promising method to prove the existence of axion-like particles. For example, the range of mass that the boson can have goes from 10^{-20} to 10^{-10} eV, since astrophysical BH can have a mass of some M_\odot to $10^{10} M_\odot$ [60].

We anticipate that the principal effects of the presence of bosons around a spinning BH are two: the emission of gravitational waves (GWs) and the decrease of the rotational velocity of the BH.

A boson cloud surrounding a Kerr BHs can lead to a phenomenon called "Black Hole Bomb" because of the instability in the amplification of the wave [136].

A BH bomb is ideally realized when a spinning BH is embedded into a perfectly reflecting cavity. The superradiance can enhance an incoming wave if the condition in (4.10) is respected. However, the cavity will reflect the amplified wave that will undergo again the another enhancement. The succession of reflections leads to an instability.

The field can be expressed separating the different dependencies as

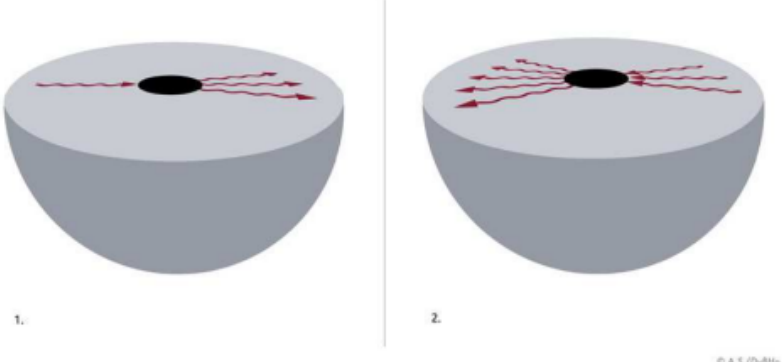


Figure 4.4: Schematic view of a BH bomb. If a wave penetrate the cavity, the superradiance effect can enhance the radiation. However, the outgoing radiation will be reflected by the mirror and will be amplified again. If this process continues, it would be created an instability (Figure from [40]).

$$\Phi = (t, r, \theta, \phi) = e^{-i(\omega t + m\phi)} S_l^m(\theta) R(r). \quad (4.11)$$

$S_l^m(\theta)$ is spheroidal angular function dependent also on quantum numbers, but for simplicity it will be called just S . The behavior of this field at the boundary of interest, so the horizon and at infinite distance, scales like [41]

$$\begin{cases} \Phi \sim \frac{e^{-i\omega t}}{r} e^{\pm i\omega r_*} & r \rightarrow \infty, \\ \Phi \sim e^{-i\omega t} e^{-i(\omega - m\Omega_H)r_*} & r \rightarrow r_+. \end{cases} \quad (4.12)$$

Here we used the tortoise coordinate $dr_* = dr(r^2 + a^2)/\Delta$.

Considering only positive frequencies, if the superradiance condition is respected, then the wave is co-rotating with the BH. This can be seen thanks to the phase velocity $-\omega/(\omega - m\Omega_H)$ that is positive [41].

With those boundary conditions, and the requirement that the wave vanishes when approaching the mirror, located at a distance r_0 from the BH, it is possible to use the field in 4.11 to solve the Klein-Gordon equation 3.6. We can make a split the problem into two equation for the angular and radial part and find [41]

$$\frac{1}{\sin \theta} \partial_\theta (\sin \theta \partial_\theta S) + \left[a^2 \omega^2 \cos^2 \theta - \frac{m^2}{\sin^2 \theta} + A_{lm} \right] S = 0, \quad (4.13)$$

$$\Delta \partial_r (\Delta \partial_r R) + [\omega^2 (r^2 + a^2)^2 - 2Mam\omega r + a^2 m^2 - \Delta(a^2 \omega^2 + A_{lm})] R = 0. \quad (4.14)$$

A_{lm} is called separation constant and for small values of $a\omega$ it is equal to $l(l+1)$. [165]

The solution of eq.4.13 and eq.4.14 can be found numerically and the results are plotted in Fig.4.5

The frequency ω is complex. While the real part represents the actual frequency of the oscillation, while the imaginary part determine the growth rate (if positive) or decay rate (if negative). As it can be seen in Fig.4.5, the imaginary part has a critical value of r_0 , dependent on a , below which superradiance instability loses its relevance, due to an exponential suppression, and the system became stable [41]. However, this critical value does not affect the real part of ω which seems not to suffer the change of value of a .

In Fig.4.6 it is plotted the gravitational coupling α_G against the growth rate. It clear that the system reaches the maximum for $\alpha_G \sim 1/2$

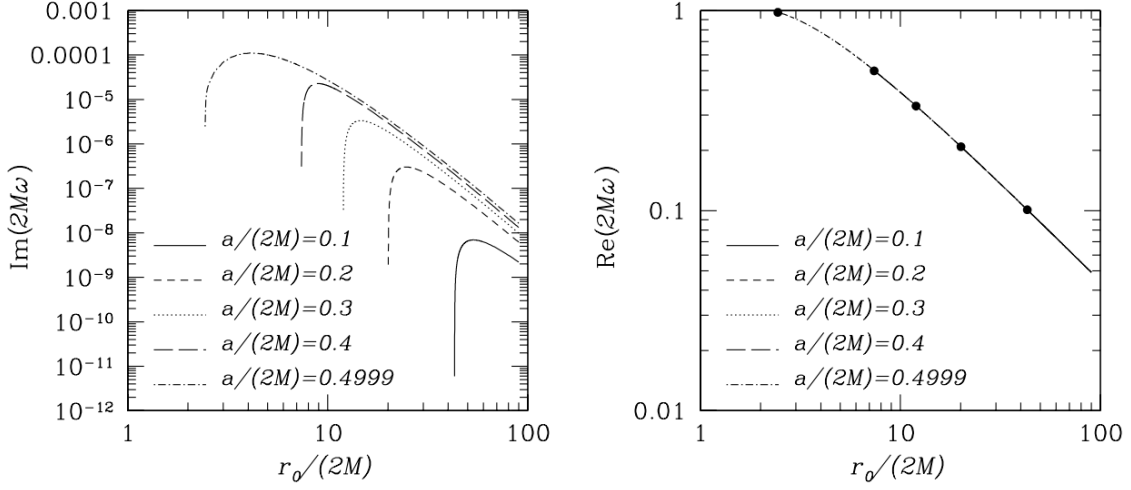


Figure 4.5: (Left) Imaginary part of the fundamental tone frequency as a function of the mirror position r_0 . The plot shows the wave with quantum numbers $l = m = 1$, $n = 0$. Depending on the value of the spin a , there is a clear drop below a critical radius r_0^{crit} . When $r < r_0^{crit}$, superradiance is no longer unstable since the imaginary part became negative, symptom of the decay of the mode. (Right) Real part of the fundamental frequency tone in the same configuration. Unlike the imaginary part, here it seems there is no clear dependence on a , but an overall r_0^{-1} trend. The dots represent the critical radius of the respective imaginary part (Figure from [41]).

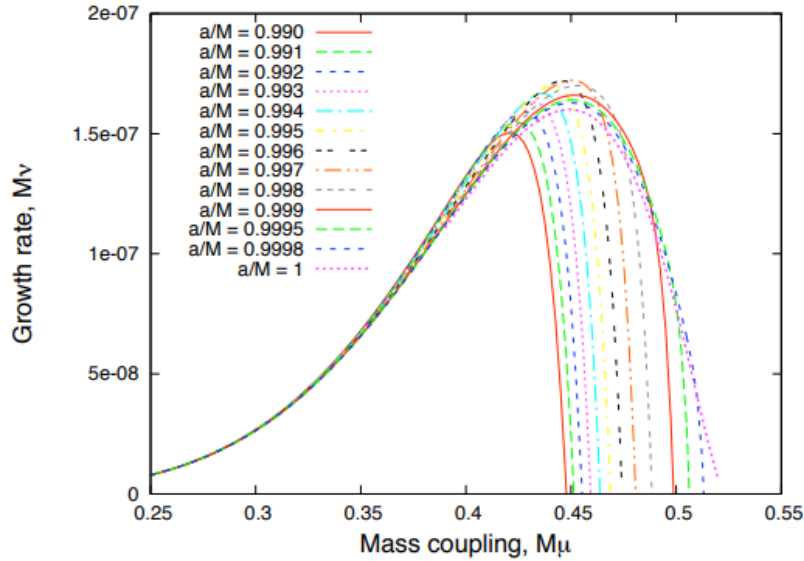


Figure 4.6: Taking the mode $l = m = 1$, $n = 0$, the plot shows the growth rate $M\nu$ against the gravitational coupling $\alpha_G = M\mu$ for different high values of spins. The common trend tells us that the peak in the growth is reached when $M\mu$ is in between 0.4 and 0.5 (Figure from [54]).

4.4 The Gravitational Atom

It is clearly impossible to build a giant spherical mirror around a BH, however as mentioned before, a natural configuration that shows the same behavior is a spinning BH surrounded by a field with a rest mass like a boson cloud [51].

Considering the Gross-Pitaevskii equation [3.31] it is possible to find an effective Schrödinger form with a Coulomb-like central potential [19]

$$i \frac{\partial}{\partial t} \psi = - \left(\frac{\nabla^2}{2\mu} + \frac{\alpha}{r} \right) \psi. \quad (4.15)$$

This formula recall the usual Schrödinger equation for the hydrogen atom, and so, due to this similarity, the boson cloud is often called "gravitational atom". The energy eigenstates can be divided into two classes:

- The bound states are identified by the quantum numbers $|nlm\rangle$. The wavefunction is defined by $\psi = R_{nl}(r)Y_{lm}(\theta, \phi) \exp[-i(\omega_{nlm} - \mu)t]$ where Y_{lm} are spherical harmonics and R_{nl} are the hydrogen radial functions for different values of the quantum numbers. The radial functions are given by [18]

$$R_{nl}(r) = \sqrt{\left(\frac{2\mu\alpha}{n}\right)^3 \frac{(n-l-1)!}{2n(n+l)!}} \left(\frac{2\alpha\mu r}{n}\right)^l e^{-\frac{\mu\alpha r}{n}} L_{n-l-1}^{2l+1}. \quad (4.16)$$

The frequency is complex and it can be written as $\omega_{nlm} = E_{nlm} + i\Gamma_{nlm}$ with [16]

$$\begin{cases} E_{nlm} = \mu \left(1 - \frac{\alpha^2}{2n^2}\right), \\ \Gamma_{nlm} = 2\tilde{r}_+ C_{nlm} (m\Omega_H - \omega_{nlm}) \alpha^{4l+5}. \end{cases} \quad (4.17)$$

C_{nl} are coefficients that can be found numerically and $\tilde{r}_+ = r_+/M$.

Considering timescales long enough to allow the formation of the gravitational atom, but insufficient to perturb the binary inspiral system, the energy level of the bound states is $\epsilon_{nlm} = \mathcal{R}e[\omega_{nlm}] - \mu$;

- The unbound states are represented by the energy and two quantum numbers $|\epsilon; lm\rangle$. The imaginary part of the frequency Γ_{nlm} is given by the dissipative nature of the event horizon, so in this case it is absent. The energy of these states is then $\epsilon = \omega - \mu = k^2/2\mu$ with k the wavenumber.

All bound and unbound states are orthonormalized

4.5 Binary Inspiral System

The superradiance effect proceeds as long as the condition [4.10] holds. However, while spinning down, Ω_H will inevitable decrease and at some point superradiance will no longer be effective. The evolution of the spin can be tracker thanks to the Regge plane.

The critical issue is that the two effects linked to the presence of a boson cloud (BH spin down and GW emission) are too small so it is very difficult to be sure about the actual presence of a ultralight field. However, there is a unique mark if the cloud is part of a binary system since the companion can "ionize" it.

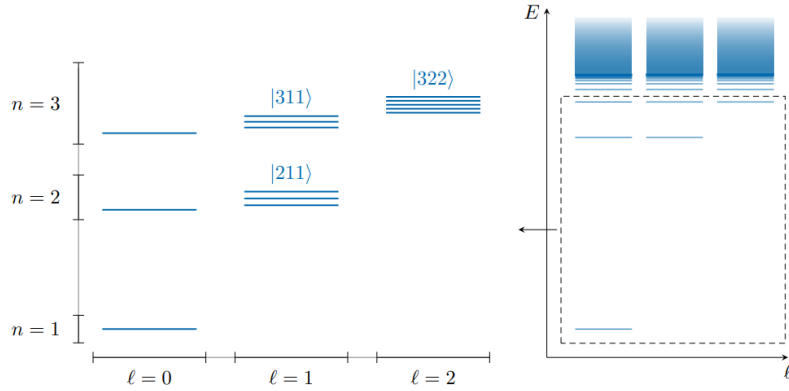


Figure 4.7: Bound and unbound states of the gravitational atom (Figure from [18]).

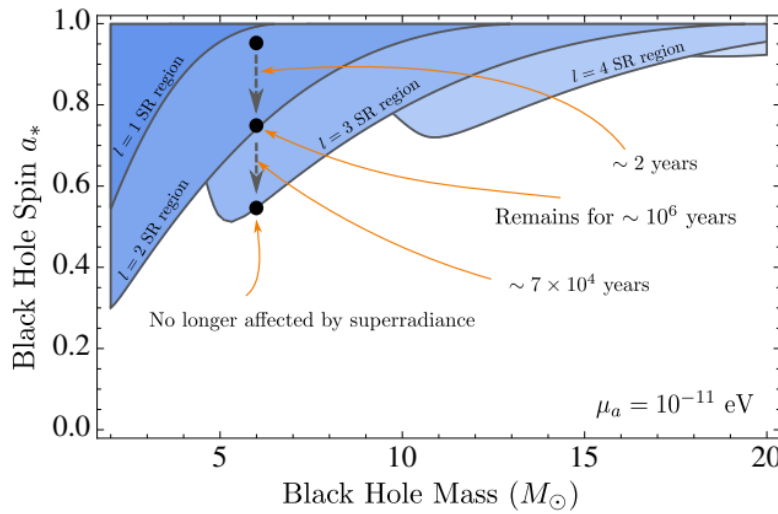


Figure 4.8: The Regge plane plot the dimensionless spin a_* versus the mass of the BH. In this case it is taken an initial spin of 0.95, a mass of $6 M_\odot$ and an ultralight scalar field of mass $\mu = 10^{-11} \text{ eV}$. The colored regions indicate where the superradiant effect is relevant for different values of the quantum number l . Superradiance is responsible for the spin down of the BH, so the compact object will cover a trajectory in the plane towards lower values of a_* until it get out from the superradiant regions when the condition $\omega < m\Omega_H$ will be no longer true (Figure from [6]).

4.5.1 The gravitational effect of the companion

The presence of the companion has a gravitational impact on the dynamics of the system BH-cloud. The energy eigenfunctions of the gravitational atom are analogous to the hydrogenic levels, so it is possible to apply the same treatment. The companion perturb the Kerr metric giving a overall space-time $g_{\mu\nu} = g_{\mu\nu}^{Kerr} + \delta g_{\mu\nu}$. The perturbation is given by the effect of the companion and the tidal response of the system BH-cloud. In this treatment it will be ignored the latter contribution [16]

Taking the schematic representation in Fig.4.9, we introduce the following parameters [16]

- Center of mass coordinate $\rho = \frac{Mr_1 + \mu r_2}{M + \mu}$;
- Spatial separation BH-cloud $r = r_2 - r_1$;
- Reduced mass $\hat{\mu} = \frac{M\mu}{M + \mu}$;
- Momentum $p_\rho = (M + \mu)\dot{\rho}$ and $p_r = \hat{\mu}\dot{r}$;
- Coordinates relative to the center of mass $\mathbf{R}_*(R_*, \Theta_*, \Phi_*)$ and $\bar{r}(\bar{r}, \bar{\theta}, \bar{\phi})$;

The Hamiltonian of the 3-body system is given by

$$\begin{aligned} \mathcal{H} &= \mathcal{H}_{BH-cloud} + \mathcal{H}_* \\ &= \left[\frac{\mathbf{p}_p^2}{2(M + \mu)} + \frac{\mathbf{p}_r^2}{2\hat{\mu}} + V_c(|\mathbf{r}|) \right] + \left[\frac{\mathbf{p}_*^2}{2M_*} + V_*(\hat{\mathbf{r}}, \mathbf{R}_*) \right]. \end{aligned} \quad (4.18)$$

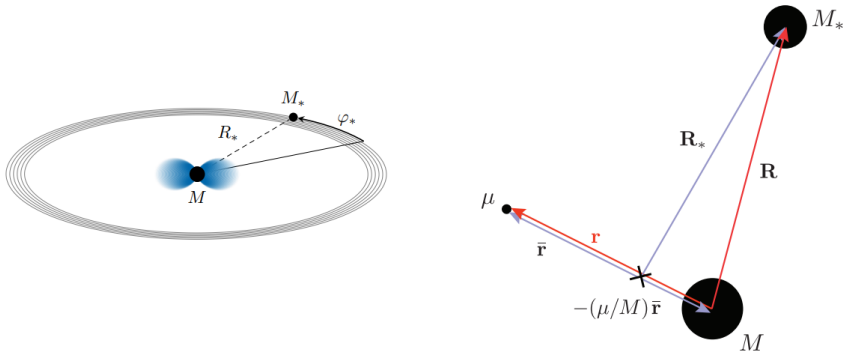


Figure 4.9: (Left) The position of the companion of mass M_* around the central Kerr BH can be described by the orbital separation R_* and the anomaly ϕ_* [19] (Right) The system is now describable with the formalism of the 3 body problem (Figure from [16]).

Working in the Newtonian limit by asking that objects move slowly with respect to c , the potential induced by the companion is given by [16]

$$V_*(\hat{\mathbf{r}}, \mathbf{R}_*) = -M_* \sum_{l_* m_*} \frac{4\pi}{2l_* + 1} \left(\frac{M(-\mu/M)^{l_*} + \mu}{R_*} \right) \left(\frac{\bar{r}}{R_*} \right)^{l_*} Y_{l_* m_*}^*(\Theta_*, \Phi_*) Y_{l_* m_*}(\bar{\theta}, \bar{\phi}). \quad (4.19)$$

Since $\hat{r} + \mu\hat{r}/M = r$, it is possible to write the potential in term of the separation BH-cloud and then expanding for the realistic case $\mu/M \ll 1$. Eq.4.19 became

$$V_*(r, R_*) = -\frac{M_*(M + \mu)}{R_*} - \frac{M_*\mu}{R_*} \sum_{l_* > 2|m_*| < l_*} \frac{4\pi}{2l_* + 1} \left(\frac{r}{R_*}\right)^{l_*} Y_{l_* m_*}^*(\Theta_*, \Phi_*) Y_{l_* m_*}(\theta, \phi). \quad (4.20)$$

The first term is not considered. It depends only on the distance of the companion, so it does not bring some type of contribution for the energy spectrum. The second term start its sum at $l_* = 2$ since $l_* = 1$ represents a dipole, which has zero contribution in the center of mass frame. We will refer to the second term as our V_* .

It is important to note that the potential V_* is quasi periodic. This behavior is obtain if it is considered a limited timescale in order to have small changes in time in the companion orbital frequency $\Omega = \pm d\phi_*/dt$ (+ for co-rotating orbits and - for counter-rotating ones). The law that determine the evolution of the orbital frequency is [131]

$$\frac{d\Omega}{dt} = \frac{96}{5} \frac{q}{(1+q)^{1/3}} M^{5/3} \Omega_0^{11/3} \left(\frac{\Omega}{\Omega_0}\right)^{11/3} = \gamma \left(\frac{\Omega}{\Omega_0}\right)^{11/3}. \quad (4.21)$$

It is introduced the chirp rate γ and a frequency of reference Ω_0 .

By solving this differential equation through separation of variables and integrating between Ω_0 at $t_0 = 0$ and Ω at time t , we end up with the equation for the orbital frequency of the companion

$$\Omega^{-11/3} d\Omega = \frac{\gamma}{\Omega_0^{-11/3}} dt \implies \Omega = \Omega_0 \left(1 - \frac{8\gamma t}{3\Omega_0}\right)^{-3/8}. \quad (4.22)$$

We have to choose a timescale for which Ω is very close to Ω_0 i.e. Ω is quasi-constant. The condition is then $8\gamma t / 3\Omega_0 \ll 1$ and so $t \ll 3\Omega_0 / 8\gamma$. Note that if the time is exactly equal to that value, it means that $\Omega = 0$ and so that time is the time of merge.

Considering the time condition, eq. 4.22 can be linearized according to $(1+x)^\alpha \sim 1 + \alpha x$

$$\phi_* = \int \Omega dt = \phi_0 + \Omega t + \frac{1}{2} \gamma t^2. \quad (4.23)$$

4.5.2 Overview on the energetic transition

The bound states $|n, l, m\rangle$ defined by the quantum numbers are labeled $|b\rangle$. The transition from a level $|b\rangle$ to another bound state $|a\rangle$ triggered by the presence of the companion potential, is dependent on the transition matrix element $\eta_{ab}(t) = \langle a | V_*(t) | b \rangle$.

Since the perturbation given by the companion is quasi-periodic, as seen in the previous section, it means that Ω changes slowly. This means that the matrix element η can be written with the Fourier coefficients. The states $|a\rangle$ and $|b\rangle$ have their own angular momentum m_a and m_b

$$\eta_{ab}(t) = e^{-i(m_a - m_b)\phi_*(t)} \eta_{ab}^{(m_a - m_b)}(t). \quad (4.24)$$

The transition is in particular resonant if the angular velocity of the companion matches the energy difference between the two states. The exponential in eq. 4.24 can be seen as $e^{-i\Delta E t}$ and this means that the resonant condition, for quasi-circular equatorial orbit, is given by [17]

$$(m_a - m_b)\Omega(t) = E_b - E_a. \quad (4.25)$$

It is worth remembering that Ω can be positive or negative for co-rotating and counter-rotating orbits, so the resonant frequency and, in general, the fingerprint effect will be slightly different depending on this sign.

For simplicity, we initially assume a single bound state $|b\rangle$ and a semi-infinite continuum of states $|k\rangle$ that do not interact with each other and are normalized $\langle k | k' \rangle = 2\pi\delta(k' - k)$. Another assumption is that the interaction bound-unbound states oscillate at frequency Ω and grows slowly ($\dot{\Omega} = \gamma$). The Hamiltonian of the gravitational atom is [18]

$$\mathcal{H} = \epsilon_b |b\rangle \langle b| + \frac{1}{2\pi} \int_0^\infty dk \left[\eta(k) e^{-i\phi_*(t)} |k\rangle \langle b| + \eta(k)^* e^{i\phi_*(t)} |b\rangle \langle k| + \epsilon_k |k\rangle \langle k| \right]. \quad (4.26)$$

In order to compute the time-dependent Schrödinger equation $i\partial_t |\psi\rangle = \mathcal{H}|\psi\rangle$, we first have to introduce the most generic state $|\psi\rangle$

$$|\psi\rangle = c_b(t)e^{-i\epsilon_b t}|b\rangle + \frac{1}{2\pi} \int_0^\infty dk c_k(t)e^{-i\epsilon(k)t}|k\rangle. \quad (4.27)$$

The companion has to do work to ionize the gravitational atom, and the energy necessary for the ionization is [18]

$$E_{ION}(t) = \frac{1}{2\pi} \int_0^\infty dk [\epsilon(k) - \epsilon_b] |c_k(t)|^2. \quad (4.28)$$

To compute the power of ionization $P_{ION} = dE_{ION}/dt$ it is then necessary knowing the equation for $c_k(t)$. That equation is obtained solving the Schrödinger equation through the system [18]

$$\begin{cases} i\frac{\partial c_b}{\partial t} = \frac{1}{2\pi} \int_0^\infty dk \eta^*(k) e^{i\phi_*(t)+i(\epsilon_b-\epsilon(k))t} c_k(t), \\ i\frac{\partial c_k}{\partial t} = \eta(k) e^{-i\phi_*(t)+i(\epsilon(k)-\epsilon_b)t} c_b(t). \end{cases} \quad (4.29)$$

The requirement we make is that the system is initially in the bound state, so $c_k(t) \rightarrow 0$ if $t \rightarrow -\infty$. In this way, the equation for $c_k(t)$ can be immediately integrated

$$c_k(t) = -i \int_{-\infty}^t dt' \eta(k) e^{i(\epsilon(k)-\epsilon_b)t'-i\phi_*(t')} c_b(t'). \quad (4.30)$$

Inserting eq[4.30] in eq[4.28], the power of ionization is given by [18]

$$P_{ION} = \frac{1}{2\pi} \int_0^\infty dk \int_{-\infty}^t dt' \left[(\epsilon(k) - \epsilon_b) |\eta(k)|^2 e^{i(\phi_*(t)-\phi_*(t'))-i(\epsilon(k)-\epsilon_b)(t-t')} c_b^*(t) c_b(t') + c.c. \right]. \quad (4.31)$$

This equation is quite complex, but it take a way easier form using the Markov approximation [71], [18]

$$P_{ION} = \frac{M_c}{\mu} \left[\mu \Omega(t) \frac{|\eta(k_*(t))|^2}{k_*(t)} \right] |c_b(t)|^2 \Theta(k_*(t)), \quad (4.32)$$

where M_c is the mass of the cloud, $k_* = \sqrt{2\mu(\Omega + \epsilon_b)}$ and Θ the Heaviside step function.

However, in reality, one should take into account other bound-bound transitions and interactions of the continuum with other free states. The Hamiltonian and the generic state are slightly different from the previous simple configuration [18]

$$\mathcal{H} = \sum_b \epsilon_b |b\rangle \langle b| + \sum_{a \neq b} a \eta_{ab} |a\rangle \langle b| + \sum_K \epsilon_K |K\rangle \langle K| + \sum_{K,b} \left[\eta K b |K\rangle \langle b| + h.c. \right], \quad (4.33)$$

$$|\psi\rangle = \sum_b \epsilon_b(t) e^{-i\epsilon_b t} |b\rangle + \sum_K c_K(t) e^{-i\epsilon_K t} |K\rangle. \quad (4.34)$$

Even though the computation for P_{ION} is analogous to the one done for the simplified model, the result must take into account the presence of overtones in the oscillations. The overtone are considered through the number $g \in \mathbb{Z}$, where the condition $|m| = |m_b + g| < l$ holds. Moreover, the realistic case includes also an infinite degeneracy due to the presence of this overtones, so now $K_* = \{k_*^{(g)}, l, m\}$ and $K_*^{(g)} = \sqrt{2\mu(g\Omega + \epsilon_b)}$. In the end, the power of ionization must be summed for all values of l and g [18]

$$P_{ION} = \sum_{lg} \frac{M_c}{\mu} \left[g \mu \Omega(t) \frac{|\eta_{K_* b}^{(g)}(t)|^2}{k_*^{(g)}(t)} \right] |c_b(t)|^2 \Theta(k_*^g(t)). \quad (4.35)$$

4.5.3 Gravitational Wave emission

Given the power of a GW [19]

$$P_{GW} = \frac{32}{5} \frac{q^2}{(1+q)^2} M^2 R_*^4 \Omega^6, \quad (4.36)$$

it is possible to plot the ratio P_{ION}/P_{GW} to see how much energy is lost due to ionization with respect to the energy loss due to GWs emission. As it can be seen in Fig 4.10, a fingerprint effect is the presence of clear jumps depending on the overtones and level considered. For the initial bound state $|b\rangle = |n_b, l_b, m_b\rangle$ the jumps appear at separation [18], [19]

$$\frac{R_*^{(g)}}{M} = \frac{1}{\alpha^2} \left[4g^2(1+q)n_b^4 \right]^{1/3}. \quad (4.37)$$

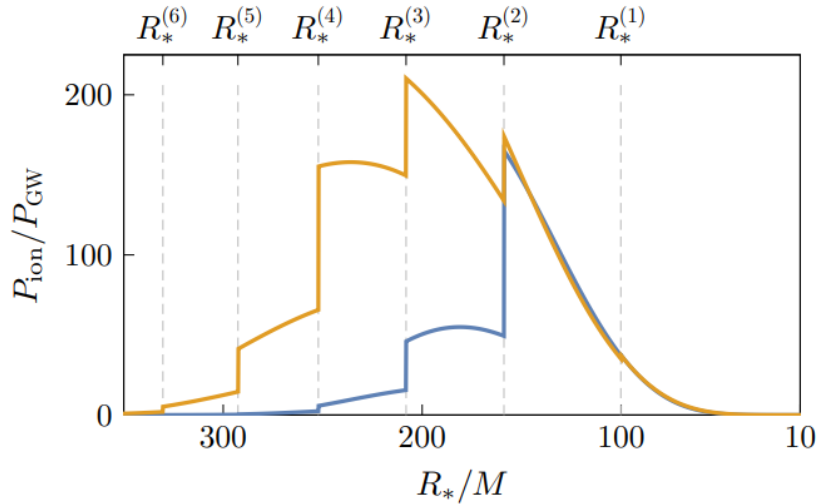


Figure 4.10: Chosen as a reference the state $|211\rangle$, $\alpha_G = 0.2$ and $M_c/M = 0.01$, we can find how much power goes into ionization with respect to the one that goes into the GWs emission. The yellow line takes into account counter-rotating orbit, while the blue curve represents co-rotating trajectories. The jumps at different overtones are a fingerprint effect of the presence of the gravitational atom (Figure from [19]).

Those kinks are a peculiar feature of the presence of a boson cloud surrounding the central Kerr BH and the mass of the particle which composes the gravitational atom can be inferred by measuring the frequency of the GWs emitted by the system.

The frequency of a GW can be written as $f_{GW} = \Omega/\pi$ and due to the fact that we have considered quasi-circular equatorial orbit for the companion, $\Omega^2 = M/R_*^3$. The dependence of the frequency of the GW to R_* links the fingerprint effect of the gravitational atom presence to the GW signal. Indeed $\Omega/R_* = (M^3/R_*^3)M^{-2}$ and we can use eq 4.37. The result is plotted in Fig 4.11. In this way, it is explicit the dependence $f_{GW} \propto \alpha^3 M^{-1} n_b^{-2}$ with $\alpha = M\mu$.

In principle, this is a powerful technique to estimate the mass of a ultralight scalar boson. Unfortunately, the parameters like q , α , M_c and even the state defined by the quantum numbers have to combine in order to give signal that can be perceived by our GW detector. The reason for this is that the frequency of GW is found numerically to be [18]

$$f_{GW} \sim \frac{33.5 \text{ mHz}}{g} \left(\frac{M}{10^4 M_\odot} \right)^2 \left(\frac{\mu}{10^{-12} \text{ eV}} \right)^3 \left(\frac{2}{n_b} \right)^2. \quad (4.38)$$

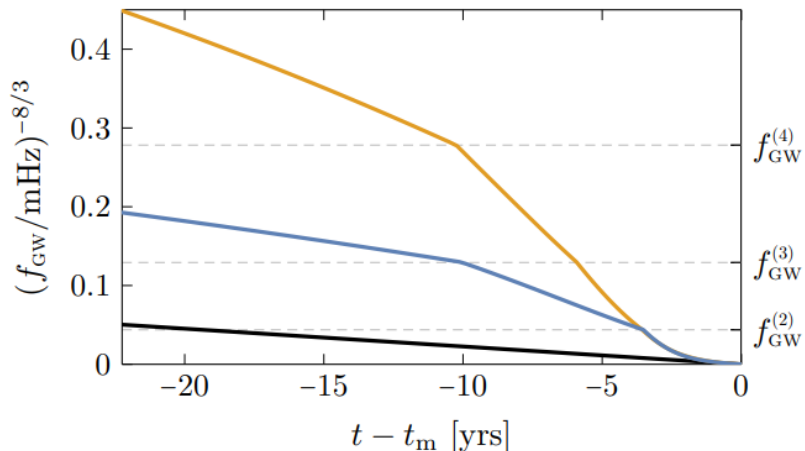


Figure 4.11: Having the state $|211\rangle$, $\alpha_G = 0.2$, $M_c/M = 0.01$, $R_* = 400M$, $q = 10^{-3}$ and $m = 10^4 M_\odot$, the plot show the GW emission frequency as we get closer to merging. The difference between the vacuum case (black line) and the one with the presence of the gravitational atom (colored line, yellow for counter-rotating orbit and blue for co-rotating) is very clear (Figure from [19]).

Chapter 5

Galaxy Alignment

Galaxies appear to be fainter and smaller as the distance from the observer increases, since it is well known that greater distances correspond to earlier times. This is the reason why galaxies are excellent candidates to study the properties and evolution of LSS. Just to mention some of those qualities [86]

- spatial and spectral light distribution with dynamical properties give us knowledge on galaxy formation and evolution;
- the galaxy density distribution follow the matter density distribution, providing us important feedback on DM;
- light samples suggest information about the geometry of space-time along the line-of-sight.

For what concern the last point, the interest goes into the ellipticity and the orientation of the galaxy. Those two properties, when the sample considered is sufficiently large, are supposed to be randomly distributed and therefore to have a zero average value because of Universe homogeneity and isotropy. For this reason, if by chance a violation of this assumption is indeed found, that would mean that galaxies show a preferred direction thus creating an alignment. This effect can be due to another phenomenon exerted by LSS, the gravitational lensing [86]

In this chapter the focus is on different types of power spectra. After a detailed treatment on how the linear and non-linear matter power spectrum are computed, they are founded thanks to the cosmology code **CAMB** and then the non-linear matter power spectrum will be used to compute the gravitational lensing power spectrum. In the end it will be noted future possibilities to implement the axion transfer function into the code **PyCosmo** to see how the axion presence affects the total lensing power spectrum, a topic that in literature is not so common to find.

5.1 Galaxy triaxial shape

As already mention in the previous chapters, the formation history of the structures in the Universe is determined by DM dynamics. The initial tiny fluctuations enhanced by inflation grew through gravitational interactions. If random motion balance the gravitational collapse, then a bound object is formed, the halo. These over-dense regions are usually triaxial shaped [10] and, following the Λ CDM bottom-up scenario, they gave rise to bigger and bigger haloes.

Haloes have an angular momentum and a shape that is typically approximated as an ellipsoid. The shape is a consequence of its mass distribution characterized by the inertia tensor I . For an halo with N_p particles, the inertia tensor components are [23]

$$I_{\alpha\beta} = \sum_{i=1}^{N_p} m_i (\mathbf{r}_i^2 \delta_{\alpha\beta} - r_{i,\alpha} r_{i,\beta}), \quad (5.1)$$

where m_i is the mass of the i-th particle, $\delta_{\alpha\beta}$ is the Kronecker delta and r_i the position relative to the halo center.

The diagonalized form of I is obtained by performing a rotation that makes the angular velocity ω and the angular momentum \mathbf{J} parallel. Calling the three semi-axis a , b and c ($a \geq b \geq c$) and the mass of the halo M_h , the inertia tensor is [23]

$$I = \frac{1}{5} M_h \begin{pmatrix} b^2 + c^2 & 0 & 0 \\ 0 & a^2 + c^2 & 0 \\ 0 & 0 & a^2 + b^2 \end{pmatrix}. \quad (5.2)$$

Eigenvectors and eigenvalues are the elements that determine the shape of the halo. A structure of a parent halo and several sub-haloes are visible in Fig. 5.1 where the ellipsoids are very clear to see

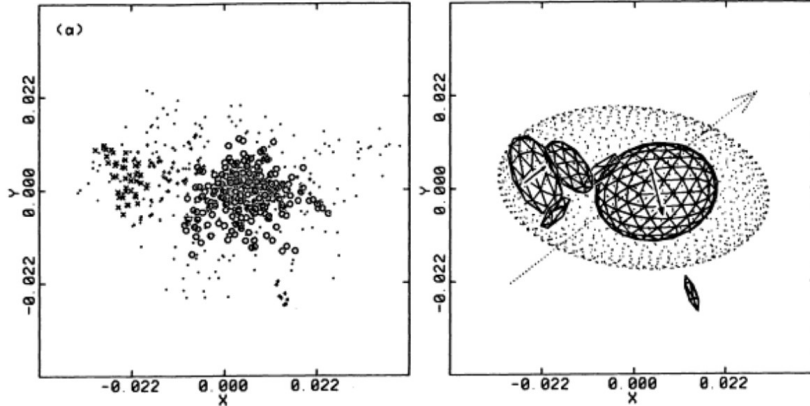


Figure 5.1: The plot shows the results of a N-body simulation. The left panel represents the positions of the massive particles. Different dots are used to identify particle with similar properties in the simulation. The right panel rearranges the contents of the left graph into smooth ellipsoids that represent the sub-halo structures. The arrows identify the angular momentum direction of the sub-halo (Figure from [11]).

The haloes evolve under gravity in order to form bigger and bigger structures up to the cosmic web (see Fig. 3.4 panel **b**). Once the halo is formed, its shape is not crystallized. Merges between DM haloes can affect dramatically the alignments [86]

- in minor merges, the smaller halo can survive inside the bigger one, but he will feel the big halo gravitational presence;
- in major merges, the two haloes are completely destructed and therefore the alignments of the original objects are entirely cancelled. A new alignment can eventually be formed.

Baryons feel the gravitational presence of haloes and accumulate towards their center adding angular momentum, for example, infalling from a specific direction. This creates a rotationally supported disc of gas. When a galaxy is formed, its alignment typically matches the one of the DM halo. However, processes like star formation, gas accretion or chemical enrichment of interstellar medium, can change the overall mass and angular momentum distribution and so the alignment

5.2 The matter power spectrum

As already mentioned in section 3.8, when the cosmology considered involves the presence of ultralight axion-like particles as DM candidate, the power spectrum changes dramatically at small scales because of a mass-dependent cut-off at high values of k (see Fig. 5.43).

The changes in $P(k)$ will of course have consequences also in every other parameter dependent on the matter power spectrum like the equation of the shear power spectrum as we will see in the next section.

In this section it is shown how the presence of axion-like particles affect the power spectrum P_γ starting from its modification of the matter power spectrum P .

5.2.1 The linear matter power spectrum

To begin with, the primordial potential $\Phi_i(\mathbf{k})$ generated during inflation is linked to the potential $\Phi(\mathbf{k}, a)$ computed at some later time through [52]

$$\Phi(\mathbf{k}, a) = \Phi_i(\mathbf{k})T(k)D(a), \quad (5.3)$$

where $T(k)$ is the transfer function which describes the evolution of the perturbation through the horizon crossing and radiation-matter transition, and $D(a)$ the growth rate that characterizes the evolution of the perturbation at late times.

In order to relate the matter overdensity δ_m to the potential Φ the simplest choice is to use the Poisson equation $\nabla^2\Phi = 4\pi G\rho$ considering late times and large values of k in Fourier space. The equation is then [52]

$$k^2\Phi(\mathbf{k}, a) = 4\pi G\rho_m(a)a^2\delta_m(\mathbf{k}, a), \quad (5.4)$$

and since the density parameter is $\Omega_m = \rho_m a^3 / \rho_{crit}$ and the Hubble parameter is $H_0^2 = 8\pi G\rho_{crit}/3$, the overdensity is

$$\delta_m = \frac{2k^2 a}{3\Omega_m H_0^2} \Phi. \quad (5.5)$$

This means that also the matter perturbation is dependent on both the transfer function and the growth rate. Being the power spectrum the Fourier Transform of the two point correlation function of the perturbation, this lead to $P \propto (TD)^2$. In particular, at late times, the linear matter spectrum is [52]

$$P_L(\mathbf{k}, a) = \frac{8\pi^2}{25} \frac{\mathcal{A}_s}{\Omega_m^2} D^2(a) T^2(k) \frac{k^{n_s}}{H_0^4 k_p^{n_s - 1}}, \quad (5.6)$$

where \mathcal{A}_s is a parameter called variance of curvature perturbations, k_p reference scale called pivot-scale (typically, when $k_p \sim 0.05 \text{ Mpc}^{-1}$, we have that $\mathcal{A}_s \sim 2.1 \cdot 10^{-9}$) and n_s is the scalar spectral index.

In the Λ CDM scenario, the growth of the perturbations is scale-independent for redshift $z \leq 100$, so, at least in linear order, the power spectrum can be obtained starting from its current value [104]

$$P_{\Lambda CDM}(k, z) = \left(\frac{D(z)}{D(z=0)} \right)^2 P_{\Lambda CDM}(k). \quad (5.7)$$

In the last equation $P_{\Lambda CDM}(k) = P_{\Lambda CDM}(k, z=0)$ and the growth rate is given by [104]

$$D(z) = \frac{5\Omega_m}{2H(z)} \int_0^{a(z)} \frac{da'}{(a'H(a')/H_0)^3}. \quad (5.8)$$

This is valid for the linear part of the matter power spectrum, unfortunately, when small scales are considered it is necessary a non-linear treatment.

5.2.2 The non-linear matter power spectrum

As already said, the structure formation in our Universe follows the bottom-up scenario in which the first objects formed are also the smallest ones. This type of formation require a non-linear treatment and the most famous one is the proposal of Peacock and Dodds [122].

Peacock and his collaborator improved the HKLM approach [70] that gives an accurate description of the transition form linear to non-linear regime considering a Universe with $\Omega = 1$. Rather than the simple power spectrum P , they worked with the dimensionless power spectrum Δ^2 given by [128]

$$\Delta^2(k) = \frac{V}{(2\pi)^3} 4\pi k^3 P(k), \quad (5.9)$$

where V is a normalization volume.

Referring to the perturbation in the density field in eq. [3.54], the two point correlation function of δ is now noted as $\zeta(\mathbf{r}) = \langle \delta(\mathbf{x})\delta(\mathbf{x} + \mathbf{r}) \rangle$, which, in module, is [122]

$$\zeta(r) = \int_0^\infty \Delta^2(k) \frac{\sin(kr)}{kr} \frac{dk}{k}. \quad (5.10)$$

If r_L is the comoving linear coordinate and r_{NL} the non-linear one, these two length are related by [128, 70]

$$r_L = (1 + \bar{\zeta}_{NL}(r_{NL}))^{1/3} r_{NL}, \quad (5.11)$$

where $\bar{\zeta}$ is the volume-averaged correlation function $\bar{\eta}(r) = 3r^{-3} \int_0^r \zeta(x) x^2 dx$. The presence of the volume-averaged $\bar{\zeta}$ is due to the fact that the collapse is triggered when the integrated overdensity reaches a critical value.

According to Peacock [122], the correlation $\bar{\zeta}$ could be thought as the dimensionless power spectrum if instead of r it is considered the wavenumber k . Eq. [5.11] becomes then

$$k_L = (1 + \Delta_{NL}^2(k_{NL}))^{-1/3} k_{NL}. \quad (5.12)$$

From Hamilton paper [70] it is known that the linear and non-linear power spectrum are related by some function

$$\Delta_{NL}^2(k_{NL}) = f[\Delta_L^2(k_L)], \quad (5.13)$$

with the empirical result of $f(x) \sim 11.68 x^{3/2}$. Thanks to Peacock et. al [122] f can be now expressed through an analytic equation that includes the case $\Omega \neq 1$

$$f(x) = x \left[\frac{1 + 0.2\beta x + (Ax)^{\alpha\beta}}{1 + ([Ax]^\alpha g^3(\Omega)/[11.68x^{1/2}])^{1/2}} \right]^{1/\beta}, \quad (5.14)$$

where $A = 0.84[g(\Omega)]^0.2$, $\alpha = 2/g(\Omega)$ and $\beta = 2g(\Omega)$. The function $g(\Omega)$ is the growth factor [43]

$$g(\Omega) = \frac{5}{2}\Omega_m \left[\Omega_m^{4/7} - \Omega_\nu + (1 + \frac{\Omega_m}{2})(1 + \frac{\Omega_\nu}{70}) \right]^{-1}. \quad (5.15)$$

This proposal for Δ_{NL}^2 was tested [82] since eq. [5.13] was not coherent with simulations for a spectral index of $n = -2$, for example. Smith et. al [150] gave an alternative in the description of the non-linear power spectrum through a separation of the components

$$P_{NL}(k) = P_Q(k) + P_H(k), \quad (5.16)$$

where P_Q represents the quasi-linear term and P_H the halo (non-linear) part.

Considering a mass function $n(M)dM$, the Fourier Transform of the density profile $\tilde{\rho}(k, M)$ and the bias field of the DM halo seed $b(M)$, the quasi-linear term is given by [150]

$$P_Q(k) = P_L(k) \left[\frac{1}{\rho} \int dM b(M) n(M) \tilde{\rho}(k, M) \right]^2. \quad (5.17)$$

However, in order to fit the data, it is necessary to take an empirical approach for the requirement that the quasi-linear term must be suppressed at large value of k . In order to formulate the dimensionless power spectrum, we need first to introduce the non-linear scale k_σ

Thanks to several studies, it is known that the halo mass function depends only on the dimensionless fluctuation amplitude [150, 83]

$$\nu = \frac{\delta_c}{\sigma(R)}, \quad (5.18)$$

where the numerator is a constant of order unity, while the denominator is the variance in the linear density field. Since this variance is dependent on k

$$\sigma^2(R) = \int \Delta_L^2 e^{-K^2 R^2} dl nk, \quad (5.19)$$

it is possible to define a scale k_σ for which $\sigma(k_\sigma^{-1}) = 1$.

Now, defining the scale $y = k/k_\sigma$, the empirical quasi-linear term is [150]

$$\Delta_Q^2(k) = \Delta_L^2(k) \frac{[1 + \Delta_L^2(k)]^{\beta_n}}{1 + \alpha_n \Delta_L^2(k)} e^{-f(y)}, \quad (5.20)$$

with α_n and β_n coefficients spectral dependent and $f(y) = y/4 + y^2/8$.

On the other hand, the halo term is [150, 123]

$$P_H(k) = \frac{1}{\bar{\rho}^2(2\pi)^3} \int dM n(M) |\tilde{\rho}(k, M)|^2. \quad (5.21)$$

The empirical dimensionless power spectrum is

$$\begin{cases} \Delta_H^2(k) = \frac{\Delta_H^{2'}(k)}{1 + \mu_n y^{-1} + \nu_n y^{-2}} \\ \Delta_H^{2'}(k) = \frac{a_n y^3}{1 + b_n y + c_n y^{3-\gamma_n}}. \end{cases} \quad (5.22)$$

All the spectrum-dependent coefficients noted with the index n can be found in the Appendix C of Smith et al. [150].

Considering the axion transfer function introduced in sec. 3.8, the matter power spectra affected by the axion presence are plotted for different masses m_a and different redshifts z respectively in Fig. 5.2 and Fig. 5.3.

5.3 Gravitational Lensing

The property on which this effect is based is that light follow geodesics, trajectories that are characterized by the absence of all non-gravitational forces. In a FLRW geometry, geodesics are straight lines, while, considering a curved space-time, they will be curved too.

The advantage of the gravitational lensing effect is that it can experimentally probe the whole mass distribution. Other methods probing LSS like galaxy clustering or the Sunyaev-Zel'dovich effect (affect the apparent brightness of the CMB radiation towards a cluster of galaxies [27]) the can account for only the baryonic distribution.

The geometry of the gravitational lensing effect is schematically represented in Fig. 5.4.

Gravitational lensing is an effect that can be divided into two categories, depending on the strength of the distortion of the image:

- Background sources close in angular position to the massive object, the lens, show multiple images of the same object oriented tangentially into arcs around the center of the lens. This is the strong gravitational lensing and one example of it is the Einstein ring in Fig. 5.5.
- When the angular distance between the lens and the object increases, there are no more multiple images of the same source and the lensing effect is just small modifications to the light profile of the source. In this case, we talk about weak gravitational lensing and it is the most interesting case for cosmological studies.

Change in the image at first order are given by the following matrix [12, 86]

$$\mathbf{A} = (1 - \kappa) \mathbb{1}_2 - |\gamma| \begin{pmatrix} \cos 2\phi & \sin 2\phi \\ \sin 2\phi & -\cos 2\phi \end{pmatrix}. \quad (5.23)$$

In this matrix there are the introduction of the convergence parameter κ responsible for isotropic stretches of the source, the gravitational shear $\gamma = \gamma_1 + i\gamma_2$ that quantify the distortion and ϕ that is the polar angle that describes the orientation of the galactic ellipse.

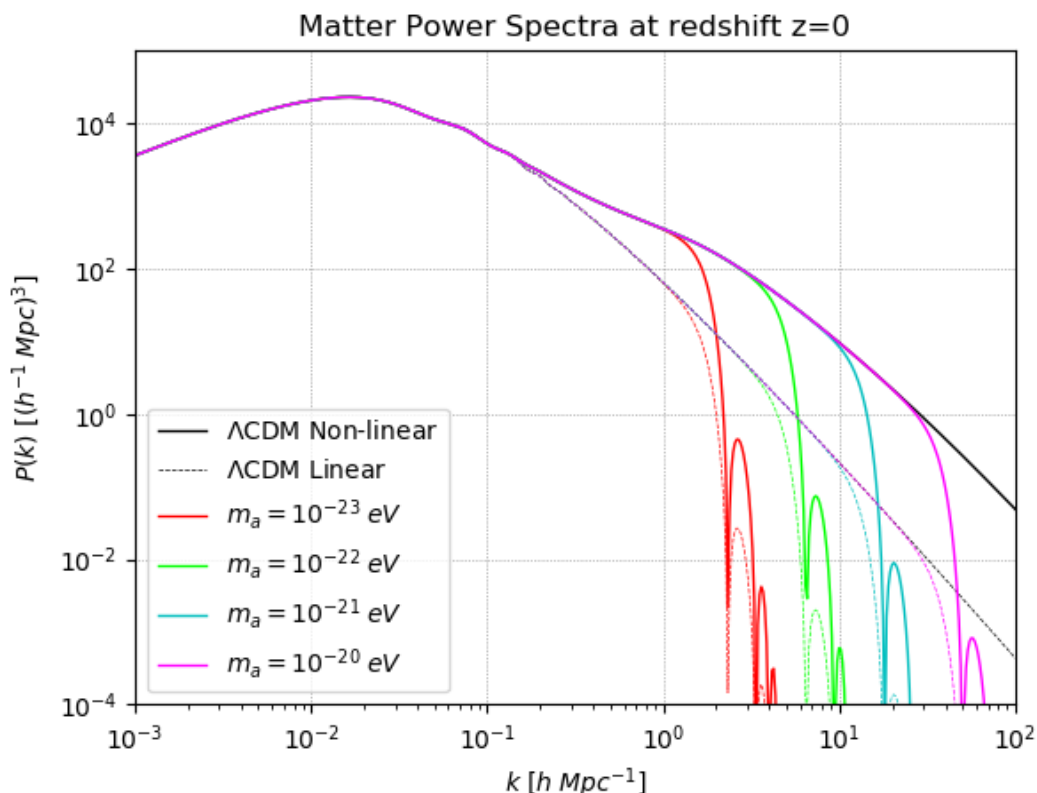


Figure 5.2: In this plot is shown in different colors the impact of axions on the non-linear matter power spectrum (solid lines) considering always redshift $z = 0$. The lighter the mass of the axion, the smaller is the wavenumber at which the power spectrum drops. The dotted lines represent the same elements but considering the linear matter power spectrum

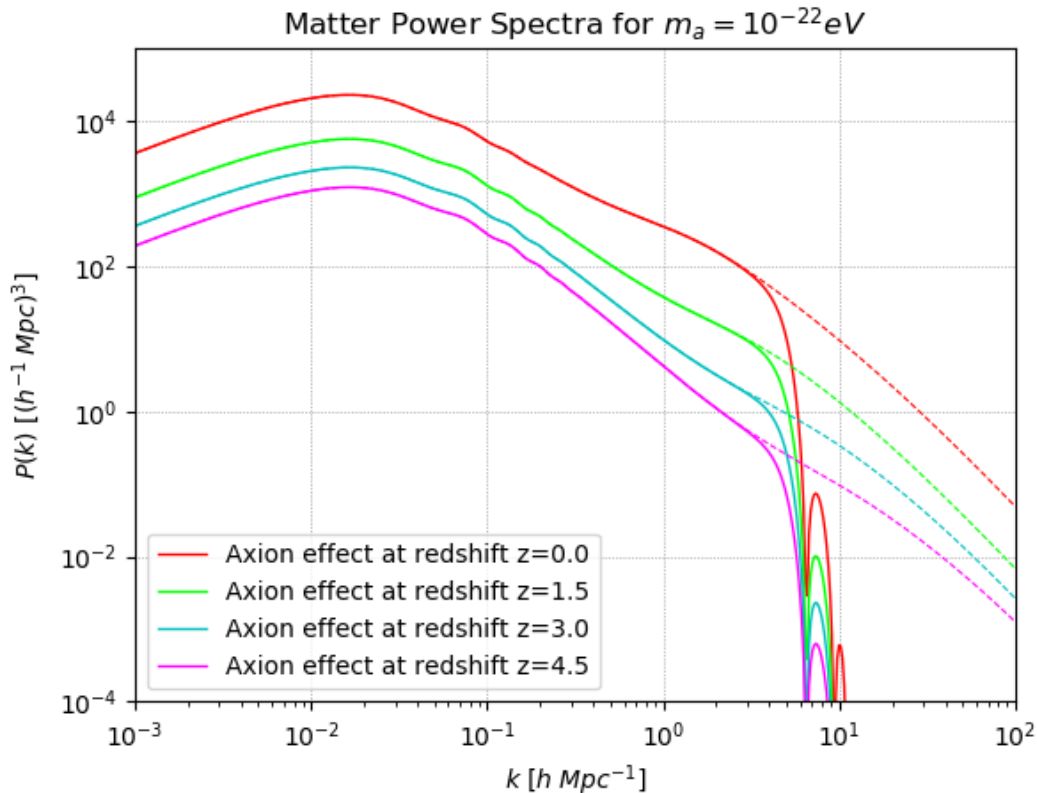


Figure 5.3: As in the previous plot, here we can see the effect of the presence of an axion on the non-linear matter power spectrum. This time, the variable is the redshift and the axion mass is considered a constant of 10^{-22} eV . Since the cut-off depends only on $m_a = \text{const}$, it is present always at the same scale for every values of redshift. The dotted lines are the non-linear matter power spectrum at different z not considering the axion effect

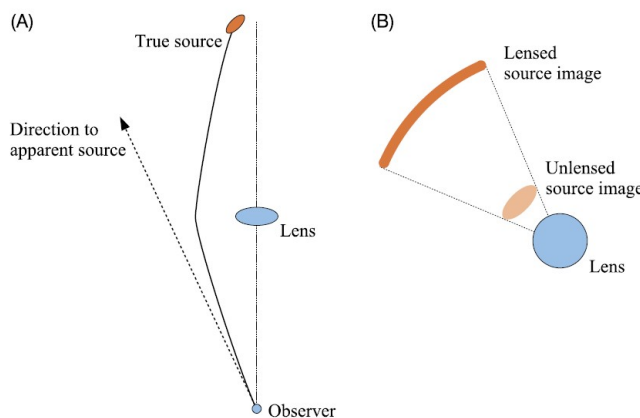


Figure 5.4: Geometry of the lensing effect. (Left) a top view of the path of light deflected by the lens (solid line) and the apparent direction of the source (dotted line). (Right) the front view of how the source is distorted. The overall effect is that the lensed image is thinner and longer than the unlensed one and its orientation is tangential to the lens. (Figure from [52]).

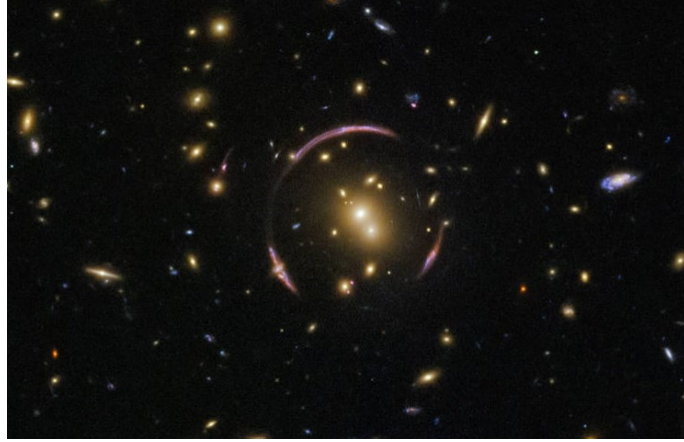


Figure 5.5: Image of SDSS J0146-0929, a galaxy cluster whose mass large enough to perturb the surrounding space-time and cause a lensing effect. The light of farther sources is deflected into different direction producing multiple images of the same object. The result of this light deflection is the formation of a ring-shaped structure around the cluster known as the "Einstein ring" (Figure from [56]).

As one can observe from the scheme in Fig. 5.4, the lensed images cover an higher surface than the real source. This translates in a magnification effect of gravitational lensing. Given the matrix \mathbf{A} , the magnification μ is given by $\mu = |\det \mathbf{A}|^{-1}$ [148].

Galaxies that do not show a circular shape have an intrinsic ellipticity ϵ^s . However, lensing leads to a distorted image and so the ellipticity that is observed ϵ will be different from the intrinsic one [86]. The two are related through

$$\epsilon = \frac{\epsilon^s + g}{1 + \epsilon^s g^*}, \quad (5.24)$$

where $g = \gamma/(1 - \kappa)$ is the reduced shear, g^* its conjugate and with the assumption of $\det \mathbf{A} > 0$ [148].

Given the complex nature of the shear, it is immediate to see that also the ellipticity ϵ is a complex parameter. It can be expressed in a polar form $\epsilon = |\epsilon|e^{2i\phi}$, where $|\epsilon|$ gives the shape and ϕ the orientation with respect to some reference axis. In the weak lensing limit ($|\gamma|, \kappa \ll 1$), the ellipticity can be approximated as $\epsilon = \epsilon^s + \gamma$ [86]. For this reason, when a reasonable large sample of galaxy is considered, the ensemble average of ellipticity will be given only by the shear ($\langle \epsilon \rangle = \gamma$), since the randomness distributed orientation of the galaxies makes $\langle \epsilon^s \rangle = 0$. Repeating the same reasoning for an even larger sample of galaxies, the shear is also supposed to vanish due to isotropy. This makes it possible to consider γ as a random field that depends on the position \mathbf{x} and show a zero expectation value $\langle \gamma \rangle = 0$.

5.3.1 The shear power spectrum

Considering the shear in two different galaxies located in \mathbf{x} and \mathbf{x}' with respect to a reference frame, the two point correlation function is [13]

$$\langle \gamma(\mathbf{x}) \gamma^*(\mathbf{x}') \rangle = C_{\gamma\gamma}(|\mathbf{x} - \mathbf{x}'|). \quad (5.25)$$

It is well known that it is possible to go in Fourier space to obtain the power spectrum. The Fourier Transform (FT) of a function is $\hat{f}(\mathbf{k}) = \int dk f(x) e^{i\mathbf{x}\cdot\mathbf{k}}$ and so, considering \mathbf{x} a vector of n dimensions, the FT of eq. 5.25 is

$$\langle \hat{\gamma}(\mathbf{k}) \hat{\gamma}^*(\mathbf{k}') \rangle = \int d^n x e^{i\mathbf{x}\cdot\mathbf{k}} \int d^n x' e^{-i\mathbf{x}'\cdot\mathbf{k}'} \langle \gamma(\mathbf{x}) \gamma^*(\mathbf{x}') \rangle. \quad (5.26)$$

Considering the translation $\mathbf{x}' = \mathbf{x} + \mathbf{y}$, eq. 5.26 takes an easier form

$$\langle \hat{\gamma}(\mathbf{k}) \hat{\gamma}^*(\mathbf{k}') \rangle = \int d^n x e^{i \mathbf{x} \cdot \mathbf{k}} \int d^n y e^{-i (\mathbf{x} + \mathbf{y}) \cdot \mathbf{k}'} C_{\gamma\gamma}(|\mathbf{y}|). \quad (5.27)$$

Collecting all the \mathbf{x} -dependent terms in the first integral, it is recognizable the presence of the Dirac delta function $\delta_D(k) = (2\pi)^{-1} \int dx e^{ixk}$

$$\langle \hat{\gamma}(\mathbf{k}) \hat{\gamma}^*(\mathbf{k}') \rangle = (2\pi)^n \delta_D(\mathbf{k} - \mathbf{k}') \underbrace{\int d^n y e^{-i \mathbf{y} \cdot \mathbf{k}} C_{\gamma\gamma}(|\mathbf{y}|)}_{P_\gamma(|\mathbf{k}|)}, \quad (5.28)$$

where it is highlighted the power spectrum $P_\gamma(|\mathbf{k}|)$.

Equations from 5.25 to 5.28 are just the well known definition of power spectrum i.e. the FT of the two point correlation function. However, our interest is goes into the two-dimensional projection of the homogeneous and isotropic field γ .

- The homogeneity is ensure by the fact that $\gamma(\mathbf{x})$ and $\gamma(\mathbf{x} + \mathbf{y})$ have statistics that cannot be distinguished;
- The isotropy, in an analogous way, is given by the equal statistical properties of $\gamma(\mathbf{x})$ and $\gamma(\mathcal{R}\mathbf{x})$, where \mathcal{R} is a rotational matrix.

Having these assumptions, the link between the three-dimensional field and its projection is given by the Limber equation since it is possible to consider small scales (to other details see [99, 88]). Consider the comoving radial function $f_K(\chi)$ and the DM density perturbation given in eq.3.54. The radial comoving function is [13]

$$f_K(\chi) = \begin{cases} K^{-1/2} \sin(K^{1/2}\chi) & K>0 \\ \chi & K=0 \\ (-K)^{-1/2} \sinh[(-K)^{1/2}\chi] & K<0 \end{cases}, \quad (5.29)$$

with χ the comoving distance and K the curvature parameter. As we saw in the previous chapters, our Universe is almost flat, so in the following treatment it will be used the flat case for the radial comoving function $f_K(\chi) = \chi$.

The density perturbation $\delta(\mathbf{x}, a)$ can be rewritten thanks to a two-dimensional vector $\boldsymbol{\theta}$, which will be identified with the angular position in the sky. The perturbation is now $\delta[\chi\boldsymbol{\theta}, \chi]$ [13]. As illustrated in Fig.5.6, the position of the different elements in the source plane can be identified by specifying χ and the angular position $\boldsymbol{\theta}$.

Let $g_i(\boldsymbol{\theta})$, $i = 1, 2$, the projection of δ along the line-of-sight of the observer at $\chi = 0$, $t = t_0$ [13]

$$g_i(\boldsymbol{\theta}) = \int_0^{\chi_H} d\chi q_i(\chi) \delta[\chi\boldsymbol{\theta}, \chi], \quad (5.30)$$

where q_i is a weight function that will be defined as the lensing efficiency and χ_H the horizon comoving distance.

Being g_i the projection of a homogeneous and isotropic field, it shows the same properties. In analogous to the previous treatment, the correlation function between g_1 and g_2 gives the coefficient C_{12} . This last term can be written in terms of the correlation function between density perturbations thanks to eq.5.30

$$C_{12}(\boldsymbol{\theta}) = \int d\chi q_1(\chi) \int d\chi' q_2(\chi') \langle \delta[\chi\boldsymbol{\theta}, \chi] \delta[\chi'\boldsymbol{\theta}', \chi'] \rangle. \quad (5.31)$$

In order to proceed, some assumptions are required [13]:

- For the Harrison-Pebbles-Zel'dovich power spectrum [84], having k_0 the wavenumber of the perturbation corresponding to the horizon size at Equivalence, the dependence of $P(k)$ on k is linear for $k \ll k_0$. Considering this power spectrum, the first assumption is considering zero power in the fluctuations when the scales that we are considering are larger than a determined coherent scale L_{coh} . Imposing this, the correlation goes to zero for $\Delta\chi = \chi' - \chi \geq L_{coh}$;

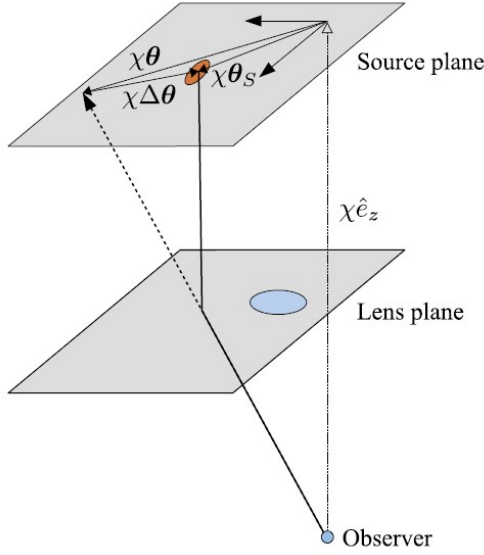


Figure 5.6: Geometry in the Limber approximation. All the position in the source plane can be identified by (θ, χ) with χ being the comoving distance on the line-of-sight and θ the angular position (Figure from [52]).

- δ remain constant in the period of time in which light travels a distance equal to L_{coh} ;
- Taking the difference $\Delta\chi < L_{coh}$, the weight functions are roughly constant over the coherence length and also $\chi \sim \chi'$;
- The regime considered is the small angle approximation, so that the sinusoidal functions can be expanded.

To obtain the Limber projection, eq. 5.31 can be rewritten as 149

$$C_{12}(\boldsymbol{\theta}) = \int_0^\infty d\chi \int_0^\infty d\chi' q_1(\chi) q_2(\chi') C_{\delta\delta}(\hat{\chi}, \bar{\chi}), \quad (5.32)$$

in which are defined the mean comoving distance $\bar{\chi} = (\chi + \chi')/2$ and the distance given by the cosines law $\hat{\chi} = \sqrt{(\chi)^2 + (\chi')^2 - 2\chi\chi' \cos\theta}$.

We now perform a change in variables, considering mean radial comoving distance and the comoving separation between the two galaxies: $\bar{\chi}$ and $\Delta\chi = \chi' - \chi$. In this way, trivially, $\chi = \bar{\chi} - \Delta\chi/2$ and $\chi' = \bar{\chi} + \Delta\chi/2$. Eq. 5.32 becomes

$$C_{12}(\boldsymbol{\theta}) = \int_0^\infty d\bar{\chi} \int_{-\Delta\chi}^{+\Delta\chi} d\Delta\chi q_1\left(\bar{\chi} - \frac{\Delta\chi}{2}\right) q_2\left(\bar{\chi} + \frac{\Delta\chi}{2}\right) C_{\delta\delta}(\hat{\chi}, \bar{\chi}). \quad (5.33)$$

For the third assumption, the product of the weight functions can be approximated with the easier form $q_1(\bar{\chi})q_2(\bar{\chi})$ and being $\chi \sim \chi'$, we can consider $\bar{\chi} = \chi$. Furthermore, for the last hypothesis, $\hat{\chi}$ can be expanded for small angles

$$\begin{aligned} \hat{\chi} &= \sqrt{(\chi)^2 + (\chi')^2 - 2\chi\chi' \cos\theta} \\ &= \sqrt{(2\bar{\chi}^2 + \frac{\Delta\chi^2}{2}) - (2\bar{\chi}^2 - \frac{\Delta\chi^2}{2}) \cos\theta} \\ &= \sqrt{2\bar{\chi}^2(1 - \cos\theta) + \frac{\Delta\chi^2}{2}(1 + \cos\theta)}, \end{aligned} \quad (5.34)$$

and since $\cos\theta \sim 1 - \theta^2/2 + \mathcal{O}(\theta^4)$, it is true that $1 - \cos\theta \sim \theta^2/2$ and $1 + \cos\theta \sim 2$. In this way eq. 5.34 becomes

$$\hat{\chi} = \sqrt{\theta^2 \bar{\chi}^2 + \Delta \chi^2}. \quad (5.35)$$

Using these approximations, the resulting equation is known as the relativistic Limber projection [99] that relates the correlation of the projected and three-dimensional field:

$$C_{12}(\boldsymbol{\theta}) = \int_0^\infty d\chi q_1(\chi) q_2(\chi) \int_0^\infty d\Delta\chi C_{\delta\delta}(\hat{\chi}, \chi), \quad (5.36)$$

where the integral in $d\Delta\chi$ is been expanded imposing that $C_{\delta\delta}$ falls off quickly over the width of $q_{1,2}$.

The final step is to use this Limber projection to obtain the relation between the matter and the weak gravitational shear power spectra. This is possible by inserting into eq. 5.31 the FT of the perturbation δ . While doing this, we highlight the separation between the component of k parallel and perpendicular to the line-of-sight and we still distinguish between χ and χ' [13]

$$C_{12}(\boldsymbol{\theta}) = \int d\chi q_1(\chi) \int d\chi' q_2(\chi') \int \frac{d^3 k}{(2\pi)^3} \int \frac{d^3 k'}{(2\pi)^3} \langle \hat{\delta}(\mathbf{k}, \chi) \hat{\delta}^*(\mathbf{k}', \chi') \rangle \\ \cdot e^{-i\chi \mathbf{k}_\perp \cdot \boldsymbol{\theta}} e^{i\chi' \mathbf{k}'_\perp \cdot \boldsymbol{\theta}'} e^{-ik_3 \chi} e^{ik'_3 \chi'}. \quad (5.37)$$

The correlation function can be replaced by the related power spectrum $\langle \hat{\delta}(\mathbf{k}, \chi) \hat{\delta}^*(\mathbf{k}', \chi') \rangle = (2\pi)^3 \delta_D(\mathbf{k} - \mathbf{k}') P_g(|\mathbf{k}|, \chi)$. Now we use the assumption $q_1(\chi) q_2(\chi)$ and note that the only term in χ' is the exponential term that gives $\int d\chi' e^{ik_3 \chi'} = 2\pi \delta_D(k_3)$. Eq. 5.37 becomes

$$C_{12}(\boldsymbol{\theta}) \int d\chi q_1(\chi) q_2(\chi) \int \frac{d^2 k_\perp}{(2\pi)^2} P_g(|\mathbf{k}_\perp|, \chi) e^{-i\chi \mathbf{k}_\perp \cdot \boldsymbol{\theta}}. \quad (5.38)$$

The final step to obtain the power spectrum is then to consider the integral in eq. 5.28

$$P_\gamma(l) = \int d^2 \boldsymbol{\theta} e^{i\chi \mathbf{k}_\perp \cdot \boldsymbol{\theta}} C_{12}(\boldsymbol{\theta}). \quad (5.39)$$

The integral of the exponential term, considering also the exponential in eq. 5.38 gives another Dirac delta function.

$$P_\gamma(l) = \int d\chi q_1(\chi) q_2(\chi) \int \frac{d^2 k_\perp}{(2\pi)^2} P_g(|\mathbf{k}_\perp|, \chi) \int d^2 \boldsymbol{\theta} e^{-i(\chi \mathbf{k}_\perp - l) \cdot \boldsymbol{\theta}} \\ = \int d\chi \frac{q_1(\chi) q_2(\chi)}{\chi^2} P_g\left(\frac{l}{\chi}, \chi\right). \quad (5.40)$$

The weight functions are defined as the lensing efficiency [86]

$$q_1(\chi) = q_2(\chi) = \frac{3}{2} \frac{H_0^2}{c^2} \Omega_m \frac{\chi}{a(\chi)} \int_\chi^{\chi_H} d\chi' n(\chi') \frac{\chi - \chi'}{\chi'}, \quad (5.41)$$

where $n(\chi)$ is the source-distance distribution of galaxies.

The source-distance distribution in eq. 5.41 can be rewritten in terms of redshift. This new function that we note as $n(z)$ is the redshift distribution of source galaxies and, considering the LSST survey, it can be written [93, 44]

$$n(z) = z^\alpha \exp\left[-\left(\frac{z}{z_0}\right)^\beta\right], \quad (5.42)$$

with the best fit for $\alpha \sim 1.25$, $\beta \sim 1.26$ and $z_0 \sim 1$.

Finally, this distribution can be written in terms of comoving distance instead of redshift thanks to the comoving line-of-sight distance-redshift relation given by [75, 127]

$$\chi = \int_0^z c \frac{dz'}{H(z')}, \quad (5.43)$$

with the Hubble parameter obtained through $H(z) = H_0 E(z)$. The function $E(z)$ is dimensionless Hubble parameter and is given by the following relation.

$$E(z) = \sqrt{\Omega_r(1+z)^4 + \Omega_m(1+z)^3 + \Omega_k(1+z)^2 + \Omega_\Lambda}, \quad (5.44)$$

remembering that in the cosmology considered in this thesis $\Omega_r = \Omega_k = 0$.

5.3.2 The total power spectrum

The shear power spectrum obtained in eq. 5.40 is, however, not sufficient to understand the whole lensing effect because it is only one of the four total parts that need to be taken into account.

Considering eq. 5.24 in its weak limit ($\epsilon = \epsilon^s + \gamma$) it is immediate that the correlator is [86]

$$\langle \epsilon_i \epsilon_j \rangle = \langle \gamma_i \gamma_j \rangle + \langle \epsilon_i^s \epsilon_j^s \rangle + \langle \gamma_i \epsilon_j^s \rangle + \langle \epsilon_i^s \gamma_j \rangle. \quad (5.45)$$

Considering the right-hand side, the first term is the GG correlator that take into account the shear and it is linked to the power spectrum obtained in eq. 5.40 (In order to be consistent, we will refer to $P_\gamma(l)$ as $C_{GG}^{i,j}(l)$). The second term is the II correlator that consider the correlation between galaxies intrinsic ellipticities and the last two terms are the GI correlators for intrinsic-shear alignments. The sum of those four components gives us the final observable power spectrum.

The total angular power spectrum is then [61]

$$C_{tot}(l) = C_{GG}^{i,j}(l) + C_{II}^{i,j}(l) + C_{IG}^{i,j}(l), \quad (5.46)$$

where the power spectra resulting from the II and GI correlators can be written in a form similar to the shear power spectrum in eq. 5.40 considering a modified matter power spectrum.

Referring to the non-linear alignment model (NLA) [31], we introduce the normalization parameter $F(z)$ [72]

$$F(z) = -A_1 C_1 \rho_{crit} \frac{\Omega_m}{D(z)} \left(\frac{1+z}{1+z_0} \right)^\eta \left(\frac{\bar{L}}{L_0} \right)^\beta. \quad (5.47)$$

In the last equation, A_1 is the amplitude of the intrinsic alignment (value of order unity, we will set $A_1 = 1$ [85]), C_1 a fixed value of $5 \cdot 10^{-14} h^{-2} M_\odot^{-1} / \text{Mpc}^3$, ρ_{crit} the critical density at redshift $z = 0$, Ω_m the matter density parameter, $D(z)$ the growth factor, η and β are free parameter that are related respectively to the redshift and luminosity term that can be set both to zero [72], \bar{L} is the mean luminosity of the sample of sources and finally z_0 and L_0 are two reference value of the redshift and luminosity. Having this normalization, it is possible to introduce also the modified matter spectra

$$P_{II}(k, z) = F^2(z) P_{nl}(k, z), \quad (5.48)$$

$$P_{IG}(k, z) = F(z) P_{nl}(k, z). \quad (5.49)$$

Their respective contribution to the total power spectrum is then [61]

$$\begin{aligned} C_{II}^{i,j}(l) &= \int_0^{\chi_H} d\chi \frac{n^i(\chi) n^j(\chi)}{\chi^2} P_{II}\left(\frac{l}{\chi}, \chi\right), \\ C_{IG}^{i,j}(l) &= \int_0^{\chi_H} d\chi \frac{n^i(\chi) q^j(\chi) + n^j(\chi) q^i(\chi)}{\chi^2} P_{IG}\left(\frac{l}{\chi}, \chi\right), \end{aligned} \quad (5.50)$$

where, again, $n(\chi)$ is the galaxies distribution and $q(\chi)$ the lensing efficiency introduced in eq. 5.41.

It is worth to underline the fact that in literature it is possible to find another definition of $C_{IG}^{i,j}(l)$ like in [86] in which

$$C_{IG}^{i,j}(l) = \int_0^{\chi_H} d\chi \frac{n^i(\chi) q^j(\chi)}{\chi^2} P_{IG}\left(\frac{l}{\chi}, \chi\right). \quad (5.51)$$

In order to obtain the plot of the gravitational lensing in eq.5.46 it has been used the python code `PyCosmo` [57] which is a multi-purpose cosmology calculation tool. The code `PyCosmo` can be used to compute several cosmological calculations like the luminosity distance, linear perturbations using a Boltzmann solver, linear and non linear power spectrum and it is useful also to obtain the angular power spectrum of weak lensing

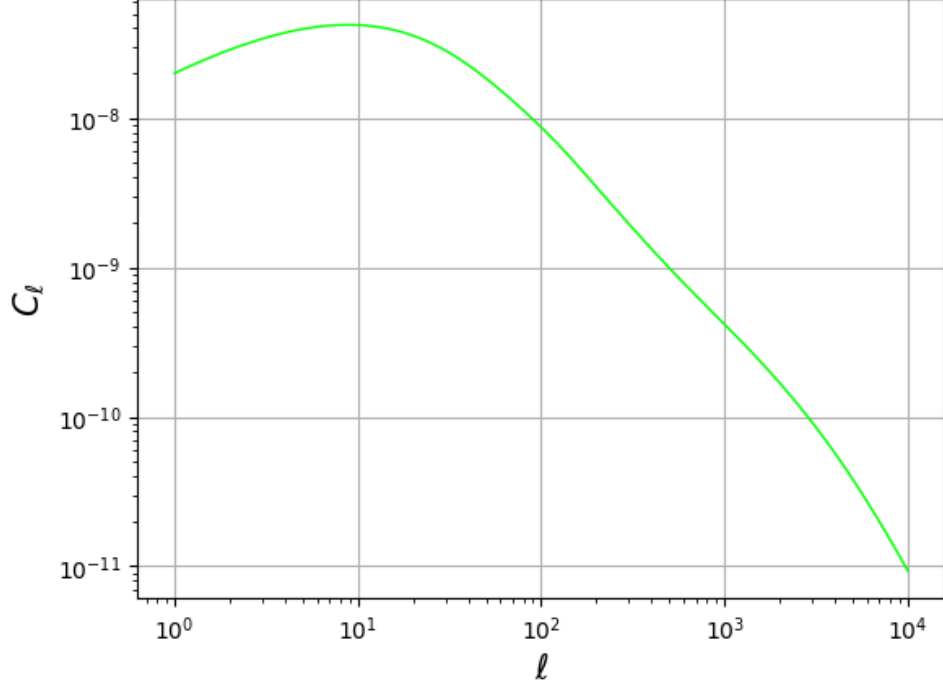


Figure 5.7: Total gravitational lensing angular power spectrum plotted using `PyCosmo`. The equations and the values of the parameter used to plot this curve are all explained in section 5.3.2

Once the angular power spectrum in eq.5.7 is obtained and plotted in Fig.5.7, the final step is to insert the axion fingerprint in the equations. Considering that the axion modifies the matter power spectrum according to eq.3.61, the power spectra P_{II} and P_{IG} are affected by this change too. The three matter power spectra becomes

$$\begin{aligned} P_{nl}^a(k, z) &= T^2(k)P_{nl}(k, z), \\ P_{II}^a(k, z) &= T^2(k)F^2(z)P_{nl}(k, z), \\ P_{IG}^a(k, z) &= T^2(k)F(z)P_{nl}(k, z), \end{aligned} \quad (5.52)$$

where the upper index a stands for axion.

Having these power spectra, also the angular power spectra feels the presence of the axion according to

$$\begin{aligned} C_{GG}^{ij}(l) &= \int d\chi \frac{q^i(\chi)q^j(\chi)}{\chi^2} P_{nl}^a\left(\frac{l}{\chi}, \chi\right), \\ C_{II}^{i,j}(l) &= \int_0^{\chi_H} d\chi \frac{n^i(\chi)n^j(\chi)}{\chi^2} P_{II}^a\left(\frac{l}{\chi}, \chi\right), \\ C_{IG}^{i,j}(l) &= \int_0^{\chi_H} d\chi \frac{n^i(\chi)q^j(\chi) + n^j(\chi)q^i(\chi)}{\chi^2} P_{IG}^a\left(\frac{l}{\chi}, \chi\right). \end{aligned} \quad (5.53)$$

This modified galaxy alignment power spectrum is another important observable useful to put additional constraints on the mass of the axion and, in order to plot it, one possibility is to modify

PyCosmo by inserting the axion transfer function in eq.3.62 inside the sub-function that compute the non-linear matter power spectrum.

Chapter 6

Conclusions

After an illustration of the concordance model of cosmology and a detailed discussion on the reason that leads to the introduction of DM, we show the reason why CDM is not completely exhaustive in explaining the observation at small scales since it cannot solve issues such as the Missing Satellite Problem or the Core-Cusp Problem. For this reason we decided to introduce a DM alternative whose particle is identified by an ultralight scalar field ϕ . In this thesis we studied FDM, how it behaves and how it changes some phenomena that we have studied in the CDM scenario.

The scalar field which form the FDM coincides with the cosmological axion and because of its extremely small mass that in this thesis we assume of the order of 10^{-22} eV it shows a quantum non-negligible behavior. When masses so small are considered, the DM is called Fuzzy and the quantum nature of the field arise in the quantum pressure term in eq.[3.53](#)

During the collapse of the DM halo, the competition between the inward gravity and the outward quantum pressure determines a critical scale, the Jeans scale [3.57](#) which determines the boundary between the formation of a galaxy or not.

In this thesis we were looking for some observables through which it is possible to verify the possible existence of axions as a source of DM. We identify two possible observables, the matter and galaxy alignment power spectra.

When axion are taken into account through the transfer function in eq.[3.62](#), the matter power spectrum changes and the big amount of dwarf galaxies expected in the CDM scenario are no longer present since the axion matter power spectrum predicts a cut off at large values of k , i.e. small scales, as clearly observable in Fig.[5.2](#) while in Fig.[3.4](#) we can find a comparison between the Universe born from a CDM scenario and the same considering FDM. In this last plot it is also possible to see the lack of small galaxies in the FDM scenario w.r.t the CDM case.

Without being solely focused on the existence of a single type of axion, we consider for a quick treatment also the case in which the axion shows a mass range that cover over 20 orders of magnitude with each one bringing its own contribution to the matter density parameter Ω_m . In particular, we consider the cases where the mass makes it possible to treat axions as DM (above 10^{-25} eV) and as DE (below 10^{-30} eV). Using BOSS and Planck data from 2015 and 2018, the result is that, even if we consider axion also as DE source, its major contribution goes into the DM sector since for $m_a < 10^{-26}$ eV the contribution is about the 10% of the total current DM amount and this can be seen in Fig.[3.11](#).

Because FDM modifies dramatically the Λ CDM situation at small scales, we consider relevant to studied how the star formation changes when the DM particle is the axion. The Core-Cusp Problem suggests that the NFW profile is not consistent with the observation of the density profile because it seems like the density profile of galaxies tends to form a core rather than the cusp predicted by CDM. FDM, as it can be seen in Fig.[3.21](#), is more consistent with the reality of the profile and of course this has consequences on the formation of the first objects in the Universe.

In this thesis it is also studying very quickly how to detect the presence of an axion cloud around a compact object and a binary system. The phenomenon of superradiance can happen when the condition in eq.[4.10](#) is satisfied and it reaches its maximum efficiency when the gravitational coupling constant $\alpha_G \sim 0.5$. However, the consequences when a single BH is involved are too small to be detected. For this reason, it is more convenient to study binary systems, since they can

ionize the axions cloud in the surroundings that behave like an hydrogen atom. The comparison between the power of ionization P_{ION} and the power emitted by the GW P_{GW} shows fingerprint effects and the frequency of the GW can be used to put constraints on the axion mass.

The second principal way in which this thesis deals with the problem of putting constraints on the mass of the axion is the galaxy alignment. The most common way to model a galaxy shape is an ellipsoid, and these geometrical figures can be aligned toward a common direction when they are projected into a two-dimensional surface. This can be due to an intrinsic effect called "intrinsic alignment" through which galaxies are actually tilted all in the same direction due to an external force, or due an extrinsic optic effect known as "gravitational lensing". The lenses are conglomerate of matter (baryonic or not) that perturb the local space-time bending the trajectories of photons. In this way we can observe objects which would normally be obscured by other bodies.

The lensing effect is described at small scales using the Limber approximation that leads to P_γ in eq.5.40. However, as mentioned above, this term is not sufficient to understand the whole lensing effect because there can be some intrinsic force or phenomenon that cause galaxies under its influence to point toward the same direction. Indeed, in the weak lensing limit ($|\gamma|, \kappa \ll 1$), the ellipticity that we observe expressed in eq.5.24 shows two terms, the intrinsic ellipticity ϵ^s and the shear γ . The correlator of ϵ then will have a term due to the shear $\langle \gamma\gamma \rangle$, one due to the intrinsic $\langle \epsilon^s \epsilon^s \rangle$ and a cross term $\langle \epsilon^s \gamma \rangle + \langle \gamma \epsilon^s \rangle$. All of this terms give rise to an angular power spectrum (see eq.5.40 5.50), with the last two terms involving a modified version of the matter power spectrum. By inserting the axion transfer function into the matter power spectrum used to compute all the terms in eq.5.7, we could be able to compare the theoretical results and the observation to find additional constraints on the mass of the axion and verify if the wave DM could be a better proposal than CDM to explain why the Universe looks like the way we observe it.

Bibliography

- [1] Tom Abel, Greg L. Bryan, and Michael L. Norman. “The Formation of the First Star in the Universe”. In: *Science* 295.5552 (Jan. 2002), pp. 93–98. DOI: [10.1126/science.1063991](https://doi.org/10.1126/science.1063991). URL: <https://doi.org/10.1126/science.1063991>
- [2] Simone Aiola et al. “The Atacama Cosmology Telescope: DR4 maps and cosmological parameters”. In: *Journal of Cosmology and Astroparticle Physics* 2020.12 (Dec. 2020), pp. 047–047. DOI: [10.1088/1475-7516/2020/12/047](https://doi.org/10.1088/1475-7516/2020/12/047). URL: <https://doi.org/10.1088/1475-7516/2020/12/047>
- [3] S. M. Khairul Alam, James S. Bullock, and David H. Weinberg. *Dark Matter Properties and Halo Central Densities*. 2001. DOI: [10.48550/ARXIV.ASTRO-PH/0109392](https://arxiv.org/abs/astro-ph/0109392). URL: <https://arxiv.org/abs/astro-ph/0109392>
- [4] Shadab Alam et al. “The clustering of galaxies in the completed SDSS-III Baryon Oscillation Spectroscopic Survey: cosmological analysis of the DR12 galaxy sample”. In: *Monthly Notices of the Royal Astronomical Society* 470.3 (Mar. 2017), pp. 2617–2652. DOI: [10.1093/mnras/stx721](https://doi.org/10.1093/mnras/stx721). URL: <https://doi.org/10.1093/mnras/stx721>
- [5] Anthony Challinor Antony Lewis. URL: <https://camb.info/>.
- [6] Asimina Arvanitaki, Masha Baryakhtar, and Xinlu Huang. “Discovering the QCD axion with black holes and gravitational waves”. In: *Physical Review D* 91.8 (Apr. 2015). DOI: [10.1103/physrevd.91.084011](https://doi.org/10.1103/physrevd.91.084011). URL: <https://doi.org/10.1103/physrevd.91.084011>
- [7] Asimina Arvanitaki and Sergei Dubovsky. “Exploring the string axiverse with precision black hole physics”. In: *Physical Review D* 83.4 (Feb. 2011). DOI: [10.1103/physrevd.83.044026](https://doi.org/10.1103/physrevd.83.044026). URL: <https://doi.org/10.1103/physrevd.83.044026>
- [8] Asimina Arvanitaki et al. “String axiverse”. In: *Physical Review D* 81.12 (June 2010). DOI: [10.1103/physrevd.81.123530](https://doi.org/10.1103/physrevd.81.123530). URL: <https://doi.org/10.1103/physrevd.81.123530>
- [9] C. A. Baker et al. “Improved Experimental Limit on the Electric Dipole Moment of the Neutron”. In: *Physical Review Letters* 97.13 (Sept. 2006). DOI: [10.1103/physrevlett.97.131801](https://doi.org/10.1103/physrevlett.97.131801). URL: <https://doi.org/10.1103/physrevlett.97.131801>
- [10] J. M. Bardeen et al. “The Statistics of Peaks of Gaussian Random Fields”. In: 304 (May 1986), p. 15. DOI: [10.1086/164143](https://doi.org/10.1086/164143).
- [11] Joshua Barnes and George Efstathiou. “Angular Momentum from Tidal Torques”. In: 319 (Aug. 1987), p. 575. DOI: [10.1086/165480](https://doi.org/10.1086/165480).
- [12] Matthias Bartelmann. “Gravitational lensing”. In: *Classical and Quantum Gravity* 27.23 (Nov. 2010), p. 233001. DOI: [10.1088/0264-9381/27/23/233001](https://doi.org/10.1088/0264-9381/27/23/233001). URL: <https://doi.org/10.1088/0264-9381/27/23/233001>
- [13] Matthias Bartelmann and Peter Schneider. “Weak gravitational lensing”. In: *Physics Reports* 340.4-5 (Jan. 2001), pp. 291–472. DOI: [10.1016/s0370-1573\(00\)00082-x](https://doi.org/10.1016/s0370-1573(00)00082-x). URL: [https://doi.org/10.1016/s0370-1573\(00\)00082-x](https://doi.org/10.1016/s0370-1573(00)00082-x)
- [14] Jurek B Bauer et al. “Intensity mapping as a probe of axion dark matter”. In: *Monthly Notices of the Royal Astronomical Society* 500.3 (Oct. 2020), pp. 3162–3177. DOI: [10.1093/mnras/staa3300](https://doi.org/10.1093/mnras/staa3300). URL: <https://doi.org/10.1093/mnras/staa3300>

- [15] Daniel Baumann. "Cosmological Inflation: Theory and Observations". In: *Advanced Science Letters* 2.2 (June 2009), pp. 105–120. DOI: [10.1166/asl.2009.1019](https://doi.org/10.1166/asl.2009.1019). URL: <https://doi.org/10.1166%2Fasl.2009.1019>.
- [16] Daniel Baumann, Horng Sheng Chia, and Rafael A. Porto. "Probing ultralight bosons with binary black holes". In: *Physical Review D* 99.4 (Feb. 2019). DOI: [10.1103/physrevd.99.044001](https://doi.org/10.1103/physrevd.99.044001). URL: <https://doi.org/10.1103%2Fphysrevd.99.044001>.
- [17] Daniel Baumann et al. "Gravitational collider physics". In: *Physical Review D* 101.8 (Apr. 2020). DOI: [10.1103/physrevd.101.083019](https://doi.org/10.1103/physrevd.101.083019). URL: <https://doi.org/10.1103%2Fphysrevd.101.083019>.
- [18] Daniel Baumann et al. "Ionization of gravitational atoms". In: *Physical Review D* 105.11 (June 2022). DOI: [10.1103/physrevd.105.115036](https://doi.org/10.1103/physrevd.105.115036). URL: <https://doi.org/10.1103%2Fphysrevd.105.115036>.
- [19] Daniel Baumann et al. "Sharp Signals of Boson Clouds in Black Hole Binary Inspirals". In: *Physical Review Letters* 128.22 (June 2022). DOI: [10.1103/physrevlett.128.221102](https://doi.org/10.1103/physrevlett.128.221102). URL: <https://doi.org/10.1103%2Fphysrevlett.128.221102>.
- [20] Daniel Baumann et al. "The spectra of gravitational atoms". In: *Journal of Cosmology and Astroparticle Physics* 2019.12 (Dec. 2019), pp. 006–006. DOI: [10.1088/1475-7516/2019/12/006](https://doi.org/10.1088/1475-7516/2019/12/006). URL: <https://doi.org/10.1088%2F1475-7516%2F2019%2F12%2F006>.
- [21] K. G. Begeman, A. H. Broeils, and R. H. Sanders. "Extended rotation curves of spiral galaxies : dark haloes and modified dynamics." In: 249 (Apr. 1991), p. 523. DOI: [10.1093/mnras/249.3.523](https://doi.org/10.1093/mnras/249.3.523).
- [22] M. Betoule et al. "Improved cosmological constraints from a joint analysis of the SDSS-II and SNLS supernova samples". In: *Astronomy & Astrophysics* 568 (Aug. 2014), A22. DOI: [10.1051/0004-6361/201423413](https://doi.org/10.1051/0004-6361/201423413). URL: <https://doi.org/10.1051%2F0004-6361%2F201423413>.
- [23] Philip Bett et al. "The spin and shape of dark matter haloes in the Millennium simulation of a Λ cold dark matter universe". In: *Monthly Notices of the Royal Astronomical Society* 376.1 (Mar. 2007), pp. 215–232. DOI: [10.1111/j.1365-2966.2007.11432.x](https://doi.org/10.1111/j.1365-2966.2007.11432.x). URL: <https://doi.org/10.1111%2Fj.1365-2966.2007.11432.x>.
- [24] Florian Beutler et al. "The 6dF Galaxy Survey: baryon acoustic oscillations and the local Hubble constant". In: *Monthly Notices of the Royal Astronomical Society* 416.4 (July 2011), pp. 3017–3032. DOI: [10.1111/j.1365-2966.2011.19250.x](https://doi.org/10.1111/j.1365-2966.2011.19250.x). URL: <https://doi.org/10.1111%2Fj.1365-2966.2011.19250.x>.
- [25] Horst R. Beyer. "On the Stability of the Kerr Metric". In: *Communications in Mathematical Physics* 221.3 (Aug. 2001), pp. 659–676. DOI: [10.1007/s002200100494](https://doi.org/10.1007/s002200100494). URL: <https://doi.org/10.1007%2Fs002200100494>.
- [26] Horst Reinhard Beyer. "On the stability of the massive scalar field in Kerr space-time". In: *Journal of Mathematical Physics* 52.10 (Oct. 2011), p. 102502. DOI: [10.1063/1.3653840](https://doi.org/10.1063/1.3653840). URL: <https://doi.org/10.1063%2F1.3653840>.
- [27] M Birkinshaw. "The Sunyaev-Zel'dovich effect". In: *Physics Reports* 310.2-3 (Mar. 1999), pp. 97–195. DOI: [10.1016/s0370-1573\(98\)00080-5](https://doi.org/10.1016/s0370-1573(98)00080-5). URL: <https://doi.org/10.1016%2Fs0370-1573%2898%2900080-5>.
- [28] Michael Blanton and the Sloan Digital Sky Survey. URL: https://www.sdss3.org/science/gallery_sdss_pie2.php.
- [29] W. J. G. de Blok. "The Core-Cusp Problem". In: *Advances in Astronomy* 2010 (2010), pp. 1–14. DOI: [10.1155/2010/789293](https://doi.org/10.1155/2010/789293). URL: <https://doi.org/10.1155%2F2010%2F789293>.
- [30] G. R. Blumenthal et al. "Contraction of Dark Matter Galactic Halos Due to Baryonic Infall". In: 301 (Feb. 1986), p. 27. DOI: [10.1086/163867](https://doi.org/10.1086/163867).
- [31] Sarah Bridle and Lindsay King. "Dark energy constraints from cosmic shear power spectra: impact of intrinsic alignments on photometric redshift requirements". In: *New Journal of Physics* 9.12 (Dec. 2007), pp. 444–444. DOI: [10.1088/1367-2630/9/12/444](https://doi.org/10.1088/1367-2630/9/12/444). URL: <https://doi.org/10.1088%2F1367-2630%2F9%2F12%2F444>.

- [32] F. Brimiouille et al. “Dark matter halo properties from galaxy–galaxy lensing72”. In: *Monthly Notices of the Royal Astronomical Society* 432.2 (May 2013), pp. 1046–1102. DOI: [10.1093/mnras/stt525](https://doi.org/10.1093/mnras/stt525). URL: <https://doi.org/10.1093/mnras/stt525>.
- [33] Thejs Brinckmann et al. “Zeldovich pancakes in observational data are cold”. In: *Journal of Cosmology and Astroparticle Physics* 2016.04 (Apr. 2016), pp. 007–007. DOI: [10.1088/1475-7516/2016/04/007](https://doi.org/10.1088/1475-7516/2016/04/007). URL: <https://doi.org/10.1088/1475-7516/2016/04/007>.
- [34] Richard Brito, Vitor Cardoso, and Paolo Pani. *Superradiance*. Springer International Publishing, 2020. DOI: [10.1007/978-3-030-46622-0](https://doi.org/10.1007/978-3-030-46622-0). URL: <https://doi.org/10.1007/978-3-030-46622-0>.
- [35] Greg L. Bryan et al. “ENZO: AN ADAPTIVE MESH REFINEMENT CODE FOR ASTROPHYSICS”. In: *The Astrophysical Journal Supplement Series* 211.2 (Mar. 2014), p. 19. DOI: [10.1088/0067-0049/211/2/19](https://doi.org/10.1088/0067-0049/211/2/19). URL: <https://doi.org/10.1088/0067-0049/211/2/19>.
- [36] James S. Bullock. *Notes on the Missing Satellites Problem*. 2010. DOI: [10.48550/ARXIV.1009.4505](https://arxiv.org/abs/1009.4505). URL: <https://arxiv.org/abs/1009.4505>.
- [37] James S. Bullock, Andrey V. Kravtsov, and David H. Weinberg. “Hierarchical Galaxy Formation and Substructure in the Galaxy’s Stellar Halo”. In: *The Astrophysical Journal* 548.1 (Feb. 2001), pp. 33–46. DOI: [10.1086/318681](https://doi.org/10.1086/318681). URL: <https://doi.org/10.1086/318681>.
- [38] A. Burkert. “The Structure of Dark Matter Halos in Dwarf Galaxies”. In: *The Astrophysical Journal* 447.1 (July 1995). DOI: [10.1086/309560](https://doi.org/10.1086/309560). URL: <https://doi.org/10.1086/309560>.
- [39] Erminia Calabrese and David N. Spergel. “Ultra-light dark matter in ultra-faint dwarf galaxies”. In: *Monthly Notices of the Royal Astronomical Society* 460.4 (May 2016), pp. 4397–4402. ISSN: 0035-8711. DOI: [10.1093/mnras/stw1256](https://doi.org/10.1093/mnras/stw1256). eprint: <https://academic.oup.com/mnras/article-pdf/460/4/4397/8117919/stw1256.pdf>. URL: <https://doi.org/10.1093/mnras/stw1256>.
- [40] Vitor Cardoso. “Black hole bombs and explosions: from astrophysics to particle physics”. In: *General Relativity and Gravitation* 45.11 (Aug. 2013), pp. 2079–2097. DOI: [10.1007/s10714-013-1584-z](https://doi.org/10.1007/s10714-013-1584-z). URL: <https://doi.org/10.1007/s10714-013-1584-z>.
- [41] Vitor Cardoso et al. “Black-hole bomb and superradiant instabilities”. In: *Phys. Rev. D* 70 (4 Aug. 2004), p. 044039. DOI: [10.1103/PhysRevD.70.044039](https://doi.org/10.1103/PhysRevD.70.044039). URL: <https://link.aps.org/doi/10.1103/PhysRevD.70.044039>.
- [42] S. Carlip. “Black hole thermodynamics”. In: *International Journal of Modern Physics D* 23.11 (Oct. 2014), p. 1430023. DOI: [10.1142/s0218271814300237](https://doi.org/10.1142/s0218271814300237). URL: <https://doi.org/10.1142/s0218271814300237>.
- [43] Sean M. Carroll, William H. Press, and Edwin L. Turner. “The cosmological constant.” In: 30 (Jan. 1992), pp. 499–542. DOI: [10.1146/annurev.aa.30.090192.002435](https://doi.org/10.1146/annurev.aa.30.090192.002435).
- [44] C. Chang et al. “The effective number density of galaxies for weak lensing measurements in the LSST project”. In: *Monthly Notices of the Royal Astronomical Society* 434.3 (July 2013), pp. 2121–2135. ISSN: 0035-8711. DOI: [10.1093/mnras/stt1156](https://doi.org/10.1093/mnras/stt1156). eprint: <https://academic.oup.com/mnras/article-pdf/434/3/2121/18496619/stt1156.pdf>. URL: <https://doi.org/10.1093/mnras/stt1156>.
- [45] James M. Cline. *Baryogenesis*. 2006. DOI: [10.48550/ARXIV.HEP-PH/0609145](https://arxiv.org/abs/hep-ph/0609145). URL: <https://arxiv.org/abs/hep-ph/0609145>.
- [46] R. Courant, K. Friedrichs, and H. Lewy. “Über die partiellen Differenzengleichungen der mathematischen Physik”. In: *Mathematische Annalen* 100 (Jan. 1928), pp. 32–74. DOI: [10.1007/BF01448839](https://doi.org/10.1007/BF01448839).
- [47] Francesco D’Eramo, Nicolas Fernandez, and Stefano Profumo. “Dark Matter Freeze-in Production in Fast-Expanding Universes”. In: *Journal of Cosmology and Astroparticle Physics* 2018.02 (Feb. 2018), pp. 046–046. DOI: [10.1088/1475-7516/2018/02/046](https://doi.org/10.1088/1475-7516/2018/02/046). URL: <https://doi.org/10.1088/1475-7516/2018/02/046>.

- [48] Kyle S. Dawson et al. “THE BARYON OSCILLATION SPECTROSCOPIC SURVEY OF SDSS-III”. In: *The Astronomical Journal* 145.1 (Dec. 2012), p. 10. DOI: [10.1088/0004-6256/145/1/10](https://doi.org/10.1088/0004-6256/145/1/10). URL: <https://doi.org/10.1088%2F0004-6256%2F145%2F1%2F10>.
- [49] Antonino Del Popolo. *L’Universo Invisibile*. WriteUp Books, 2021.
- [50] Vincent Desjacques, Alex Kehagias, and Antonio Riotto. “Impact of ultralight axion self-interactions on the large scale structure of the Universe”. In: *Physical Review D* 97.2 (Jan. 2018). DOI: [10.1103/physrevd.97.023529](https://doi.org/10.1103/physrevd.97.023529). URL: <https://doi.org/10.1103%2Fphysrevd.97.023529>.
- [51] Steven Detweiler. “Klein-Gordon equation and rotating black holes”. In: 22.10 (Nov. 1980), pp. 2323–2326. DOI: [10.1103/PhysRevD.22.2323](https://doi.org/10.1103/PhysRevD.22.2323).
- [52] Scott Dodelson. *Modern Cosmology*. Academic Press, Elsevier Science, 2003.
- [53] Sam R. Dolan. “Instability of the massive Klein-Gordon field on the Kerr spacetime”. In: *Physical Review D* 76.8 (Oct. 2007). DOI: [10.1103/physrevd.76.084001](https://doi.org/10.1103/physrevd.76.084001). URL: <https://doi.org/10.1103%2Fphysrevd.76.084001>.
- [54] Sam R. Dolan. “Superradiant instabilities of rotating black holes in the time domain”. In: *Physical Review D* 87.12 (June 2013). DOI: [10.1103/physrevd.87.124026](https://doi.org/10.1103/physrevd.87.124026). URL: <https://doi.org/10.1103%2Fphysrevd.87.124026>.
- [55] Yong Du et al. “Revisiting dark matter freeze-in and freeze-out through phase-space distribution”. In: *Journal of Cosmology and Astroparticle Physics* 2022.04 (Apr. 2022), p. 012. DOI: [10.1088/1475-7516/2022/04/012](https://doi.org/10.1088/1475-7516/2022/04/012). URL: <https://doi.org/10.1088%2F1475-7516%2F2022%2F04%2F012>.
- [56] Judy Schmidt ESA/Hubble NASA. URL: <https://www.nasa.gov/image-feature/goddard/2018/hubble-finds-an-einstein-ring>.
- [57] Institute of Particle Physics ETH Zurich and Astrophysics. URL: <https://cosmo-docs.phys.ethz.ch/PyCosmo/index.html>.
- [58] F. Feroz, M. P. Hobson, and M. Bridges. “MultiNest: an efficient and robust Bayesian inference tool for cosmology and particle physics”. In: *Monthly Notices of the Royal Astronomical Society* 398.4 (Oct. 2009), pp. 1601–1614. DOI: [10.1111/j.1365-2966.2009.14548.x](https://doi.org/10.1111/j.1365-2966.2009.14548.x). URL: <https://doi.org/10.1111%2Fj.1365-2966.2009.14548.x>.
- [59] Richard Feynman, Robert B. Leighton, and Matthew L. Sands. *The Feynman Lectures on Physics*. 3 volumes. Addison-Wesley, 1963.
- [60] Giuseppe Ficarra. *Scalar field dynamics around black holes: superradiant instabilities and binary evolution*. 2021. DOI: [10.48550/ARXIV.2105.05918](https://arxiv.org/abs/2105.05918). URL: <https://arxiv.org/abs/2105.05918>.
- [61] Silvan Fischbacher et al. “Redshift requirements for cosmic shear with intrinsic alignment”. In: *Journal of Cosmology and Astroparticle Physics* 2023.01 (Jan. 2023), p. 033. DOI: [10.1088/1475-7516/2023/01/033](https://doi.org/10.1088/1475-7516/2023/01/033). URL: <https://doi.org/10.1088%2F1475-7516%2F2023%2F01%2F033>.
- [62] D. J. Fixsen et al. “The Cosmic Microwave Background Spectrum from the FullCOBE/iFIRAS Data Set”. In: *The Astrophysical Journal* 473.2 (Dec. 1996), pp. 576–587. DOI: [10.1086/178173](https://doi.org/10.1086/178173). URL: <https://doi.org/10.1086%2F178173>.
- [63] Liang Gao and Tom Theuns. “Lighting the Universe with Filaments”. In: *Science* 317.5844 (Sept. 2007), pp. 1527–1530. DOI: [10.1126/science.1146676](https://doi.org/10.1126/science.1146676). URL: <https://doi.org/10.1126%2Fscience.1146676>.
- [64] Howard Georgi and S. L. Glashow. “Unity of All Elementary-Particle Forces”. In: *Phys. Rev. Lett.* 32 (8 Feb. 1974), pp. 438–441. DOI: [10.1103/PhysRevLett.32.438](https://doi.org/10.1103/PhysRevLett.32.438). URL: <https://link.aps.org/doi/10.1103/PhysRevLett.32.438>.
- [65] J. Alberto Vazquez Gonzalez, Luis E. Padilla, and Tonatiuh Matos. “Inflationary cosmology: from theory to observations”. In: *Revista Mexicana de Fisica E* 17.1 Jan-Jun (Jan. 2020), pp. 73–91. DOI: [10.31349/revmexfise.17.73](https://doi.org/10.31349/revmexfise.17.73). URL: <https://doi.org/10.31349%2Frevmexfise.17.73>.

- [66] Christopher Gordon. *Adiabatic and entropy perturbations in cosmology*. 2001. DOI: [10.48550/ARXIV.ARTO-PH/0112523](https://doi.org/10.48550/ARXIV.ARTO-PH/0112523). URL: <https://arxiv.org/abs/astro-ph/0112523>.
- [67] D. O. Gough. “An elementary introduction to the JWKB approximation”. In: *Astronomische Nachrichten* 328.3-4 (Mar. 2007), pp. 273–285. DOI: [10.1002/asna.200610730](https://doi.org/10.1002/asna.200610730). URL: <https://doi.org/10.1002%2Fasna.200610730>.
- [68] Alan H. Guth. “Inflationary universe: A possible solution to the horizon and flatness problems”. In: *Phys. Rev. D* 23 (2 Jan. 1981), pp. 347–356. DOI: [10.1103/PhysRevD.23.347](https://doi.org/10.1103/PhysRevD.23.347). URL: <https://link.aps.org/doi/10.1103/PhysRevD.23.347>.
- [69] Oliver Hahn and Tom Abel. *MUSIC: Multi-Scale Initial Conditions*. Astrophysics Source Code Library, record ascl:1311.011. Nov. 2013. ascl: [1311.011](https://doi.org/10.1311/011).
- [70] A. J. S. Hamilton et al. “Reconstructing the Primordial Spectrum of Fluctuations of the Universe from the Observed Nonlinear Clustering of Galaxies”. In: 374 (June 1991), p. L1. DOI: [10.1086/186057](https://doi.org/10.1086/186057).
- [71] Nathan Herring et al. “Particle decay in post inflationary cosmology”. In: *Physical Review D* 98.8 (Oct. 2018). DOI: [10.1103/physrevd.98.083503](https://doi.org/10.1103/physrevd.98.083503). URL: <https://doi.org/10.1103%2Fphysrevd.98.083503>.
- [72] H. Hildebrandt et al. “KiDS-450: cosmological parameter constraints from tomographic weak gravitational lensing”. In: *Monthly Notices of the Royal Astronomical Society* 465.2 (Nov. 2016), pp. 1454–1498. DOI: [10.1093/mnras/stw2805](https://doi.org/10.1093/mnras/stw2805). URL: <https://doi.org/10.1093%2Fmnras%2Fstw2805>.
- [73] Renée Hlozek et al. “A search for ultralight axions using precision cosmological data”. In: *Physical Review D* 91.10 (May 2015). DOI: [10.1103/physrevd.91.103512](https://doi.org/10.1103/physrevd.91.103512). URL: <https://doi.org/10.1103%2Fphysrevd.91.103512>.
- [74] Craig J. Hogan and Julianne J. Dalcanton. “New dark matter physics: Clues from halo structure”. In: *Physical Review D* 62.6 (Aug. 2000). DOI: [10.1103/physrevd.62.063511](https://doi.org/10.1103/physrevd.62.063511). URL: <https://doi.org/10.1103%2Fphysrevd.62.063511>.
- [75] David W. Hogg. *Distance measures in cosmology*. 2000. arXiv: [astro-ph/9905116 \[astro-ph\]](https://arxiv.org/abs/astro-ph/9905116).
- [76] Wayne Hu, Rennan Barkana, and Andrei Gruzinov. “Fuzzy Cold Dark Matter: The Wave Properties of Ultralight Particles”. In: *Physical Review Letters* 85.6 (Aug. 2000), pp. 1158–1161. DOI: [10.1103/physrevlett.85.1158](https://doi.org/10.1103/physrevlett.85.1158). URL: <https://doi.org/10.1103%2Fphysrevlett.85.1158>.
- [77] Edwin Hubble. “A Relation between Distance and Radial Velocity among Extra-Galactic Nebulae”. In: *Proceedings of the National Academy of Science* 15.3 (Mar. 1929), pp. 168–173. DOI: [10.1073/pnas.15.3.168](https://doi.org/10.1073/pnas.15.3.168).
- [78] Lam Hui. “Wave Dark Matter”. In: *Annual Review of Astronomy and Astrophysics* 59.1 (Sept. 2021), pp. 247–289. DOI: [10.1146/annurev-astro-120920-010024](https://doi.org/10.1146/annurev-astro-120920-010024). URL: <https://doi.org/10.1146%2Fannurev-astro-120920-010024>.
- [79] Lam Hui et al. “Ultralight scalars as cosmological dark matter”. In: *Physical Review D* 95.4 (Feb. 2017). DOI: [10.1103/physrevd.95.043541](https://doi.org/10.1103/physrevd.95.043541). URL: <https://doi.org/10.1103%2Fphysrevd.95.043541>.
- [80] Mikhail M. Ivanov. *Effective Field Theory for Large Scale Structure*. 2022. DOI: [10.48550/ARXIV.2212.08488](https://doi.org/10.48550/ARXIV.2212.08488). URL: <https://arxiv.org/abs/2212.08488>.
- [81] Mikhail M. Ivanov, Marko Simonović, and Matias Zaldarriaga. “Cosmological parameters from the BOSS galaxy power spectrum”. In: *Journal of Cosmology and Astroparticle Physics* 2020.05 (May 2020), pp. 042–042. DOI: [10.1088/1475-7516/2020/05/042](https://doi.org/10.1088/1475-7516/2020/05/042). URL: <https://doi.org/10.1088%2F1475-7516%2F2020%2F05%2F042>.
- [82] B. Jain, H. J. Mo, and S. D. M. White. “The evolution of correlation functions and power spectra in gravitational clustering”. In: *Monthly Notices of the Royal Astronomical Society* 276.1 (Sept. 1995), pp. L25–L29. ISSN: 0035-8711. DOI: [10.1093/mnras/276.1.L25](https://doi.org/10.1093/mnras/276.1.L25). eprint: <https://academic.oup.com/mnras/article-pdf/276/1/L25/2972243/mnras276-0L25.pdf>. URL: <https://doi.org/10.1093/mnras/276.1.L25>.

- [83] A. Jenkins et al. “The mass function of dark matter haloes”. In: 321.2 (Feb. 2001), pp. 372–384. DOI: [10.1046/j.1365-8711.2001.04029.x](https://doi.org/10.1046/j.1365-8711.2001.04029.x). arXiv: [astro-ph/0005260](https://arxiv.org/abs/astro-ph/0005260) [astro-ph].
- [84] Jun-Qian Jiang, Gen Ye, and Yun-Song Piao. *Return of Harrison-Zeldovich spectrum in light of recent cosmological tensions*. 2022. arXiv: [2210.06125](https://arxiv.org/abs/2210.06125) [astro-ph.CO].
- [85] B. Joachimi et al. “Constraints on intrinsic alignment contamination of weak lensing surveys using the MegaZ-LRG sample”. In: *Astronomy & Astrophysics* 527 (Jan. 2011), A26. DOI: [10.1051/0004-6361/201015621](https://doi.org/10.1051/0004-6361/201015621). URL: <https://doi.org/10.1051%2F0004-6361%2F201015621>.
- [86] Benjamin Joachimi et al. “Galaxy Alignments: An Overview”. In: *Space Science Reviews* 193.1-4 (July 2015), pp. 1–65. DOI: [10.1007/s11214-015-0177-4](https://doi.org/10.1007/s11214-015-0177-4). URL: <https://doi.org/10.1007%2Fs11214-015-0177-4>.
- [87] Nick Kaiser. “Clustering in real space and in redshift space”. In: *Monthly Notices of the Royal Astronomical Society* 227.1 (July 1987), pp. 1–21. ISSN: 0035-8711. DOI: [10.1093/mnras/227.1.1](https://doi.org/10.1093/mnras/227.1.1). eprint: <https://academic.oup.com/mnras/article-pdf/227/1/1/18522208/mnras227-0001.pdf>. URL: <https://doi.org/10.1093/mnras/227.1.1>.
- [88] Nick Kaiser. “Weak Gravitational Lensing of Distant Galaxies”. In: 388 (Apr. 1992), p. 272. DOI: [10.1086/171151](https://doi.org/10.1086/171151).
- [89] Marc Kamionkowski. *Possible Relics from New Physics in the Early Universe: Inflation, the Cosmic Microwave Background, and Particle Dark Matter*. 1998. DOI: [10.48550/ARXIV.ASTRO-PH/9809214](https://arxiv.org/abs/astro-ph/9809214). URL: <https://arxiv.org/abs/astro-ph/9809214>.
- [90] Marc Kamionkowski and Andrew R. Liddle. “The Dearth of Halo Dwarf Galaxies: Is There Power on Short Scales?” In: *Physical Review Letters* 84.20 (May 2000), pp. 4525–4528. DOI: [10.1103/physrevlett.84.4525](https://doi.org/10.1103/physrevlett.84.4525). URL: <https://doi.org/10.1103%2Fphysrevlett.84.4525>.
- [91] I. G. Kaplan. *Pauli Exclusion Principle and its theoretical foundation*. 2019. DOI: [10.48550/ARXIV.1902.00499](https://arxiv.org/abs/1902.00499). URL: <https://arxiv.org/abs/1902.00499>.
- [92] Darsh Kodwani. *Origin and evolution of the Universe*. 2020. DOI: [10.48550/ARXIV.2006.12126](https://arxiv.org/abs/2006.12126). URL: <https://arxiv.org/abs/2006.12126>.
- [93] Elisabeth Krause, Tim Eifler, and Jonathan Blazek. “The impact of intrinsic alignment on current and future cosmic shear surveys”. In: *Monthly Notices of the Royal Astronomical Society* 456.1 (Dec. 2015), pp. 207–222. DOI: [10.1093/mnras/stv2615](https://doi.org/10.1093/mnras/stv2615). URL: <https://doi.org/10.1093%2Fmnras%2Fstv2615>.
- [94] Mihir Kulkarni et al. “If Dark Matter is Fuzzy, the First Stars Form in Massive Pancakes”. In: *The Astrophysical Journal Letters* 941.1 (Dec. 2022), p. L18. DOI: [10.3847/2041-8213/aca47c](https://doi.org/10.3847/2041-8213/aca47c). URL: <https://doi.org/10.3847%2F2041-8213%2Faca47c>.
- [95] Ho Lee and Alan D. Rendall. *The Einstein-Boltzmann system and positivity*. 2012. DOI: [10.48550/ARXIV.1203.2471](https://arxiv.org/abs/1203.2471). URL: <https://arxiv.org/abs/1203.2471>.
- [96] José P. S. Lemos and Oleg B. Zaslavskii. “Membrane paradigm and entropy of black holes in the Euclidean action approach”. In: *Physical Review D* 84.6 (Sept. 2011). DOI: [10.1103/physrevd.84.064017](https://doi.org/10.1103/physrevd.84.064017). URL: <https://doi.org/10.1103%2Fphysrevd.84.064017>.
- [97] Xinyu Li, Lam Hui, and Greg L. Bryan. “Numerical and perturbative computations of the fuzzy dark matter model”. In: *Physical Review D* 99.6 (Mar. 2019). DOI: [10.1103/physrevd.99.063509](https://doi.org/10.1103/physrevd.99.063509). URL: <https://doi.org/10.1103%2Fphysrevd.99.063509>.
- [98] Andrew R. Liddle and David H. Lyth. “COBE, gravitational waves, inflation and extended inflation”. In: *Physics Letters B* 291.4 (Oct. 1992), pp. 391–398. DOI: [10.1016/0370-2693\(92\)91393-n](https://doi.org/10.1016/0370-2693(92)91393-n). URL: <https://doi.org/10.1016%2F0370-2693%2892%2991393-n>.
- [99] D. Nelson Limber. “The Analysis of Counts of the Extragalactic Nebulae in Terms of a Fluctuating Density Field.” In: 117 (Jan. 1953), p. 134. DOI: [10.1086/145672](https://doi.org/10.1086/145672).
- [100] Mariangela Lisanti. “Lectures on Dark Matter Physics”. In: *New Frontiers in Fields and Strings*. WORLD SCIENTIFIC, Nov. 2016. DOI: [10.1142/9789813149441_0007](https://doi.org/10.1142/9789813149441_0007). URL: https://doi.org/10.1142%2F9789813149441_0007.

- [101] Wen-Fei Liu et al. “Energy conditions and entropy density of the universe”. In: *Results in Physics* 21 (Feb. 2021), p. 103838. DOI: [10.1016/j.rinp.2021.103838](https://doi.org/10.1016/j.rinp.2021.103838). URL: <https://doi.org/10.1016%2Fj.rinp.2021.103838>.
- [102] E. Madelung. “Quantentheorie in hydrodynamischer Form”. In: *Zeitschrift fur Physik* 40.3-4 (Mar. 1927), pp. 322–326. DOI: [10.1007/BF01400372](https://doi.org/10.1007/BF01400372).
- [103] Elisa Maggio et al. “How does a dark compact object ringdown?” In: (June 2020).
- [104] David J.E. Marsh. “Axion cosmology”. In: *Physics Reports* 643 (July 2016), pp. 1–79. DOI: [10.1016/j.physrep.2016.06.005](https://doi.org/10.1016/j.physrep.2016.06.005). URL: <https://doi.org/10.1016%2Fj.physrep.2016.06.005>.
- [105] Richard Massey, Thomas Kitching, and Johan Richard. “The dark matter of gravitational lensing”. In: *Reports on Progress in Physics* 73.8 (July 2010), p. 086901. DOI: [10.1088/0034-4885/73/8/086901](https://doi.org/10.1088/0034-4885/73/8/086901). URL: <https://doi.org/10.1088%2F0034-4885%2F73%2F8%2F086901>.
- [106] Ian D. McGreer and Greg L. Bryan. “The Impact of HD Cooling on the Formation of the First Stars”. In: *The Astrophysical Journal* 685.1 (Sept. 2008), p. 8. DOI: [10.1086/590530](https://doi.org/10.1086/590530). URL: <https://dx.doi.org/10.1086/590530>.
- [107] Nathan Mendes et al. *Numerical Methods for Diffusion Phenomena in Building Physics: A Practical Introduction*. May 2017. ISBN: 9788568324882.
- [108] C. W. Misner, K. S. Thorne, and J. A. Wheeler. *Gravitation*. Ed. by Misner, C. W., Thorne, K. S., & Wheeler, J. A. 1973.
- [109] Philip Mocz et al. “First Star-Forming Structures in Fuzzy Cosmic Filaments”. In: *Phys. Rev. Lett.* 123 (14 Oct. 2019), p. 141301. DOI: [10.1103/PhysRevLett.123.141301](https://doi.org/10.1103/PhysRevLett.123.141301), URL: <https://link.aps.org/doi/10.1103/PhysRevLett.123.141301>.
- [110] E.O. Nadler et al. “Constraints on Dark Matter Properties from Observations of Milky Way Satellite Galaxies”. In: *Physical Review Letters* 126.9 (Mar. 2021). DOI: [10.1103/physrevlett.126.091101](https://doi.org/10.1103/physrevlett.126.091101). URL: <https://doi.org/10.1103%2Fphysrevlett.126.091101>.
- [111] Debottam Nandi. *Hamiltonian formalism of cosmological perturbations and higher derivative theories*. 2017. DOI: [10.48550/ARXIV.1707.02976](https://arxiv.org/abs/1707.02976), URL: <https://arxiv.org/abs/1707.02976>.
- [112] Rachel Kuzio de Naray, Stacy S. McGaugh, and W. J. G. de Blok. “Mass Models for Low Surface Brightness Galaxies with High-Resolution Optical Velocity Fields”. In: *The Astrophysical Journal* 676.2 (Apr. 2008), pp. 920–943. DOI: [10.1086/527543](https://doi.org/10.1086/527543). URL: <https://doi.org/10.1086%2F527543>.
- [113] Julio F. Navarro, Carlos S. Frenk, and Simon D. M. White. “A Universal Density Profile from Hierarchical Clustering”. In: 490.2 (Dec. 1997), pp. 493–508. DOI: [10.1086/304888](https://doi.org/10.1086/304888), arXiv: [astro-ph/9611107 \[astro-ph\]](https://arxiv.org/abs/astro-ph/9611107).
- [114] Julio F. Navarro, Carlos S. Frenk, and Simon D. M. White. “The Structure of Cold Dark Matter Halos”. In: 462 (May 1996), p. 563. DOI: [10.1086/177173](https://doi.org/10.1086/177173), arXiv: [astro-ph/9508025 \[astro-ph\]](https://arxiv.org/abs/astro-ph/9508025).
- [115] Jens C. Niemeyer. “Small-scale structure of fuzzy and axion-like dark matter”. In: *Progress in Particle and Nuclear Physics* 113 (July 2020), p. 103787. DOI: [10.1016/j.ppnp.2020.103787](https://doi.org/10.1016/j.ppnp.2020.103787), URL: <https://doi.org/10.1016%2Fj.ppnp.2020.103787>.
- [116] Rafael C Nunes and Sunny Vagnozzi. “Arbitrating the iS/i8 discrepancy with growth rate measurements from redshift-space distortions”. In: *Monthly Notices of the Royal Astronomical Society* 505.4 (June 2021), pp. 5427–5437. DOI: [10.1093/mnras/stab1613](https://doi.org/10.1093/mnras/stab1613). URL: <https://doi.org/10.1093%2Fmnras%2Fstab1613>.
- [117] Giovanni Cabass Oliver Philcox Mikhail Ivanov. URL: https://github.com/oliverphilcox/full_shape_likelihoods.
- [118] PITAEVSKII L. P. “Vortex lines in an imperfect Bose gas”. In: *Sov. Phys.-JETP* 13.2 (1961), p. 451. URL: <http://www.jetp.ras.ru/cgi-bin/e/index/e/13/2/p451?a=list>.

- [119] and P. A. R. Ade et al. “iPlanck/i2015 results”. In: *Astronomy & Astrophysics* 594 (Sept. 2016), A13. DOI: [10.1051/0004-6361/201525830](https://doi.org/10.1051/0004-6361/201525830). URL: <https://doi.org/10.1051%2F0004-6361%2F201525830>.
- [120] Fabio Pacucci. “The First Black Holes in the Cosmic Dark Ages”. PhD thesis. Scuola Normale Superiore, Pisa, Italy, Aug. 2016.
- [121] David Parkinson et al. “The WiggleZ Dark Energy Survey: Final data release and cosmological results”. In: *Physical Review D* 86.10 (Nov. 2012). DOI: [10.1103/physrevd.86.103518](https://doi.org/10.1103/physrevd.86.103518). URL: <https://doi.org/10.1103%2Fphysrevd.86.103518>
- [122] J. A. Peacock and S. J. Dodds. “Reconstructing the linear power spectrum of cosmological mass fluctuations”. In: *Monthly Notices of the Royal Astronomical Society* 267.4 (Apr. 1994), pp. 1020–1034. DOI: [10.1093/mnras/267.4.1020](https://doi.org/10.1093/mnras/267.4.1020). URL: <https://doi.org/10.1093%2Fmnras%2F267.4.1020>.
- [123] J. A. Peacock and R. E. Smith. “Halo occupation numbers and galaxy bias”. In: 318.4 (Nov. 2000), pp. 1144–1156. DOI: [10.1046/j.1365-8711.2000.03779.x](https://doi.org/10.1046/j.1365-8711.2000.03779.x). arXiv: [astro-ph/0005010 \[astro-ph\]](https://arxiv.org/abs/astro-ph/0005010).
- [124] R. D. Peccei and Helen R. Quinn. “Constraints imposed by CP conservation in the presence of pseudoparticles”. In: *Phys. Rev. D* 16 (6 Sept. 1977), pp. 1791–1797. DOI: [10.1103/PhysRevD.16.1791](https://doi.org/10.1103/PhysRevD.16.1791). URL: <https://link.aps.org/doi/10.1103/PhysRevD.16.1791>.
- [125] R. D. Peccei and Helen R. Quinn. “CP Conservation in the Presence of Pseudoparticles”. In: *Phys. Rev. Lett.* 38 (25 June 1977), pp. 1440–1443. DOI: [10.1103/PhysRevLett.38.1440](https://doi.org/10.1103/PhysRevLett.38.1440). URL: <https://link.aps.org/doi/10.1103/PhysRevLett.38.1440>.
- [126] Roberto D. Peccei. “The Strong CP Problem and Axions”. In: *Lecture Notes in Physics*. Springer Berlin Heidelberg, 2008, pp. 3–17. DOI: [10.1007/978-3-540-73518-2_1](https://doi.org/10.1007/978-3-540-73518-2_1). URL: https://doi.org/10.1007%2F978-3-540-73518-2_1.
- [127] P. J. E. Peebles. *Principles of Physical Cosmology*. 1993. DOI: [10.1515/9780691206721](https://doi.org/10.1515/9780691206721).
- [128] P. J. E. Peebles. *The large-scale structure of the universe*. 1980.
- [129] R. Penrose and R. M. Floyd. “Extraction of Rotational Energy from a Black Hole”. In: *Nature Physical Science* 229.6 (Feb. 1971), pp. 177–179. DOI: [10.1038/physci229177a0](https://doi.org/10.1038/physci229177a0).
- [130] A. A. Penzias and R. W. Wilson. “A Measurement of Excess Antenna Temperature at 4080 Mc/s.” In: 142 (July 1965), pp. 419–421. DOI: [10.1086/148307](https://doi.org/10.1086/148307).
- [131] P. C. Peters and J. Mathews. “Gravitational Radiation from Point Masses in a Keplerian Orbit”. In: *Phys. Rev.* 131 (1 July 1963), pp. 435–440. DOI: [10.1103/PhysRev.131.435](https://doi.org/10.1103/PhysRev.131.435). URL: <https://link.aps.org/doi/10.1103/PhysRev.131.435>.
- [132] Oliver H. E. Philcox and Mikhail M. Ivanov. “BOSS DR12 full-shape cosmology: Λ CDM constraints from the large-scale galaxy power spectrum and bispectrum monopole”. In: *Physical Review D* 105.4 (Feb. 2022). DOI: [10.1103/physrevd.105.043517](https://doi.org/10.1103/physrevd.105.043517). URL: <https://doi.org/10.1103%2Fphysrevd.105.043517>.
- [133] Lorenzo Pizzuti et al. “Future constraints on the gravitational slip with the mass profiles of galaxy clusters”. In: *Monthly Notices of the Royal Astronomical Society* 486.1 (Mar. 2019), pp. 596–607. DOI: [10.1093/mnras/stz825](https://doi.org/10.1093/mnras/stz825). URL: <https://doi.org/10.1093%2Fmnras%2Fstz825>.
- [134] Planck Collaboration et al. “Planck 2018 results - I. Overview and the cosmological legacy of Planck”. In: *A&A* 641 (2020), A1. DOI: [10.1051/0004-6361/201833880](https://doi.org/10.1051/0004-6361/201833880). URL: <https://doi.org/10.1051/0004-6361/201833880>.
- [135] Planck Collaboration et al. “Planck 2018 results. VI. Cosmological parameters”. In: 641, A6 (Sept. 2020), A6. DOI: [10.1051/0004-6361/201833910](https://doi.org/10.1051/0004-6361/201833910). arXiv: [1807.06209 \[astro-ph.CO\]](https://arxiv.org/abs/1807.06209).
- [136] William H. Press and Saul A. Teukolsky. “Floating Orbits, Superradiant Scattering and the Black-hole Bomb”. In: *Nature* 238 (1972), pp. 211–212. DOI: [10.1038/238211a0](https://doi.org/10.1038/238211a0).
- [137] Joel R. Primack and Michael A. K. Gross. *Hot Dark Matter in Cosmology*. 2000. DOI: [10.48550/ARXIV.ASTRO-PH/0007165](https://arxiv.org/abs/10.48550/ARXIV.ASTRO-PH/0007165). URL: <https://arxiv.org/abs/astro-ph/0007165>.

- [138] Stuart Raby. *Grand Unified Theories*. 2006. DOI: [10.48550/ARXIV.HEP-PH/0608183](https://doi.org/10.48550/ARXIV.HEP-PH/0608183). URL: <https://arxiv.org/abs/hep-ph/0608183>.
- [139] Tullio Regge and John A. Wheeler. “Stability of a Schwarzschild Singularity”. In: *Phys. Rev.* 108 (4 Nov. 1957), pp. 1063–1069. DOI: [10.1103/PhysRev.108.1063](https://doi.org/10.1103/PhysRev.108.1063). URL: <https://link.aps.org/doi/10.1103/PhysRev.108.1063>.
- [140] Antonio Riotto. *Theories of Baryogenesis*. 1998. DOI: [10.48550/ARXIV.HEP-PH/9807454](https://doi.org/10.48550/ARXIV.HEP-PH/9807454). URL: <https://arxiv.org/abs/hep-ph/9807454>.
- [141] Keir K. Rogers and Hiranya V. Peiris. “Strong Bound on Canonical Ultralight Axion Dark Matter from the Lyman-Alpha Forest”. In: *Physical Review Letters* 126.7 (Feb. 2021). DOI: [10.1103/physrevlett.126.071302](https://doi.org/10.1103/physrevlett.126.071302). URL: <https://doi.org/10.1103/physrevlett.126.071302>.
- [142] Keir K. Rogers et al. *Ultra-light axions and the S_8 tension: joint constraints from the cosmic microwave background and galaxy clustering*. 2023. DOI: [10.48550/ARXIV.2301.08361](https://doi.org/10.48550/ARXIV.2301.08361). URL: <https://arxiv.org/abs/2301.08361>.
- [143] Ashley J. Ross et al. “The clustering of the SDSS DR7 main Galaxy sample – I. A 4 per cent distance measure at $z = 0.15$ ”. In: *Monthly Notices of the Royal Astronomical Society* 449.1 (Mar. 2015), pp. 835–847. DOI: [10.1093/mnras/stv154](https://doi.org/10.1093/mnras/stv154). URL: <https://doi.org/10.1093/mnras/stv154>.
- [144] Ippocratis D. Saltas et al. “Anisotropic Stress as a Signature of Nonstandard Propagation of Gravitational Waves”. In: *Physical Review Letters* 113.19 (Nov. 2014). DOI: [10.1103/physrevlett.113.191101](https://doi.org/10.1103/physrevlett.113.191101). URL: <https://doi.org/10.1103/physrevlett.113.191101>.
- [145] D. Schaefer. “On the properties of massive Population III stars and metal-free stellar populations”. In: *Astronomy & Astrophysics* 382.1 (Jan. 2002), pp. 28–42. DOI: [10.1051/0004-6361:20011619](https://doi.org/10.1051/0004-6361:20011619). URL: <https://doi.org/10.1051/0004-6361:20011619>.
- [146] Hsi-Yu Schive, Tzihong Chiueh, and Tom Broadhurst. “Cosmic structure as the quantum interference of a coherent dark wave”. In: *Nature Physics* 10.7 (June 2014), pp. 496–499. DOI: [10.1038/nphys2996](https://doi.org/10.1038/nphys2996). URL: <https://doi.org/10.1038/nphys2996>.
- [147] Jeremy D. Schnittman. “The collisional Penrose process”. In: *General Relativity and Gravitation* 50.6 (June 2018). DOI: [10.1007/s10714-018-2373-5](https://doi.org/10.1007/s10714-018-2373-5). URL: <https://doi.org/10.1007/s10714-018-2373-5>.
- [148] Carolin Seitz and Peter Schneider. *Steps towards nonlinear cluster inversion through gravitational distortions: III. Including a redshift distribution of the sources*. 1996. arXiv: [astro-ph/9601079 \[astro-ph\]](https://arxiv.org/abs/astro-ph/9601079).
- [149] P. Simon. “How accurate is Limber’s equation?” In: *Astronomy & Astrophysics* 473.3 (Aug. 2007), pp. 711–714. DOI: [10.1051/0004-6361:20066352](https://doi.org/10.1051/0004-6361:20066352). URL: <https://doi.org/10.1051/0004-6361:20066352>.
- [150] R. E. Smith et al. “Stable clustering, the halo model and non-linear cosmological power spectra”. In: *Monthly Notices of the Royal Astronomical Society* 341.4 (June 2003), pp. 1311–1332. DOI: [10.1046/j.1365-8711.2003.06503.x](https://doi.org/10.1046/j.1365-8711.2003.06503.x). URL: <https://doi.org/10.1046/j.1365-8711.2003.06503.x>.
- [151] J. A. Sobrin et al. “The Design and Integrated Performance of SPT-3G”. In: *The Astrophysical Journal Supplement Series* 258.2 (Feb. 2022), p. 42. DOI: [10.3847/1538-4365/ac374f](https://doi.org/10.3847/1538-4365/ac374f). URL: <https://doi.org/10.3847/1538-4365/ac374f>.
- [152] David N. Spergel and Paul J. Steinhardt. “Observational Evidence for Self-Interacting Cold Dark Matter”. In: *Physical Review Letters* 84.17 (Apr. 2000), pp. 3760–3763. DOI: [10.1103/physrevlett.84.3760](https://doi.org/10.1103/physrevlett.84.3760). URL: <https://doi.org/10.1103/physrevlett.84.3760>.
- [153] Matthew J. Stott and David J. E. Marsh. “Black hole spin constraints on the mass spectrum and number of axionlike fields”. In: *Physical Review D* 98.8 (Oct. 2018). DOI: [10.1103/physrevd.98.083006](https://doi.org/10.1103/physrevd.98.083006). URL: <https://doi.org/10.1103/physrevd.98.083006>.

- [154] Zdeněk Stuchlík, Martin Kološ, and Arman Tursunov. “Penrose Process: Its Variants and Astrophysical Applications”. In: *Universe* 7.11 (2021). ISSN: 2218-1997. DOI: [10.3390/universe7110416](https://doi.org/10.3390/universe7110416). URL: <https://www.mdpi.com/2218-1997/7/11/416>.
- [155] Masahiro Takada and Bhuvnesh Jain. “The three-point correlation function in cosmology”. In: *Monthly Notices of the Royal Astronomical Society* 340.2 (Apr. 2003), pp. 580–608. ISSN: 0035-8711. DOI: [10.1046/j.1365-8711.2003.06321.x](https://doi.org/10.1046/j.1365-8711.2003.06321.x). eprint: <https://academic.oup.com/mnras/article-pdf/340/2/580/18646799/340-2-580.pdf>. URL: <https://doi.org/10.1046/j.1365-8711.2003.06321.x>.
- [156] NASA / WMAP Science Team. URL: https://wmap.gsfc.nasa.gov/universe/universe_shape.html.
- [157] NASA/WMAP Science Team. *Wilkinson Microwave Anisotropy Probe*. <https://map.gsfc.nasa.gov/>. [Page Updated: Friday, 12-22-2017]. 2012.
- [158] Saul A Teukolsky. “The Kerr metric”. In: *Classical and Quantum Gravity* 32.12 (June 2015), p. 124006. DOI: [10.1088/0264-9381/32/12/124006](https://doi.org/10.1088/0264-9381/32/12/124006). URL: <https://doi.org/10.1088/0264-9381%2F32%2F12%2F124006>.
- [159] Eemeli Tomberg. *Unit conversions and collected numbers in cosmology*. 2022. arXiv: [2110.12251 \[astro-ph.CO\]](https://arxiv.org/abs/2110.12251).
- [160] Jesús Torrado and Antony Lewis. *Cobaya: Bayesian analysis in cosmology*. Astrophysics Source Code Library, record ascl:1910.019. Oct. 2019. ascl: [1910.019](https://ascl.net/1910.019).
- [161] Jesús Torrado and Antony Lewis. “Cobaya: code for Bayesian analysis of hierarchical physical models”. In: *Journal of Cosmology and Astroparticle Physics* 2021.05 (May 2021), p. 057. DOI: [10.1088/1475-7516/2021/05/057](https://doi.org/10.1088/1475-7516/2021/05/057). URL: <https://doi.org/10.1088/1475-7516%2F2021%2F05%2F057>.
- [162] Sean Tulin and Hai-Bo Yu. “Dark matter self-interactions and small scale structure”. In: *Physics Reports* 730 (Feb. 2018), pp. 1–57. DOI: [10.1016/j.physrep.2017.11.004](https://doi.org/10.1016/j.physrep.2017.11.004). URL: <https://doi.org/10.1016%2Fj.physrep.2017.11.004>.
- [163] Michael S. Turner. “The hot big bang and beyond”. In: *AIP Conference Proceedings*. AIP, 1995. DOI: [10.1063/1.48810](https://doi.org/10.1063/1.48810). URL: <https://doi.org/10.1063%2F1.48810>.
- [164] Rodrigo Vicente, Vitor Cardoso, and Jorge C. Lopes. “Penrose process, superradiance, and ergoregion instabilities”. In: *Physical Review D* 97.8 (Apr. 2018). DOI: [10.1103/physrevd.97.084032](https://doi.org/10.1103/physrevd.97.084032). URL: <https://doi.org/10.1103%2Fphysrevd.97.084032>.
- [165] A. Vilenkin. “Exponential Amplification of Waves in the Gravitational Field of Ultrarelativistic Rotating Body”. In: *Phys. Lett. B* 78 (1978), pp. 301–303. DOI: [10.1016/0370-2693\(78\)90027-8](https://doi.org/10.1016/0370-2693(78)90027-8).
- [166] Robert M. Wald. “Energy Limits on the Penrose Process”. In: 191 (July 1974), pp. 231–234. DOI: [10.1086/152959](https://doi.org/10.1086/152959).
- [167] David H. Weinberg et al. “Cold dark matter: Controversies on small scales”. In: *Proceedings of the National Academy of Sciences* 112.40 (Feb. 2015), pp. 12249–12255. DOI: [10.1073/pnas.1308716112](https://doi.org/10.1073/pnas.1308716112). URL: <https://doi.org/10.1073%2Fpnas.1308716112>.
- [168] Lawrence M. Widrow et al. “Power spectrum for the small-scale Universe”. In: *Monthly Notices of the Royal Astronomical Society* 397.3 (July 2009), pp. 1275–1285. ISSN: 0035-8711. DOI: [10.1111/j.1365-2966.2009.15075.x](https://doi.org/10.1111/j.1365-2966.2009.15075.x). eprint: <https://academic.oup.com/mnras/article-pdf/397/3/1275/3726666/mnras0397-1275.pdf>. URL: <https://doi.org/10.1111/j.1365-2966.2009.15075.x>.
- [169] Jaswant K. Yadav. *Nature of Clustering of Large Scale Structures*. 2009. DOI: [10.48550/ARXIV.0910.0806](https://arxiv.org/abs/0910.0806). URL: <https://arxiv.org/abs/0910.0806>.
- [170] Amr El-Zant, Isaac Shlosman, and Yehuda Hoffman. “Dark Halos: The Flattening of the Density Cusp by Dynamical Friction”. In: *The Astrophysical Journal* 560.2 (Oct. 2001), pp. 636–643. DOI: [10.1086/322516](https://doi.org/10.1086/322516). URL: <https://doi.org/10.1086%2F322516>.
- [171] Jesús Zavala and Carlos S. Frenk. *Dark matter haloes and subhaloes*. 2019. DOI: [10.48550/ARXIV.1907.11775](https://arxiv.org/abs/1907.11775). URL: <https://arxiv.org/abs/1907.11775>.

- [172] Ya. B. Zel'Dovich. "Generation of Waves by a Rotating Body". In: *Soviet Journal of Experimental and Theoretical Physics Letters* 14 (Aug. 1971), p. 180.
- [173] Jiajun Zhang, Hantao Liu, and Ming-Chung Chu. "Cosmological Simulation for Fuzzy Dark Matter Model". In: *Frontiers in Astronomy and Space Sciences* 5 (Jan. 2019). DOI: [10.3389/fspas.2018.00048](https://doi.org/10.3389/fspas.2018.00048), URL: <https://doi.org/10.3389%2Ffspas.2018.00048>.
- [174] J. Zuntz et al. "CosmoSIS: Modular cosmological parameter estimation". In: *Astronomy and Computing* 12 (Sept. 2015), pp. 45–59. DOI: [10.1016/j.ascom.2015.05.005](https://doi.org/10.1016/j.ascom.2015.05.005), URL: <https://doi.org/10.1016%2Fj.ascom.2015.05.005>.
- [175] F. Zwicky. "Die Rotverschiebung von extragalaktischen Nebeln". In: *Helvetica Physica Acta* 6 (Jan. 1933), pp. 110–127.